2015

MICRO- AND MACRO-SCALE MODELING OF FILTER AGING: EFFECTS OF PARTICLE POLY-DISPERSITY AND FIBER CROSS-SECTIONAL SHAPE

Ahmed M. Saleh
saleham@vcu.edu

MICRO- AND MACRO-SCALE MODELING OF FILTER AGING: EFFECTS OF PARTICLE POLY-DISPERSITY AND FIBER CROSS-SECTIONAL SHAPE

Ph.D. Dissertation
by

AHMED M. SALEH

ADVISOR

DR. HOOMAN V. TAFRESHI

Department of Mechanical and Nuclear Engineering
Virginia Commonwealth University
Richmond, VA, USA
August 2015

Acknowledgements

I would of course like to thank my advisor, Dr. Hooman Vahedi Tafreshi, for all his guidance, patience, teaching and wisdom. Without him, this thesis would not have been as it is.

I would also like to thank my Ph.D. committee members—Dr. Daren Chen, Dr. Worth Longest, Dr. Rebecca Segal, and Dr. Puru Jena—for their participation and fruitful comments that strengthen my research.

Finally, I would indeed like to thank my wife for her patience and support along through these years of my Ph.D. studies. I will always be grateful to her, my mom, my dad, my sisters, my brother, my lab mates and all my friends.

Table of Contents

Abstract

MICRO- AND MACRO-SCALE MODELING OF FILTER AGING: EFFECTS OF PARTICLE POLY-DISPERSITY AND FIBER CROSS-SECTIONAL SHAPE

By: Ahmed Mohammed Saleh
A dissertation submitted in partial fulfillment of the requirements for the degree of Doctor of Philosophy at Virginia Commonwealth University.

Virginia Commonwealth University, 2015

Director: Dr. Hooman Vahedi Tafreshi
Professor, Mechanical and Nuclear Engineering

The goal of this study is to further advance the state of the art in developing self-sufficient methods to predict the performance of an aerosol filter. The simulation methods developed in this study are based on first principles and consequently, they do not rely on empirical correction factors. These simulation methods can be used to predict the instantaneous collection efficiency and pressure drop of a filter under dust-loading conditions. In the current study, 3-D micro- and macroscale CFD models are developed to simulate the service life of flat-sheet and pleated filters. These CFD micro- and macroscale models are also used to quantify the effects of a fiber's cross-sectional shape on the performance of the resulting filter. As fiber manufacturing methods are rapidly advancing, these fibers are becoming more accessible. The filtration performance of trilobal fibers is compared with their circular counterparts under dust-loading conditions. Our results show that trilobal fibers do not outperform circular ones except in very limited conditions, revealing no advantage over circular fibers.

In addition, a fast but approximate 2-D model is developed to predict the filtration performance of flat and circular pleated filters. The predictions of the model are compared with predictions from the more sophisticated CFD models, as well as with experimental work in the literature. Our 2-D model developed in this study is aimed at providing the aerosol filtration industry with a fast but fairly accurate method of designing pleated filters. With a CPU-time of practically zero, the developed model allows one to conduct a broad parameter study, altering the parameters that affect the filtration performance of pleated filters. Using this model, predictive correlations for dust-loaded pleated filters are presented. These correlations allow one to estimate the instantaneous pressure drop and collection efficiency of pleated filters effectively.

Chapter 1

General Introduction

1. Background

Fibrous materials are the most commonly used means of particle filtration. The theory of particle filtration was originally developed for a single fiber (the single fiber theory which dates back to the work of Kuwabara in 1959) and later extended to also include the effects of neighboring fibers (see the books of Brown, 1993; Spurny, 1998; and Tien, 2012 for comprehensive reviews of the filtration literature). These theories have originally been developed using an exact or a numerical solution of the flow field around perfectly clean fibers placed normal to the flow direction in a 2-D ordered configuration (i.e., lattice). Obviously, deposition of filtered particles leads to the formation of complicated dendrites on the surface of the fibers, altering the flow field inside a filter, and thereby affecting its pressure drop and collection efficiency beyond the predictions provided by the above theories.

The pressure drop across clean fibrous media can be predicted by the empirical well-known equation of Davies (1973):

$$\frac{\Delta p_0}{Z} = 64\mu V \frac{\alpha^{1.5}(1+65\alpha^3)}{d_f^2} \tag{1.1}$$

Where α is the Solid Volume Fraction (SVF), d_f is the fiber diameter, Z is the filter thickness and V is the air velocity. The collection efficiency of any fibrous structure is defined as the fraction of captured particles to the total inlet particles to the fibrous medium:

$$E = \frac{N_{inlet} - N_{outlet}}{N_{inlet}} \tag{1.2}$$

In addition to the efficiency, penetration is commonly used in filtration defined as

$$P = \frac{N_{outlet}}{N_{inlet}} \tag{1.3}$$

There are three major mechanisms that cause particles to deposit on the surface of a fiber in a filter. A brief discussion for each of these mechanisms is given below.

I. Brownian Diffusion

Brownian motion is the irregular wiggling motion of a particle caused by the random collision of the gas molecules with the surface of the particle. Thermal diffusion is the primary deposition mechanism for particles less than 0.1 µm in diameter (Hinds, 1982). This random motion of the small particles enhances the probability of colliding with the fiber's surface and hence, the deposition probability as can be seen in Fig. 1.1.

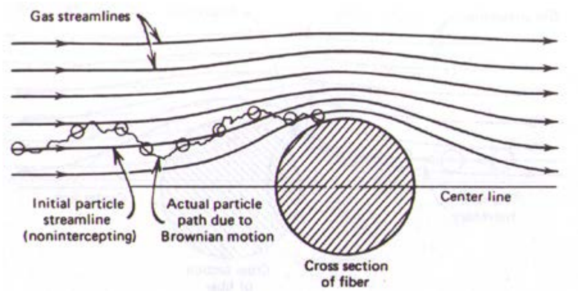

Figure 1.1: Single fiber collection by diffusion.[1]

---

[1] W.C. Hinds, Aerosol Technology, properties, behavior, and measurement of airborne particles. John Wiley & Sons, Inc. New York, 1982

II. Direct Interception

Interception deposition takes place when a particle perfectly follows the streamlines of the gas and touches the fiber's surface because of its finite volume (i.e. when the streamline is closer to the surface of the fiber with a distance of a particle radius or less) as shown in Fig. 1.2.

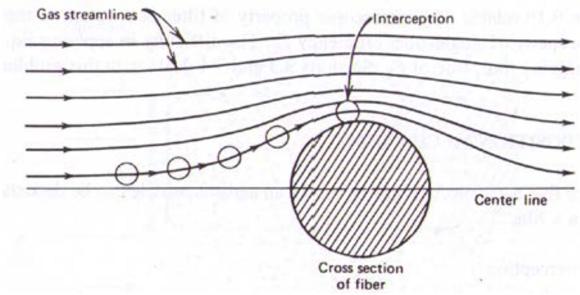

Figure 1.2: Single fiber collection by interception.[2]

III. Inertial Impaction

Inertial impaction takes place when the particle deviates from following the streamline because of its inertia. Inertial particles need more time to adjust to the change in the direction, which cause the particle to hit the fiber as they fail to exactly adapt their motion to match the curved streamlines of the flow close to the fiber as shown in the Fig. 1.3.

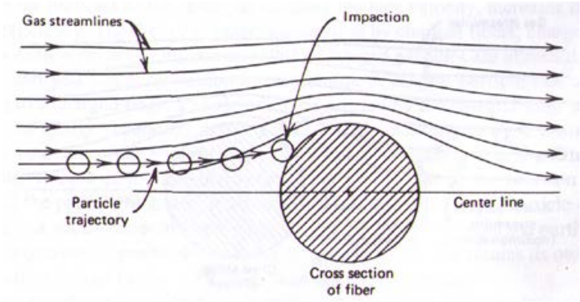

Figure 1.3: Single fiber collection by impaction.[3]

---

[2] W.C. Hinds, Aerosol Technology, properties, behavior, and measurement of airborne particles. John Wiley & Sons, Inc. New York, 1982

[3] W.C. Hinds, Aerosol Technology, properties, behavior, and measurement of airborne particles. John Wiley & Sons, Inc. New York, 1982

The total Single Fiber Efficiency (SFE) is defined as the ratio of the number of particles collected by the fiber to the number of particles that passed through an imaginary projected area of the fiber. The SFE by interception, diffusion, and impaction can be obtained from different correlations; however, for the sake of brevity we chose some of the well-known expressions and stated them below.

For the interception SFE, the expression proposed by Lee and Liu (1982) is commonly used:

$$\eta_R = 0.6\frac{1-\alpha}{Ku}\frac{R^2}{1+R} \tag{1.4}$$

In this equation $Ku = -\frac{ln\,\alpha}{2} - 0.75 + \alpha - 0.25\alpha^2$ is the Kuwabara factor, R is the particle to fiber diameter ratio. The SFE due to impaction is obtained using the following expression given by Brown (1993) for moderate values of Stokes number:

$$\eta_I = \frac{\mathrm{St}^3}{\mathrm{St}^3 + 0.77\mathrm{St}^2 + 0.22} \tag{1.5}$$

where $Stk = \frac{\rho_P\, d_P^2\, c^c\, V}{18\,\mu\, d_f}$ is the Stokes number.

SFE due to Brownian Diffusion can be obtained from the expression proposed by Lee and Liu, (1982) as in the following equation:

$$\eta_D = 2.6\left(\frac{1-\alpha}{Ku}\right)^{1/3} Pe^{-2/3} \tag{1.6}$$

Where Ku is the Kuwabara factor as mentioned above, $Pe = V\, d_f \,/\, D$ is the Peclet number, $D = \sigma\, c^c\, T \,/\, (3\pi\,\mu\, d_P)$ is particle diffusivity, and $\sigma = 1.38\times10^{-23}\,(m^2 kg\, s^{-2}\, K^{-1})$ is Boltzmann constant.

Filtration efficiency, *E,* can be obtained based on the total SFE, $\eta_{\Sigma 0}$, as follows using (Brown 1993):

$$\eta_{\Sigma 0} = 1-\left(1-\eta_R\right)\left(1-\eta_I\right)\left(1-\eta_D\right) \tag{1.7}$$

$$E = 1-exp\left(\frac{-4\alpha\,\eta_{\Sigma 0}\,Z}{\pi d_f\,(1-\alpha)}\right) \tag{1.8}$$

1.1. Aerosol Filtration via Fibrous Filters

The first numerical study to simulate the effects of particle deposition on pressure drop and collection efficiency of a filter is that of Payatakes and Tien (1976), who simulated the growth of chain-like dendrites on a fiber in a Kuwabara cell. For simplicity, they considered interception to be the only particle collection mechanism. Later, Payatakes and Gradon (1980) modified this model to also include particle capture via diffusion and inertial impaction mechanisms. Utilizing a Monte Carlo technique in a Kuwabara cell, Kanaoka et al. (1980) calculated the SFE for particles in the inertial and interception regimes. More recently, Kanaoka et al. (2001) and Cheung et al. (2005) reported on case studies in which particle deposition on orderly packed electret fibers was numerically simulated. Nevertheless, in neither of the above studies was the air flow field recalculated during the particle deposition process, leading to an overestimation of the fibers' collection efficiency. Since then, there have been few other studies that reported simulation of particle dendrite growth on a single fiber (e.g., Filippova and Hanel, 1997; Przekop et al., 2003; Lantermann et al., 2007; Li and Marshall, 2007; Wang et al., 2012; Hosseini and Tafreshi, 2012).

In spite of its relevance, predicting the capture efficiency and pressure drop of a particle-loaded fibrous filter via any form of a 2-D simulation is a simplification. This is because of the inherent differences between the random three-dimensional structure of a real fibrous filter and a two-dimensional ordered structure. Moreover, particle dendrites are 3-D objects by their own nature, and any 2-D simulation of their growth is a misrepresentation of the physics of the problem. In addition, it is hard to relate the outcomes of a study conducted for a single fiber under dust-loading conditions to the performance of a real particle-loaded filter, as in a real fibrous filter the fibers located on the side of the filter facing the incoming particles receive more deposition than those deep inside the structure. Therefore, because of the fundamental differences between both the geometry and the particle deposition pattern in a real fibrous filter and those in its 2-D counterpart, the results of cell model calculations always require empirical correction factors (not available prior to manufacturing and testing a new filter) before they can be used to provide reliable performance predictions.

Our research group have previously demonstrated and reported the advantages of generating virtual 3-D models that can mimic the internal microstructure of a fibrous structure for predicting simulating pressure drop and collection efficiency of clean filters (Hosseini and Tafreshi, 2010a). Such 3-D models do not need empirical correction factors, as they are developed based on first principles, and their predictions can directly be used for product design and development. The problem with 3-D microscale models, however, is that they are computationally expensive. This may limit one’s ability to conduct an extensive parameter study, especially in the presence of particle loading. Fortunately, with the current rate of progress in the development of advanced computers, it is expected that 3-D microscale simulations will become more viable. However, the above studies investigate the performance of clean filters not loaded. It is also important to mention that the humidity affect the filtration performance in addition to the adhesion efficiency (the probability of a particle to stick on the filter surface and not to rebound, see Gupta et al., 1993; Joubert et al., 2010, 2011; Montgomery et al., 2015 for more information). However, studying the effect of the humidity and particle rebound was beyond the objective of this research.

1.2 Pleated Aerosol Filters

Pleated filters have vast areas of applications in the automotive industry, HVAC systems, and clean rooms among many others, especially when high aerosol filtration performance or compact filter design is required. Controlling the air flow inside pleats is an essential consideration which allows for minimizing pressure drop and maximizing particle collection efficiency. The air flow pattern in pleated filters usually depends on two major contributors. The first is the fibrous medium or the flat-sheet paper which will be folded to make pleats. The second is the pleat geometry (i.e. pleat width, pleat height and pleat shape) which can influence the performance of the filter via viscous effects. In addition, dust deposition can be another factor involved in filter performance. In general, most of the published research which studies pleated filters concentrates on optimizing clean pleats to minimize pressure drop (Chen et al., 1995; Lucke and Fissan, 1996; Del Fabbro et al., 2002; Caesar and Schroth, 2002; Subernat et al., 2003; Tronville and Sala, 2003; Wakeman et al., 2005; Waghode et al., 2007; Lo et al., 2010). To the knowledge of the authors, there are no criteria for designing pleat shape and pleat count which optimize both the pressure drop and collection efficiency.

The influence of particle loading (i.e., filter aging) on the performance of pleated fibrous filters has not been vastly studied in the past. To date, there are a few studies that can be found which study the effects of surface dust loading on the performance of pleated filters: the work of Rebai et al, (2010), Fotovati et al., (2011), and the experimental work of Hasolli et al., (2013). These numerical studies are limited in their findings by simplifications. For instance, the work of Rebai et al., (2010) was limited to only surface deposition and mainly monitored pleats' pressure drop. In addition, their results rely on empirical coefficients that correspond to certain specific conditions. They also did not report the shape of deposition and neglected the inertia of the particles as they assumed that the particles exactly follow the flow streamlines. In our group, Fotovati et al., (2011) reported the pressure drop of pleated filters when loading; however, particle deposition was assumed to be on the surface—simulating HEPA filters. Fotovati et al., (2012) proposed a methodology to model in-depth dust deposition and measure the collection efficiency of pleated filters. Two-dimensional dendrites do not provide realistic results as the dendrites in reality are 3-D structures, which leads 2-D simplifications to report higher values of pressure drop and higher rates of increase in collection efficiency with loading as discussed earlier. All of the aforementioned numerical studies concerning deposition in pleated filters were conducted in two dimensional domains, however, the current study provides a more realistic and comprehensive study of the performance of pleated filters. In this macroscale model, depth and surface deposition of poly-dispersed particles is simulated in 3-D domains. Fig. 1.4 demonstrates the domain of a pleated filter with its boundary conditions.

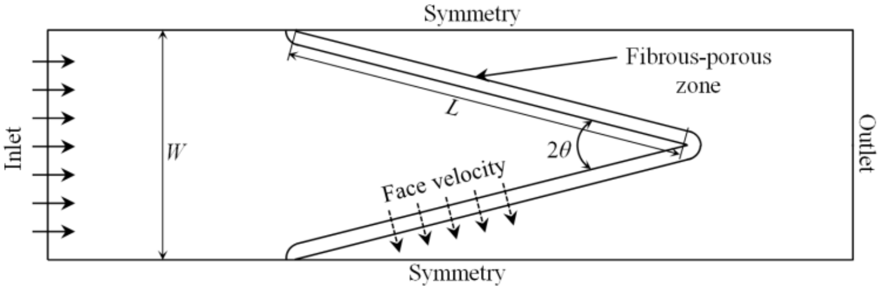

Figure 1.4: An example of pleated filter domain with its boundary conditions.

1.3 Overall Objectives of this Thesis

This thesis primarily focuses on predicting filtration performance of a fibrous filter under dust loading conditions. The main parameters describing the performance of a fibrous filter are the filtration efficiency and the pressure drop. In this study, we developed micro and macroscale models to be able to predict the performance of flat-sheet and pleated filters. We also used these models to understand the effect of fiber cross-sectional shape on the filtration performance of fibrous filters exposed to particle loading.

Chapter 2 focuses on our microscale approach which was developed to simulate the pressure drop and collection efficiency of flat-sheet fibrous media under dust loading conditions. The chapter explains how the air flow field through 3-D disordered geometries representing the internal microstructure of a fibrous filter is obtained by numerically solving Stokes' equations. For particle tracking, a Lagrangian approach is used to track the particles through our virtual filter media and determine the filter's collection efficiency under different dust-load conditions.

The calculations in this chapter were conducted using the ANSYS CFD code enhanced with a series of in-house C subroutines. We then compared the results of our simulations with those obtained from a 1-D macroscale model developed based on some of the pioneering studies reported in the literature.

In Chapter 3, we present a flexible 3-D macroscale simulation method for modeling the instantaneous pressure drop and collection efficiency of pleated fibrous filters when exposed to poly-dispersed aerosols in both the surface and depth filtration regimes. The simulations are conducted using the Fluent CFD code enhanced with a different set of in-house subroutines. A cluster-injection method is developed to accelerate the formation and growth of dust-cake both inside and outside the filter media. The model was calibrated with empirical and more accurate microscale simulations. The macroscale model can be used to simulate the service life of a pleated filter with reasonable accuracy and CPU time and can be used to design and develop pleated filters for different applications. In particular, it allows one to study the effects of pleat shape, pleat count, filter porosity, fiber diameter(s), flow velocity, aerosol concentration, and particle diameter, as well as the aerodynamic parameters of the flow on the evolution of a filter's pressure drop and collection efficiency over time. For demonstration purposes, performance of an arbitrary filter with 2 and 4 pleats per inch is simulated when challenged with poly-dispersed particles of 1 to 10 μm in diameter.

In Chapter 4, both micro and macroscale models mentioned above were utilized to shed some light on the filtration performance of fibers with trilobal cross-section in comparison to their circular counterparts when loaded with aerosol particles. Different flow velocities are considered to discuss performance of trilobal fibers under different particle capture regimes. Trilobal fibers are found to outperform their circular counterparts only when the particles are highly inertial, and only if the orientation of the trilobal cross-section with respect to the incoming flow is such that one of the grooves of the fiber faces the flow with a normal angle. In cases of low-inertia particles, trilobal fibers were found to experience higher efficiency values with loading but at the expense of higher increase in pressure drop. We also studied the effects of the through-plane orientation of the trilobal fibers on their performance relative to their circular counterpart. Similar conclusions were drawn from the latter simulations.

Chapter 5 presents a semi-numerical 2-D model for predicting the instantaneous pressure drop and collection efficiency of filters made up of rectangular and triangular pleats in both the depth and surface filtration regimes. Inspired from our previous CFD simulations, the semi-numerical model adopts appropriate average velocity profiles in the axial and lateral directions to approximate the flow field inside rectangular and triangular pleat channels using Darcy’s law and the continuity equation. The model therefore circumvents the need to obtain a CPU-intensive solution for the partial differential equation governing the flow through a filter, i.e., the Navier–Stokes equation. The above-mentioned analytical flow field can then be used to predict the trajectory of the particles flowing through pleat channel by numerically solving the equation of motion for each particle—a simple set of second order ordinary differential equations. With the particles trajectories obtained, the deposition location and hence the dust-cake profile can be approximated. This allows one to predict the instantaneous pressure drop and collection efficiency of a filter (filter’s service life) with a CPU-time of practically zero. A brief parameter study is presented to demonstrate the method.

Chapter 6 focuses on extending the above-mentioned 2-D semi-numerical model for predicting the instantaneous pressure drop and collection efficiency of radial pleated filters (cartridge filters). Based on CFD simulations, the velocity profiles inside the pleat channels were adopted in radial and tangential direction and were different than those in a flat triangular pleated filter presented in our previous work. The model for radial filters is used to predict the particle trajectories by solving the equation of motion for the particles. Obtaining these particle trajectories, the dust-cake profile can be approximated. The deposition sites of the particles were found to depend on the inlet and outlet diameter of the radial pleated filter. In this chapter, the differences between the performance of flat and radial pleated filters were reported by conducting a parameter study. In addition, a comparison between the predictions of our model and CFD data is presented for validation of the model.

Chapter 7 discusses our developed correlations which describe the instantaneous pressure drop of pleated filters under service conditions. Both depth and surface filtration were considered for both flat and radial pleated filters. We believe these correlations help the design and development of pleated filters by circumventing the need to pursue any CFD or macroscale simulation for loading pleated filters. We used our macroscale models in Chapter 4 and Chapter 5 flat and cartridge pleated filters in order to construct these correlations. Finally, the overall conclusions of this work are presented in Chapter 8.

Chapter 2

3-D Microscale Simulation of Dust-Loading in Thin Flat-Sheet Filters: A Comparison with 1-D Macroscale Simulations[4]

2.1 Introduction

In this chapter, a microscale approach is undertaken to simulate the instantaneous pressure drop and collection efficiency of fibrous media exposed to particle loading, i.e., filter aging. The air flow field through 3-D disordered geometries representing the internal microstructure of a fibrous filter is obtained by numerically solving Stokes' equations. The advantages of generating virtual 3-D models that can mimic the internal microstructure of a fibrous structure for predicting simulating pressure drop and collection efficiency of clean filters are presented elsewhere (Wang et al., 2006; Maze et al., 2007; Hosseini and Tafreshi, 2010a). Such 3-D models do not need empirical correction factors, as they are developed based on first principles, and their predictions can directly be used for product design and development. The problem with 3-D microscale models, however, is that they are computationally expensive. This may limit one's ability to conduct an extensive parameter study, especially in the presence of particle loading. Fortunately,

---

[4] Contents of this chapter appear in the following publication:
Saleh, A.M., Hosseini, S.A., Tafreshi, H.V., Pourdeyhimi, B. (2013). 3-D Microscale Simulation of Dust-Loading in Thin Flat-Sheet Filters: A Comparison with 1-D Macroscale Simulations. Chem. Eng. Sci. 99: 284-291.

with the current rate of progress in the development of advanced computers, it is expected that 3-D microscale simulations will become more viable. We believe 3-D microscale simulation will be the industry's preferred design method in the next few years. Moreover, such simulations, unlike the cell-model-type calculations, can be utilized to design filters with more than one fiber type (i.e., fibers with different diameters or even cross-sectional shapes). To better illustrate the advantage of 3-D microscale simulations in a more quantitative manner, we compare the instantaneous collection efficiency and pressure drop values obtained from our simulations with those of a CPU-friendly 1-D macroscale model that we developed based on the pioneering work of Thomas et al. (2001).

In the next section, we briefly describe our algorithm for generating disordered 3-D fibrous domains. We then discuss our governing equations and their boundary conditions followed by our particle tracking method. In Section 2.3, we present our implementation of the abovementioned 1-D macroscale model. Our results and discussion are given in Section 2.4, and they are followed by our conclusions for this chapter outlined in Section 2.5.

2.2 Microscale Modeling of Dust Deposition in 3-D Fibrous Media

2.2.1 Virtual Fibrous Structures

Our 3-D disordered fibrous structures were generated using an in-house C++ program as described elsewhere (e.g., Wang *et al.* 2006; Wang *et al.* 2007). We treated the fibers as perfect cylinders with lengths much greater than the size of the simulation box. Our fibrous structures are assumed to consist of fourteen layers (i.e., fibers have no through-plane orientations). The choice of fourteen layers was arbitrary, but in consideration of the available memory and the desired CPU time for each simulation. In each layer, we allowed the fibers to interpenetrate into each other. Allowing the fibers to penetrating into one another has no effect on the accuracy and reliability of the simulations as long as the solid volume fraction (SVF) of the final structure is calculated correctly. This is guaranteed by exporting the coordinates of each fiber to the Gambit software package, where the structure's void volume was calculated accurately and also meshed using tetrahedral elements. The thickness of each layer was taken to be 1.4 times greater than the fiber diameter to ease the mesh generation process (see Wang *et al.* 2006 for more information). Figure 2.1 shows and example of our fibrous domains and its boundary conditions.

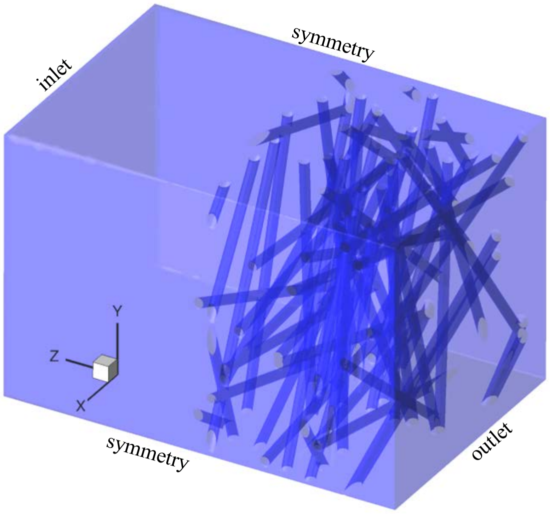

Figure 2.1: An example of our simulation domains and the boundary conditions.

2.2.2 Governing Equations

The Stokes flow regime is expected to prevail in a porous medium when the Reynolds number is smaller than unity. We used ANSYS code to solve the Stokes flow equations in void space between the fibers:

$$\nabla \cdot \vec{V} = 0 \tag{2.1}$$

$$\nabla p = \mu \nabla^2 \vec{V} \tag{2.2}$$

where $\vec{V} = u\hat{i} + v\hat{j} + w\hat{k}$ represents the flow field velocity. Air is assumed to enter the domain with a uniform velocity and leaves through a pressure-constant boundary downstream of the filter media. The lateral boundaries are considered to be symmetry (for more information regarding the boundary conditions see Wang *et al.* 2006). It is important to ensure that the x-y dimensions of the simulation domain are large enough such that the statistical uncertainty of the output results is minimized. We used the Brinkman screening length criterion for selecting appropriate x-y dimensions for our computational domains (Jaganathan *et al.* 2008).

Aerodynamic slip is expected to occur on the fiber surface when the fiber diameter is close to the mean free path of the molecules/atoms in the interstitial gas (about 65 nm for air in Normal Temperatures and Pressures). The aerodynamic slip is often characterized using the Knudsen number defined as $Kn_f = 2\lambda / d_f$ where λ is the mean free path and d_f is the fiber diameter. Previous studies on the effects of aerodynamic slip in fibrous media revealed that while aerodynamic slip can have a considerable impact on pressure drop, it does not affect the filter's collection efficiency, for the range of particle diameters of general concern in the context of aerosol filtration (see Hosseini and Tafreshi 2010b; Hosseini and Tafreshi 2011). In these studies, we developed a correction factor for the pressure drop values that one can obtain from analytical studies in which the no-slip boundary condition was considered for the fibers (e.g., that of Speilmann and Goren 1968 or Happel 1959) or the empirical correlations that have been developed using fibrous media with large fibers (e.g., empirical equation of Davies, 1973). Similarly, our correction factor can also be used to correct the pressure drop values obtained from numerical simulations conducted in the absence of aerodynamic slip. As our objective in this study was merely to provide a comparison between 3-D microscale and 1-D macroscale simulations, we used the no-slip boundary condition in both formulations.

A Lagrangian method is considered for tracking the trajectory of aerosol particles through our filter media. The standard Discrete Phase Model (DPM) of ANSYS code is enhanced with a series of in-house subroutines to customize this general purpose CFD code for the simulations conducted here. In the Lagrangian particle tracking method, the balance of forces exerted on a particle is integrated to obtain its position and velocity throughout the simulation domain.

$$\frac{d\vec{V}_p}{dt} = \frac{18\mu}{d_p^2 \rho_p C_c}\left(\vec{V} - \vec{V}_p\right) \tag{2.3}$$

where $\vec{V}_p$ is the particle velocity. Note that Brownian forces are not included in this equation, as the particles considered in the current study are not submicron. Interested readers are referred to the work of Maze *et al.* (2007) and Hosseini and Tafreshi (2010c) for modeling trajectory of nano-particles through fibrous media.

2.2.3 Implementation

As mentioned earlier, the standard DPM module in ANSYS code needs to be enhanced with in-house subroutines before it can be used for modeling aerosol filtration. ANSYS code models a particle as a point mass. Therefore, it is unable to detect a collision between a particle and a fiber (or a previously deposited particle) unless the particle’s center of mass touches the fiber. This obviously leads to a significant error in calculating particle collection efficiency via interception. This has been corrected by developing a user-defined function (UDF) as reported by Hosseini and Tafreshi (2010a).

To accurately simulate particle deposition, one needs to record the center-of-mass coordinates of the particles that deposit on the fibers or previously deposited particles. This is performed by developing two additional UDFs. The first UDF is implemented to mark the cells containing solid phase (any portion of a particle). The second UDF adds a sink term to the momentum equation in the marked cells, so that an artificial pressure drop is generated for the flow when passing through these cells. To mark the cells containing solid phase, a User Defined Memory (UDM), is defined. The process starts by assigning a zero to the UDM value of any computational cell that does not contain any solid phase. If the cell becomes filled with a deposited particle, we then change its UDM value to unity. Interested readers are referred to the work of Hosseini and Tafreshi (2012) for more details about our cell-marking procedure. It is worth mentioning that in our current work we add a sink term to the momentum equation in the marked cells, instead of increasing the air viscosity (the approach considered by Hosseini and Tafreshi 2012). The latter method was found to lead to simulations less susceptible to numerical divergence.

Note that, to avoid the formation of unrealistically long and chain-like particle dendrites on the fibers' surface, such as those in the simulations of Payatakes and Tien (1976), one has to inject the particles from randomly selected sites near the inlet boundary. Automated random injection has been implemented via an additional UDF (Hosseini and Tafreshi 2010c). Figure 2.2 shows an example of our dust-loaded fibrous media at different loading stages. The medium shown here has a fiber diameter of 1 μm, SVF of 7.5%, and is loaded with particles with a diameter of 1 μm.

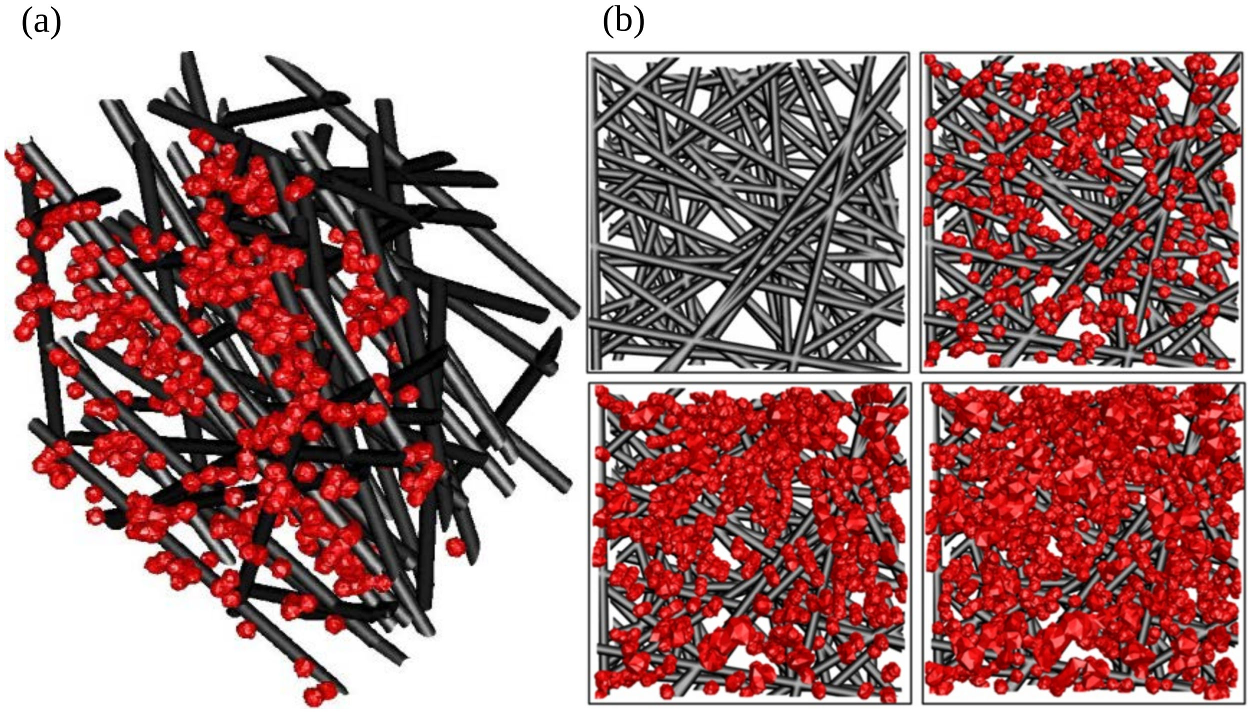

Figure 2.2: An example of our 3-D virtual loaded media at different stages of particle loading with a fiber diameter of 1μm and SVF of 7.5% loaded with 1μm-particles.

2.4 Mesh Independence

As mentioned earlier, 3-D microscale simulation of dust deposition in fibrous media is computationally expensive. It is obviously desirable to reduce the number of cells required for a given simulation. However, it is important to ensure that the grid size chosen for the simulations is not too coarse to affect the accuracy of the simulation results. In this concern, we considered a single fiber with a diameter of one micrometer inside a square domain and meshed it with different grid densities ranging from 5 to 35 mesh counts around the fiber's circular perimeter. To facilitate the comparison between these simulations, particles were injected from exact same locations at the inlet leading to almost identical particle dendrite formations in each case (see also Hosseini and Tafreshi, 2012). The pressure drop values before and after particle depositions are plotted in Figure 2.3 for two different SVFs of 2.5 and 10 percent. It can be seen that the influence of mesh density becomes almost insignificant for mesh counts greater than 15. It is also interesting to note that mesh-independence can be achieved at smaller mesh counts for the domains with lower SVFs. This is probably due to the fact that spatial flow gradients become stronger with increasing SVF (i.e., narrowing the flow passage) requiring better refined mesh distributions in the domain. In our simulations, we used fourteen grid points around the circular perimeter of a fiber for all cases considered as it seemed to be a reasonable trade-off point between accuracy and CPU time.

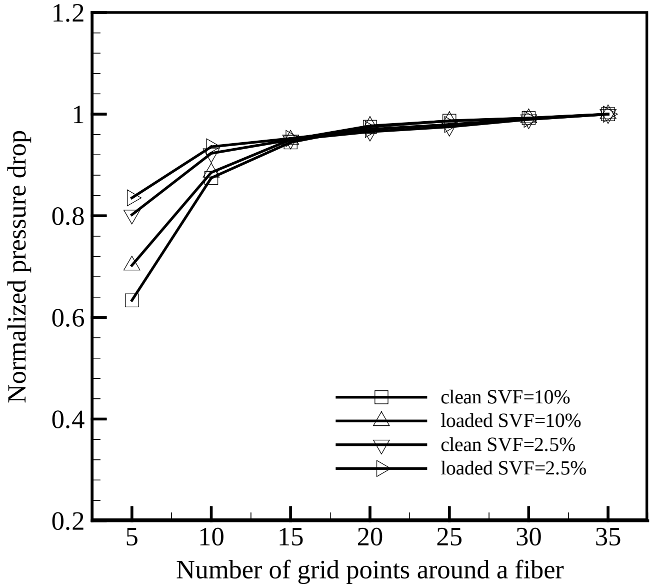

Figure 2.3: Normalized pressure drop a fiber with a diameter of 1 μm loaded with particles of 1 μm diameter. Two different SVFs of 2.5 and 10% are considered.

As mentioned earlier in the introduction, there are reliable expressions available for predicting pressure drop and collection efficiency for clean filter media. An example of such expressions for pressure drop (empirical correlation of Davies 1973) and collection efficiency calculations (Lee and Liu, 1982 and Brown, 1993) are given in Appendix A, and used here to validate our clean filter simulations (see Figure 2.4). In this figure, fibrous media with a fixed fiber diameter of 2 μm but different SVFs of 2.5, 5, and 7.5% are challenged with aerosol particles having a diameter of 1 μm and a velocity of 1 m/s. Good general agreement between our results and the empirical/semi-empirical correlations in the literature is evident. It must be noted that there exist no perfectly accurate expressions in the literature that one can use to benchmark the pressure drop or collection efficiency predictions of a numerical model (or that obtained from an in-house experiment). In fact, none of the available empirical expressions in the literature agree with one another (see the discussion in Hosseini and Tafreshi, 2010c) to an extent better than what is shown in Figure 2.4. On this basis, we consider any simulation data that are within some 20% margin of these empirical correlations as validated.

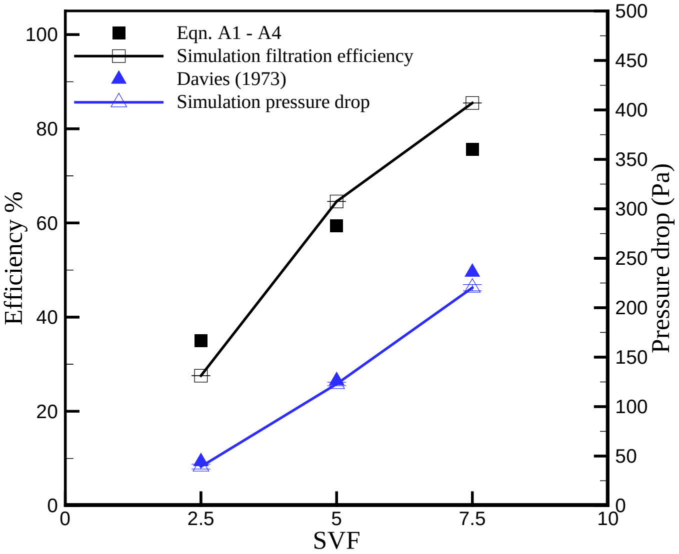

Figure 2.4: Pressure drop and collection efficiency for clean filter media with different SVFs of 2.5, 5, and 7.5% compared with the predictions of the existing semi-empirical correlations from literature (equations in A1-A5 in Appendix A).

2.3. Macroscale Modeling of Dust Deposition in 1-D Fibrous Media

Existing methods for predicting the performance of a dust-loaded filter are generally based on some 1-D macroscale representation of a fibrous filter that uses cell-model-type expressions for SFE and pressure drop calculations. An example of such models includes, but is not limited to, the work of Thomas *et al.* (1999, 2001) who developed a numerical model based on dividing a fibrous filter into some thin layers (each having their own averaged properties, e.g., porosity), and using the existing cell-model-type expressions (e.g., those given in Appendix A) for SFE and pressure drop calculations in each layer. As will be discussed later in this Chapter, such macroscale models, due to their over-simplified representation of the dynamic changes of a filter's microstructure, often need some ad-hoc case-dependent correction factors or assumptions in their formulations that limit their applications to the specific filtration problem for which they are developed.

We developed a MATLAB implementation of the macroscale model of Thomas *et al.* (2001) with some minor modifications. This model assumes a filter to be made up of a series of thin homogeneous layers each treated as individual filter media. For the sake of simplicity, this model assumes that particle dendrites, formed on the surface of the fibers, act like additional fibers with a diameter equal to that of the particles. Therefore, each layer has two types of collectors, one is made of the actual fibers and the other is made of the deposited particles. The particle collection efficiency in each layer and at each pseudo time-step (i.e., each particle batch injection) is obtained using the aforementioned semi-empirical expressions given in Appendix A. Particles filtered in each layer are assumed to contribute to the SVF of the layer (increasing with time). The 1-D nature of this model does not allow for a given layer to reach an SVF greater than that of the layer before it, i.e., mass deposition monotonically decreases with thickness, as expected. Therefore, when SVF of the first layer reaches a given maximum allowable value, any additional particle deposition will be considered as surface deposition on the face of the filter. We defined a maximum allowable SVF for each layer using the empirical correlation of Kasper *et al.* (2010) reported for mono-dispersed particle cakes,

$$\varepsilon_c = 0.36 + 0.64 \exp(-0.29 \rho_p d_p / \rho_w) \tag{2.4}$$

where d_p is the particle diameter in micrometers and $\alpha_{\max} = (1-\varepsilon_c)$. The total pressure drop of the filter is the summation of the pressure drop values in each layer plus the pressure drop caused by the cake (if any). The total efficiency of the filter is obtained by adding up the mass deposited in each layer divided by the total amount of mass injected at the inlet. The pressure drop caused by particles deposited on the filter surface and those deposited in depth are calculated based on the expression of Bergman (1978) developed for both depth and surface filtration,

$$\Delta p_t = 16\mu U_0 z(2\alpha_f / d_f + 2\alpha_{p,t} / d_p)(1+56(\alpha_f + \alpha_{p,t})^3)\sqrt{4\alpha_f / d_f^2 + 4\alpha_{p,t} / d_p^2} \tag{2.5}$$

It is important to mention that the algorithm proposed by Thomas *et al.* (2001) assumes that the aerosol particles are either captured by the actual fibrous filter or by the fictitious fibrous media made up of the particle dendrites. The mass fraction flowing through the former and latter media are intuitively, but not mathematically, assumed by these authors to be proportional to $1-(\alpha_p / (1-\alpha_f))$ and $\alpha_p / (1-\alpha_f)$, respectively. Our macroscale model implementation is shown with greater details in a flowchart in Figure 2.5.

2.4. Results and Discussion

As mentioned before, with the continuing rate of advancement in manufacturing fast computers, one can expect 3-D microscale simulations to become the common method of filter design in the near future. Being developed based on first principles, these models are self-sufficient (do not need empirical correction factors), and their predictions can directly be used for product design. To provide a comparison between the results of our 3-D microscale simulations and the aforementioned 1-D macroscale model, we simulated media with a constant fiber diameter of 2 µm but three different SVFs of 2.5, 5 and 7.5% (three common SVFs for fibrous filters). We challenged these virtual filters with dust particles having a velocity of 1 m/s and a diameter of 1 μm.

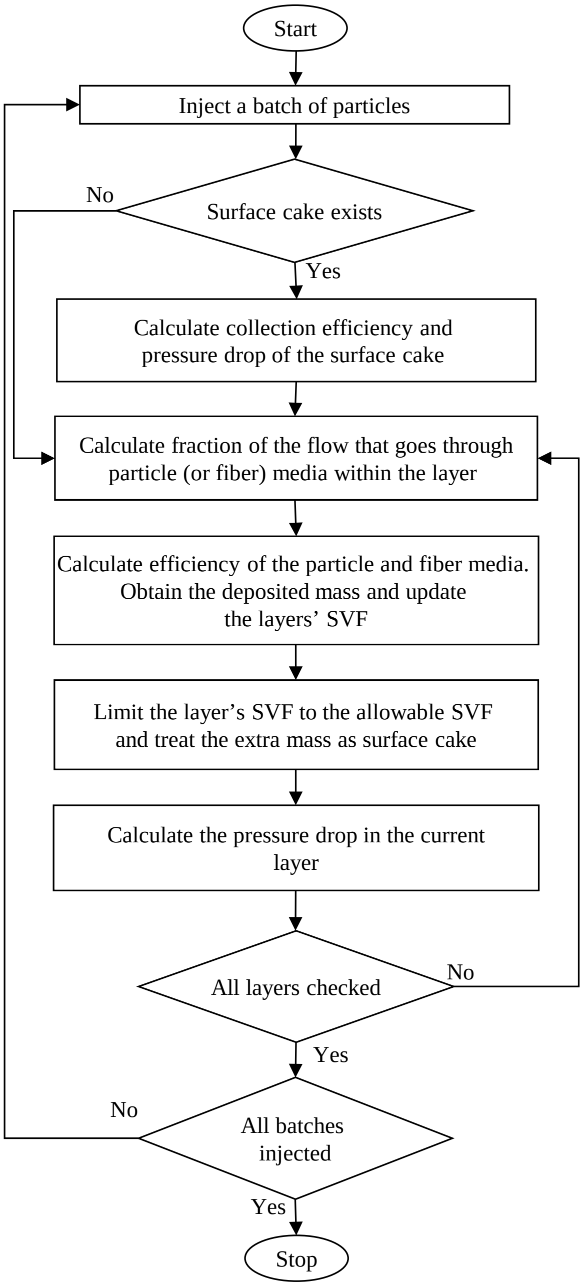

Figure 2.5: Calculation's flow chart for our 1-D macroscale model.

Figure 2.6a shows a comparison between the predictions of the instantaneous pressure drop values versus the mass of the deposited particles per unit surface area of the filter obtained from 3-D microscale and 1-D macroscale simulations. To produces these results, we injected as many particles as needed to reach a collection efficiency of 100%, as can be seen in Figure 2.6b (obviously, more particles are needed for filters with lower SVFs).

In order for the results of 1-D macroscale simulations to somewhat agree with those of the 3-D microscale simulations, we had to consider two major assumptions. Following the statement made by Bergman *et al.* (1978) that the parameter d_p in Equation 2.5 is not necessarily equal to the particle diameter, we used a value of 3μm for d_p even though the particles considered for the simulations are 1μm in diameter.

Also, in our 1-D macroscale algorithm, we had to assume that the filter is made of one single layer (which can be justified considering the filters simulated here are very thin). With these assumptions, the pressure drop values from the 1-D model came to close agreement with those of 3-D simulations, especially for higher SVFs. Nevertheless, for the media with an SVF of 2.5%, the macroscale model estimates an earlier transition from the depth filtration to the surface filtration regime. This could be due to our assumption of media being composed of one single layer only. However, increasing the number of layers in this 1-D model affects the agreement between the microscale and macroscale simulations at other SVFs. Note that we did not attempt to load our virtual filters beyond a collection efficiency of 100%, where the pressure drop is expected to increase linearly with the mass of deposited particles, as that was beyond the objectives of our current work.

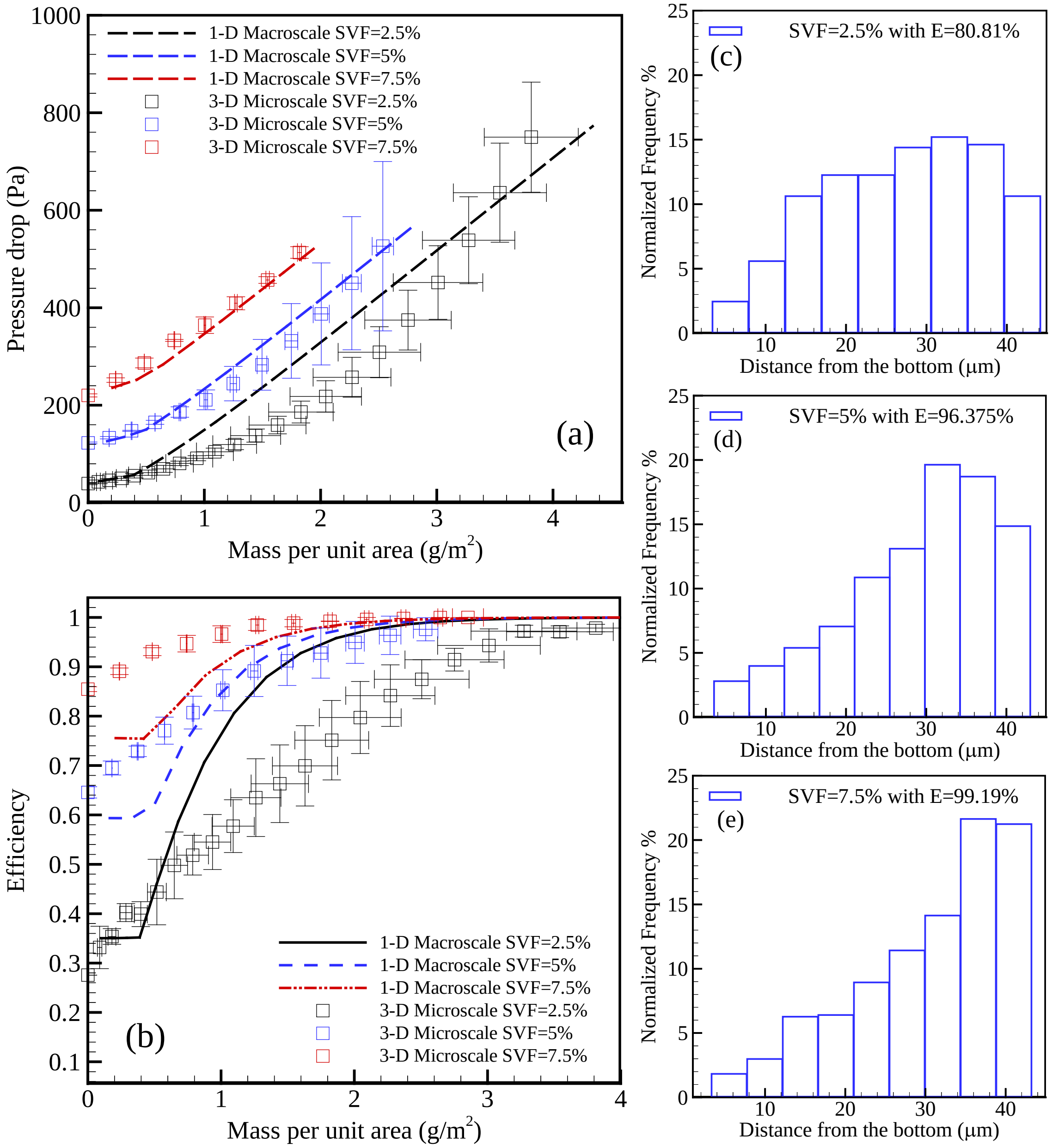

Figure 2.6: Comparison between pressure drop (a) and collection efficiency (b) values obtained from 1-D macroscale and 3-D microscale simulations at different mass depositions for media with a fiber diameter of 2 μm but SVFs of 2.5, 5, and 7.5%. Mass deposition profiles across the thickness of the filter media with SVFs of 2.5% (c), 5% (d), and 7.5% (e) are shown at a mass deposition of 2 g/m^2.

In interpreting the collection efficiency results shown in Figure 2.6b, note that there exist some differences in the predictions of the 3-D and 1-D models even at zero mass deposition (i.e., clean filter), as was discussed earlier in relation to Figure 2.4. Obviously the above differences eventually vanish as all collection efficiencies eventually reach a common value of 100%.

However, in the case of media with an SVF of 2.5%, this discrepancy seems to increase before it starts to decrease, i.e., 1-D simulations tend to be less accurate.

For completeness of the study, we have also presented the mass deposition profile across our virtual media for a total deposition mass of 2 g/m^2 in Figure 2.6c–2.6e; obviously, more depth-deposition has taken place in media with lower SVFs. At a loading mass of 2 g/m^2, we have also obtained the instantaneous collection efficiencies for media with SVFs of 2.5, 5, and 7.5% to be 81, 96, and 99%, respectively.

2.5. Chapter Conclusions

Two different approaches were considered in this chapter for simulating the unsteady-state pressure drop and collection efficiency for fibrous filters loaded with mono-dispersed aerosol particles. The first approach is a computationally inexpensive 1-D macroscale model developed based on the studies reported in the literature, and uses cell-model-type semi-empirical (and/or semi-analytical) expressions for pressure drop and collection efficiency predictions. The second approach is a computationally-expensive 3-D microscale model, which produces a realistic representation of the particle loading and its evolution over time. A close comparison between the results of 1-D macroscale and 3-D microscale simulations indicates that while the former requires a series of ad-hoc or case-dependent correction factors before it can produce accurate predictions for the instantaneous pressure drop or collection efficiency of a fibrous filter under dust-loading. The 3-D microscale simulation method proposed in this study, in contrast, is self-sufficient, as it is developed based on first principles, and can potentially replace the traditional design methods currently used in industry for product development.

Chapter 3

Modeling Service Life of Pleated Filters Exposed to Poly-Dispersed Aerosols[5]

3.1 Introduction

With the current computational power, it is practically impossible to devise a 3-D microscale simulation discussed in the previous chapter to model the deposition of aerosol particles in a pleated filter. Therefore, macroscale models that can be used to simulate the performance of dust-loaded pleated filters have been developed for the past few years (the term macroscale simulation is used here to refer to simulations on scales comparable to the dimensions of the filter, i.e., scales 3–4 orders of magnitudes larger than those of microscale simulations). In a paper by Fotovati *et al.,* 2011, we simulated the effects of dust-cake formation on the pressure drop of a pleated filter under the surface filtration regime (e.g., pleated HEPA media). An improved simulation method was later developed by Fotovati *et al.*, 2012 to model the particle capture and pressure of a filter under the depth filtration regime on the macroscales (e.g., pleated pre-filters). The work in this chapter contributes to the state of the art in modeling dust-loaded pleated filters by 1) combining the above two algorithms (surface and depth depositions) into one unified simulation scheme that can be used to simulate performance of pleated filters with no limitation on the

---

[5] Contents of this chapter appear in the following publication:
A.M. Saleh, S. Fotovati, H.V. Tafreshi, B. Pourdeyhimi, Modeling service life of pleated filters exposed to poly-dispersed aerosols, Powder Technol. 266 (2014) 79–89.

deposition regime, 2) extending the above algorithms to 3-D so that one can correctly model the clogging of a pleated filter (an inherently 3-D phenomenon by its nature), and most importantly 3) developing the formulations required for modeling the performance of pleated filters under poly-dispersed dust-loading.

In the next sections, we first present the governing equations for the flow of air and particles in a pleated filter in Section 3.2, and then discuss the methodology that we have developed for simulating pleated media loaded with poly-dispersed dust particles in Section 3.3. In Section 3.4, we present a brief parameter-study conducted to demonstrate the capabilities of our model. This is followed by our conclusions of this chapter in Section 3.5.

3.2. Flow Field and Particle Trajectory Calculations

The governing equation for the flow of air in a pleat channel is the Navier–Stokes equation:

$$\frac{\partial u_i}{\partial x_i} = 0 \tag{3.1}$$

$$u_i \frac{\partial u_j}{\partial x_i} + \frac{1}{\rho}\frac{\partial p}{\partial x_j} = \upsilon\left(\frac{\partial^2 u_j}{\partial x_i \partial x_i}\right) \tag{3.2}$$

The Fluent code has been adopted as the platform for our simulations and is enhanced with in-house subroutines whenever needed. The convective terms of the Navier–Stokes equations become negligible for the air flow inside the fibrous structure of a filter. The fibrous media of the filter is modeled as a porous zone with a given permeability tensor. Fluent assigns an artificial pressure drop (momentum sink) to the cells located in the porous zone. This pressure drop is calculated based on a permeability tensor that is input to the code. The above pressure gradient in the x, y, and z directions is defined as:

$$\frac{\partial p}{\partial x_i} = \frac{\mu}{k_{ij}} u_j \tag{3.3}$$

where k_{ij} is the permeability tensor of fibrous media. The elements of the permeability tensor k_{ij} depend on the pleat angle, and can be found from the principal permeability values. We assume that the fibrous media are layered (Wang *et al.*, 2007; Fotovati *et al.*, 2010). Therefore, the media's permeability tensor in the principal directions (i.e., the through-plane k_{TP} and in-plane k_{IP} permeability constants) can easily be obtained from the expressions of Spielmann and Goren, 1968:

$$\frac{1}{4\alpha} = \frac{1}{4} + \frac{3}{2}\frac{\sqrt{k_{IP}}}{d_f}\frac{K^1(\mathrm{d}_f/(2\sqrt{k_{IP}}))}{K^0(\mathrm{d}_f/(2\sqrt{k_{IP}}))} \tag{3.4}$$

$$\frac{1}{4\alpha} = \frac{1}{2} + \frac{2\sqrt{k_{TP}}}{d_f}\frac{K^1(d_f/(2\sqrt{k_{TP}}))}{K^0(d_f/(2\sqrt{k_{TP}}))} \tag{3.5}$$

where K^0 and K^1 are the modified zeroth and first order Bessel functions of the second kind.

A Lagrangian approach is considered to track particles and determine their paths through the filter. In this approach, Eqn. 2.3 is the equation for the balance of forces exerted on a particle is integrated to obtain the particle's velocity and position over time (Brownian forces are negligible for the particle diameters considered in this study, 1–10 µm).

In order to avoid the formation of unrealistic dendrites with ordered microstructures, the particles are injected in the simulation domain from random points at the inlet by developing a User-Defined Function as discussed previously by Hosseini and Tafreshi 2010, 2011 (also refer to the previous chapter about the discussion on enhancing Fluent for particle capture via interception).

After injecting a certain number of particles, referred here as batch-injection, the flow field is recalculated.

Formation of dust-cake, either on the surface or on the inside of a fibrous filter, is very slow process in real-life. Thousands of particles (or millions, depending on their size) are needed to build up a macroscopically measurable dust-cake. Similarly, a computer simulation of dust-cake formation requires a very long CPU time. To expedite this process, we have developed a “cluster” injection method in which a group of particles in the discrete particle tracking is modeled as a cluster of imaginary particles with the same particle diameter (Fotovati *et al.*, 2012). It is then assumed that the cluster continuously loses a fraction of its mass (i.e., some of its particle content) as it travels through the filter (or an existing dust-cake). The number of imaginary particles grouped into a cluster is designed to be an input depending on the actual size of the particle and the desired CPU time. Injecting a cluster containing, for example, 100 imaginary particles and tracking its trajectory throughout the filter replaces the process of tracking the trajectories of 100 particles with the same diameter injected from the exact same point at the inlet. This numerical treatment helps to shorten the CPU time required to simulate the formation of a dust-cake by orders of magnitudes. The treatment, however, can affect the morphology of the dust-cake. If the number of particles grouped in a cluster is too high, the resulting dust-cake can become unrealistically non-uniform. Therefore, depending on the level of accuracy required to achieve the objectives of a study and the acceptable computational cost, one can decide on the number of imaginary particles that can be grouped in a cluster. Note that this number also depends on the size of the computational mesh considered for the simulations. Generally speaking, the number of particles in a cluster should not be so high to max out the allowable Solid Volume Fraction (SVF) of a computational cell in one deposition (see the next section). After each batch-injection, the amount of mass deposited in the filter is used to calculate the instantaneous collection efficiency. The permeability of the cells in the porous zone is also updated using the amount of mass deposited to obtain the instantaneous pressure drop of the filter.

3.3. Flat-Sheet Filters Loaded with Poly-Dispersed Dust

The formulations presented here allow one to take the effect of particle size polydispersity into consideration when simulating the performance of a particle-loaded pleated filter, for the first time. To do so, we divide a given particle diameter distribution into 10 mono-dispersed sub-groups with different weight factors. We assign a User Defined Memory (UDM) to each sub-group for each cell. This is considered so that the number of particles n_i (subscript i refers to the particles having a particle diameter of d_i) is available for calculating a geometric average diameter d_g and geometric standard deviation σ_g for the deposited particles in a cell. With this information, one can calculate the instantaneous SVF of the cells during the simulation using the geometric standard deviation as

$$\ln d_{pg} = \frac{\sum n_i \ln d_i}{N} \tag{3.6}$$

$$\ln \sigma_g = \sqrt{\frac{\sum n_i (\ln d_i - \ln d_{pg})^2}{N-1}} \tag{3.7}$$

where N is the total number of particles in a cell. The geometric average diameter is also used along with the geometric standard deviation to calculate the permeability of the cells containing poly-dispersed particles as will be discussed later.

The SVF for each cell can be estimated by knowing the amount of deposited mass in that cell and the cell volume. The maximum allowable SVF α_{max} in a cell is obtained based on the diameter of the deposited particles, using the equation proposed by Kasper *et al.*, 2010.

$$\alpha_{\max} = 1 - \left\{0.36 + 0.64\left[\exp(-0.29\rho_p d_{pg} / \rho_w)\right]\right\} \tag{3.8}$$

As mentioned earlier, the flow field is recalculated after injecting each batch of clusters. Before flow recalculation, the permeability of the computational cells containing deposited mass is updated. The next section presents our proposed formulations for obtaining these permeability values. For clarity of the presentation, we first discuss our procedure for modeling surface filtration in Section 3.3.1, and then present our combined surface-and-depth filtration algorithm in Section 3.3.2.

3.3.1 Surface Filtration with Flat-Sheet Filters

The pressure drop of a dust-cake formed on the surface of a flat-sheet filter can be studied using the following equation Rudnick and First, 1978:

$$\Delta P_c = K_2 V \frac{M_c}{A_c} \tag{3.9}$$

where K_2 is the specific cake resistance, V is the air velocity, and M_c / A_c is the cake mass per unit area. The specific cake resistance can be obtained from the empirical correlations of Rudnick and First, 1978 or Kozeny–Carman (Carman, 1956) given in Equations 3.10 and 3.11, respectively.

$$K_2 = \frac{18\mu}{\rho_p d_p^2 c^c} \frac{3 + 2(1-\varepsilon)^{5/3}}{3 - 4.5(1-\varepsilon)^{1/3} + 4.5(1-\varepsilon)^{5/3} - 3(1-\varepsilon)^2} \tag{3.10}$$

$$K_2 = \frac{180\mu}{\rho_p d_p^2 c^c} \frac{(1-\varepsilon)}{\varepsilon^3} \tag{3.11}$$

where c^c is the Cunningham slip correction factor and ε is the cake porosity. Representing the cake mass as $M_c = \rho_p A_c L_c (1-\varepsilon)$, Equations 3.10 and 3.11can be used together with Darcy's law $V = k_g \Delta P_c / (\mu L_c)$ to obtained permeability expressions for the dust-cake.

$$\frac{1}{k_g} = \frac{18(1-\varepsilon)}{d_p^2 c^c} \frac{3+2(1-\varepsilon)^{5/3}}{3-4.5(1-\varepsilon)^{1/3}+4.5(1-\varepsilon)^{5/3}-3(1-\varepsilon)^2} \tag{3.12}$$

$$\frac{1}{k_g} = \frac{180}{d_p^2 c^c} \frac{(1-\varepsilon)^2}{\varepsilon^3} \tag{3.13}$$

The equation of Rudnick and First, 1978 is implemented in our simulations to calculate the permeability of the cells containing mono-dispersed particles.

Gupta *et al.*, 1993 modified the expression of Rudnick and First, 1978 such that it becomes applicable to poly-dispersed cakes. Using the specific cake resistance expression of Gupta *et al.*, 1993, we obtain:

$$\frac{1}{k_{poly}} = \frac{18(1-\varepsilon)}{d_{pg}^2 c^c} \exp(-4.0 \ln^2 \sigma_g) \frac{3+2(1-\varepsilon)^{5/3}}{3-4.5(1-\varepsilon)^{1/3}+4.5(1-\varepsilon)^{5/3}-3(1-\varepsilon)^2} \tag{3.14}$$

Figure 3.1 shows our algorithm for modeling surface filtration (particles cannot penetrate into the filter, i.e., collection efficiency is 100%) with mono- or poly-dispersed particles in the form of a flowchart. As can be seen, the cell model equations (written for a granular bed, see Appendix B) are solved inside each computational cell to calculate the mass of the deposited particles, if a cluster's trajectory encounters the dust-cake. Otherwise, if the cluster reaches the surface of the filter, its entire mass is deposited in the cells adjacent to the filter surface. When the SVF of a cell reaches α_{max}, it is then considered to be blocked, and the incoming clusters will have to deposit in the cells upstream to this blocked cell.

The resistance of the cells containing a deposit can be calculated using Equations 13–15 for mono- or poly-dispersed particles. These instructions are provided to Fluent code via a series of in-house User-Defined Functions (UDFs). The UDFs first check for an interception between a traveling cluster and the blocked cells in the dust-cake (or the cells assigned to the fibrous media in the case of surface filtration). If such encounter is detected, the entire mass of the cluster will be deposited in the cell that hosts the cluster. If no encounter is detected, then the fraction of the cluster's mass that should be deposited in cells along its trajectory is calculated using equations B.1–B.5. The distance that a cluster travels inside each cell is recorded to obtain the total length of the cluster's trajectory inside the cake. At the end, the mass of the deposited particles is recorded in a User-Defined Memory (UDM), and used to assign a new SVF to the marked cells. For poly-dispersed dust, the geometric particle diameter and standard deviation are calculated for the particles deposited in each cell and used in Equation 3.14 for permeability calculation.

As mentioned earlier in this section, the concept of using clusters instead of actual particles is a numerical treatment considered here to accelerate the dust-cake formation. The choice of the cluster mass (the number of particles grouped in a cluster) can influence the accuracy of the numerical values obtained from the simulations. This parameter is left to be chosen by the modeler in trading accuracy for CPU time. It is therefore, recommended to calibrate the simulations with an experiment to determine the error associated with a given cluster mass for simulating a given dust-filter combination (without a calibration one can only expect qualitative predictions from the model).

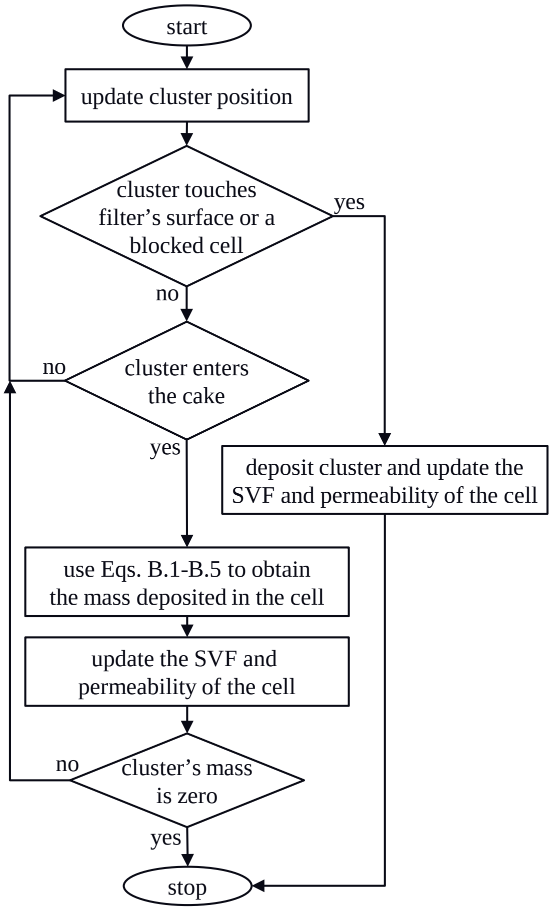

Figure 3.1: The flowchart for modeling surface filtration.

Once the simulation is calibrated, one can use it to simulate different filter geometries and aerodynamic conditions. As mentioned in the Introduction section, we have developed accurate microscale simulations for predicting the collection efficiency and pressure drop of flat-sheet fibrous media under loading (Saleh *et al.*, 2013). Being CPU-intensive, such 3-D microscale simulations are not suitable for simulating filters on scales comparable to the dimensions of a pleated filter, but they are very valuable in benchmarking the accuracy of our macroscale simulations for pleated media. In this Chapter, we use both the experimental data and microscale simulation results (Section 3.3.2) for calibrating our macroscale models.

To calibrate our macroscale model with experiment, we set up a simple 3-D simulation domain as shown in Figure 3.2a. We considered a flat-sheet filter loaded with mono-dispersed particles of 1 μm diameter. An example of a simulated dust-loaded flat sheet is shown in Figure 3.2b. We compared the instantaneous pressure drop of our simulations with the predictions of the empirical correlations given in Equations 3.10 and 3.11. As mentioned before, the choice of cluster mass should be in relation to the volume of the computational cell used in the simulation. For a mesh volume of 3.5×10^{-3} mm^3, we found a cluster volume of 2.4×10^{-5} mm^3 (corresponding to a cluster-to-cell volume ratio of 0.007) resulting in good agreement between the predictions of our model and the above correlations (see Figure 3.2c).

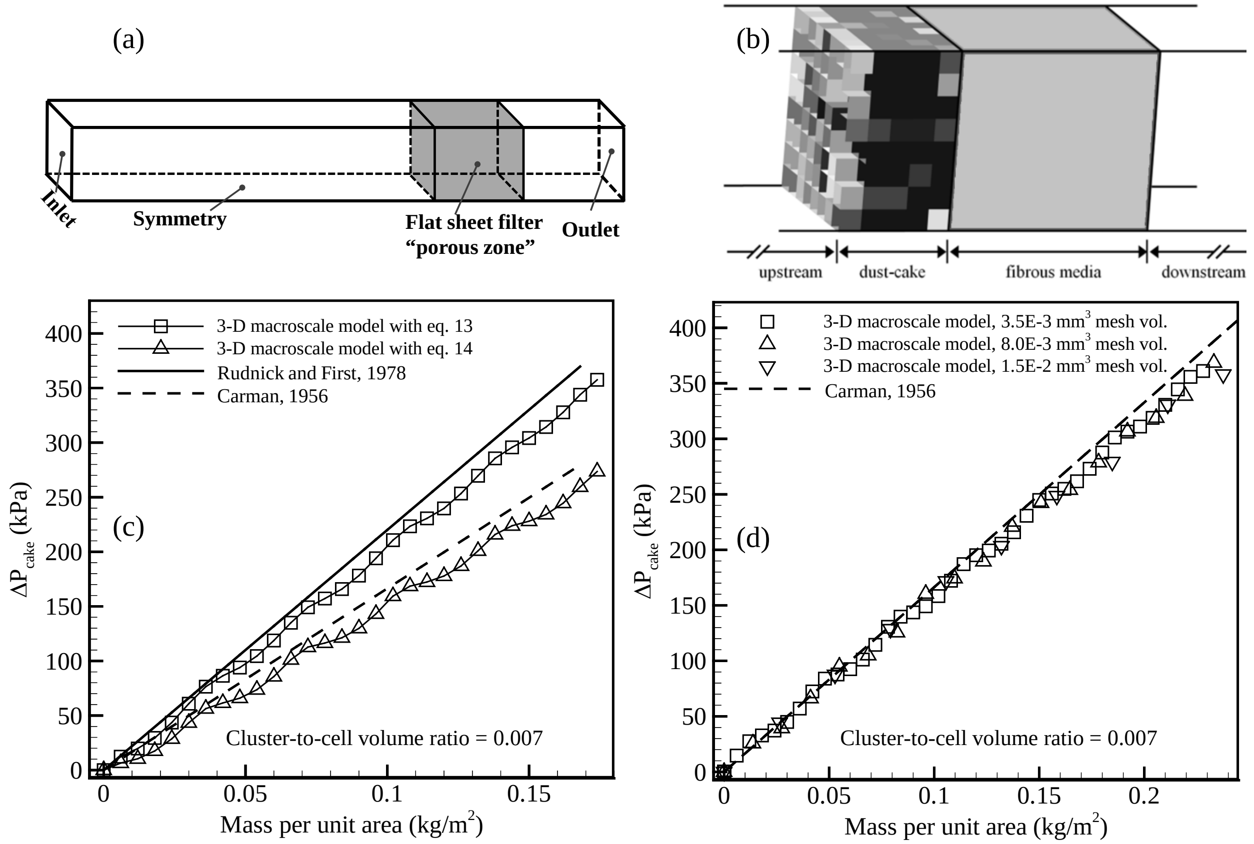

Figure 3.2: Simulation domain for modeling particle deposition on flat-sheet media (a). A dust-cake example composed of mono-dispersed particles of 1 μm diameter at a face velocity of 1 m/s formed on the surface of a flat-sheet filter (b). Model calibration using empirical correlations of Rudnick and First, 1978 and Kozeny–Carman (Carman 1956) resulting in a cluster-to-cell volume ratio of 0.007 (c). Effects of mesh volume on pressure drop prediction for a constant cluster-to-cell volume ratio of 0.007 (d).

In order to further demonstrate the uniqueness of the above-mentioned cluster-to-cell volume ratio, we increased the cell dimensions from 3.5×10^{-3} mm^3 to 8×10^{-3} and 1.5×10^{-2} mm^3 and repeated the simulation with cluster volumes of 5.5×10^{-5} and 10.6×10^{-5} mm^3, respectively (maintaining the same cluster-to-cell volume ratio) in Figure 3.2d. It can be seen that once the cluster mass is obtained through calibration with a given mesh density, further increase or decrease of the mesh will not affect the results, as long as the cluster-to-cell volume ratio is held constant.

For completeness of the study, in Figure 3.3, we present another calibration study in which we simulated the experiment of Cheng and Tsai, 1998 conducted for poly-dispersed limestone particles with a mass mean aerodynamic average diameter of 2.66 µm and a geometric standard deviation of 2.1 (note that Cheng and Tsai , 1998 did not discuss the properties of their filters, indicating that the reported pressure drop values are for the cake only). The volume of the cluster was set to be 2.4×10^{-3} mm^3 for a mesh volume of 3.5×10^{-3} mm^3.

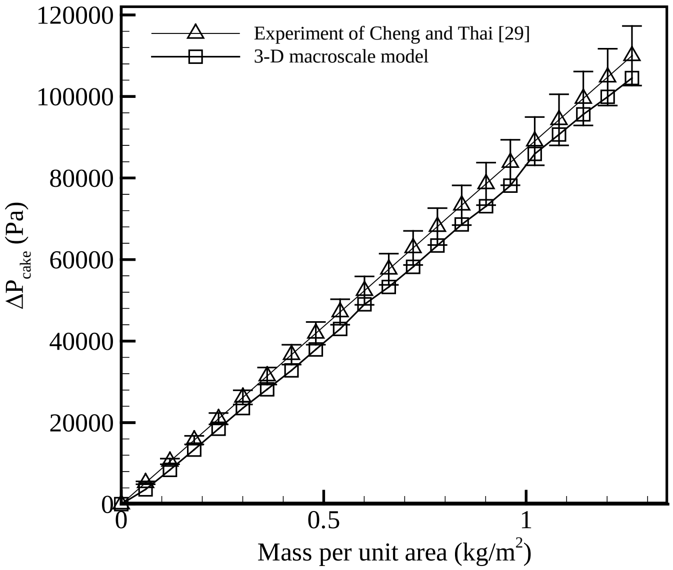

Figure 3.3: Pressure drop of a flat-sheet filter loaded with poly-dispersed particles with a mass mean aerodynamic diameter of 2.66 µm and a geometric standard deviation of 2.1 at an air velocity of 0.9 cm/s devised to simulate the experiment of Cheng and Tsai, 1998 for model calibration.

3.3.2 Combined Depth and Surface Filtration with Flat-Sheet Filters

Our algorithm for particle tracking and particle deposition in combined depth and surface filtration regimes is presented in the flowchart shown in Figure 3.4. The algorithm is very similar to the one shown in Figure 3.1, except that this algorithm the clusters are allowed to enter and deposit inside the fibrous media. When a cluster enters the fibrous domain the cell-model equations (Equations C.1–C.3 from Appendix C) are solved inside each computational cell to obtain the mass of the deposited particles. In the absence of more accurate estimates, we assumed the maximum allowable SVF in a fibrous zone to be the same as the value used for the granular zone (see Equation 3.8).

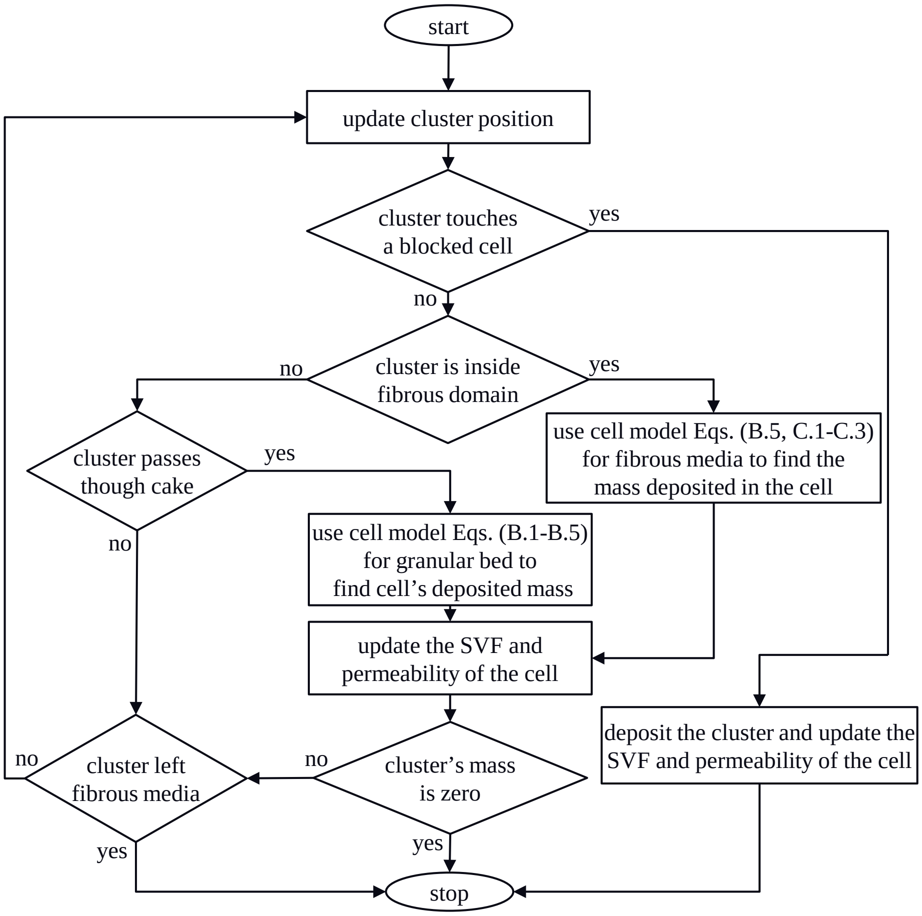

Figure 3.4: The flowchart for modeling the combined depth and surface filtration regimes.

For the cells located inside the fibrous zone containing particle deposits, the cell's resistivity (inverse of permeability) due to particles should be added to that caused by the fibers. The latter is calculated using the expressions of Spielmann and Goren, 1968 in this work, as mentioned earlier. There are several formulas in the literature for calculating the permeability of porous media comprised of different solid components, like fibers and particles (Clague and Phillips, 1998; Mattern and Deen, 2007; Tafreshi *et al*, 2009). In our preliminary investigations, we observed consistent pressure drop predictions with the un-weighted resistivity (Equation 3.15) and the volume-weighted resistivity (Equation 3.16) formulations of Mattern and Deen, 2007 (also see Tafreshi *et al.*, 2009 for additional information):

$$\frac{1}{k_{tot}} = \frac{1}{k_1(\phi_1)} + \frac{1}{k_2(\phi_2)} \tag{3.15}$$

$$\frac{1}{k_{tot}} = \frac{\phi_1}{\phi_{tot}} \frac{1}{k_1(\phi_{tot})} + \frac{\phi_2}{\phi_{tot}} \frac{1}{k_2(\phi_{tot})} \tag{3.16}$$

where ϕ_1 and ϕ_2 are the SVF of the fibrous and granular mass in a cell, respectively, with k_1 and k_2 representing their corresponding permeability values. In Equation 3.16, ϕ_{tot} is the overall SVF of the cell (both permeability values are calculated using ϕ_{tot} and weight-averaged according to their corresponding volume fractions). With the mass deposited in each cell recorded, the total resistivity of the particle-loaded fibrous media can be obtained using either of the un-weighted or the volume weighted resistivity equations (Equation 3.15–3.15).

As mentioned earlier, microscale simulations are expected to be significantly more accurate than the macroscale models. In the absence of experimental data, one can use microscale models to calibrate (even validate in many cases) the macroscale models. To demonstrate this, we use the results of the microscale 3-D simulations of Chapter 1 (Saleh *et al.* 2013) to calibrate our macroscale model for a flat-sheet filter having a fiber diameter of 2 μm loaded with particles with a diameter of 1 μm (see Figure 3.5a and 3.5b). The dimensions of the porous zone in the macroscale model are chosen such that they match the dimensions of the fibrous structure considered for the microscale simulations (a square side length of 55 μm and a thickness of 40 μm).

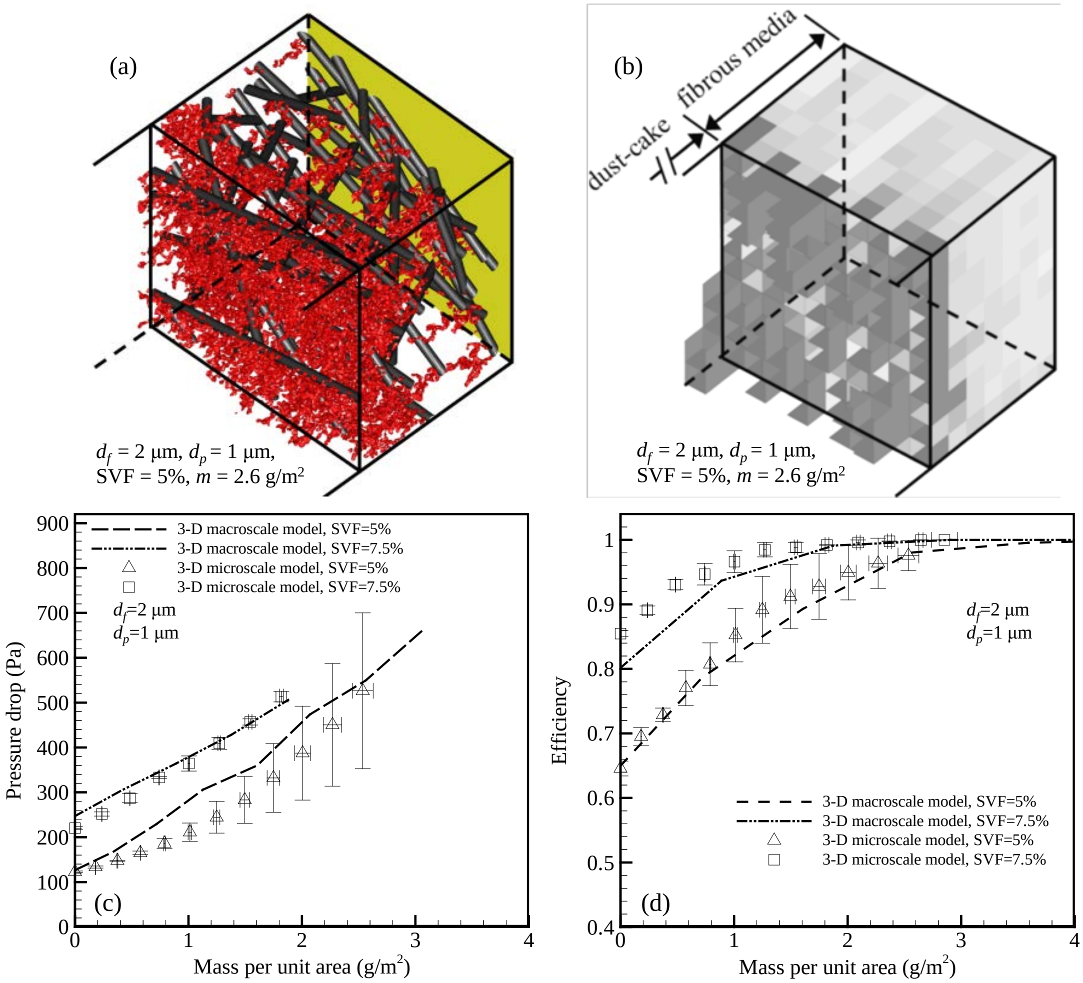

Figure 3.5: A comparison between 3-D microscale and 3-D macroscale simulation of flat-sheet filters with a fiber diameter of 2μm and SVFs of 5 and 7.5 % loaded with particles of 1μm diameter. A mass deposition of 2.6 g/m^2 on the filter with an SVF of 5% is shown on micro- and macroscales in (a) and (b), respectively. Instantaneous pressure drop (c) and collection efficiency (d) of the microscale simulations are used to calibrate the macroscale model.

Figure 3.5a and 3.5b show the deposition of 2.6 g/m^2 of particles on a flat sheet-filter having an SVF of 5%. Note that the deposition patterns are not exactly identical for two main reasons.

First, the fibrous zone in the macroscale model is a homogenous porous medium whereas the one in the microscale model is made of actual fibers with random in-plane orientations. Second, the particles in both simulations are injected from random cites at the inlet. In other words, the simulations are only statistically identical and one should only compare the ensemble average values obtained by repeating the simulations, as shown in Figure 5c and 5d. It was found that for a mesh volume of 170 μm^3 and a cluster volume of 52 μm^3 (corresponding to a cluster-to-cell volume ratio of 0.3) the macro- and microscale simulations agree well, as can be seen in Figure 5c and Figure 5d. Note also in these figures that two different SVFs of 7.5 and 5% have been considered, both having the same cluster-to-cell volume ratios.

3.4. Surface and Depth Deposition of Poly-Dispersed Dust in Pleated Filters

The main objective of this study is to provide a means of modeling the instantaneous performance of dust-loaded pleated filters over time. Triangular (V-shaped) pleats with different widths (or angles) but identical lengths of 25.4 mm are considered for the study presented here (see Figure 3.6). The depth in the z-direction is assumed to be 2.5 mm. Media thickness, SVF, fiber diameter, and inlet air velocity are assumed to be 0.7 mm, 7.5%, 15μm, and 0.5 m/s, respectively. All dimensions and parameters considered in our simulations are chosen arbitrarily, but are somewhat representative of a general dust-filtration application. Note that the inlet velocity is the velocity of the air at the entrance of the pleat channel and should not be confused with the face velocity, which is the velocity of air as it enters the fibrous medium. The aerosol mass concentration is assumed to be $C = 2.52 \times 10^{-7}$ kg/m^3 with its flux $\tilde{C}$ given as

$$\tilde{C} = C \cdot u_{in} \tag{3.17}$$

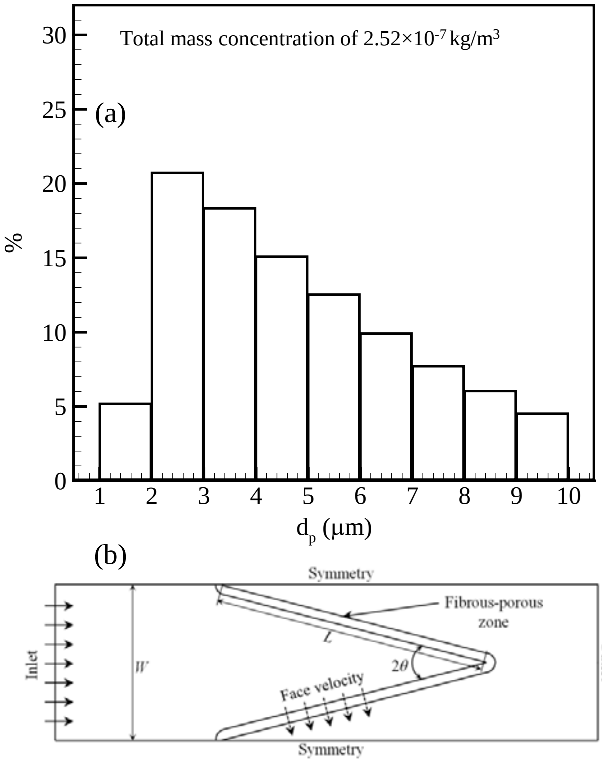

Figure 3.6: The mass distribution of the poly-dispersed aerosols used for simulating the pleated filters (a) along with the domain and boundary conditions considered for the simulations (b).

To demonstrate the capabilities of our macroscale model, three different aerosol flows have been considered in this study: mono-dispersed particles with a diameter of 1 µm, mono-dispersed particles with a diameter of 10 µm, and poly-dispersed particles with a diameter distribution between 1 and 10 µm having a mass average diameter of 4.77 µm. The mass distribution of the poly-dispersed aerosol particles is shown in Figure 3.6. To study the effects of pleat count on filtration performance, one should make sure that the number of clusters injected at each time step is obtained based on the inlet area of the filter (a variable dependent on the filter’s pleat count). This guarantees that the aerosol concentration flux is maintained constant when comparing filters with different pleat counts.

Figure 3.7 shows the pressure drop and collection efficiency (mass-based) of filters with 2 and 4 pleats per inch versus loaded mass per unit area (left column) and time (right column). It can be seen that, the rate of increase of pressure drop and collection efficiency is lower for filters with more pleats, as expected. It is often expected that pressure drop and collection efficiency values obtained for filters with different pleat counts collapse on top of each other when plotted versus mass per unit filtration area. This however, is only true if the flow patterns in filters with different pleat counts are exactly identical—a condition that may prevail in the early stages of dust loading only. It is also worth mentioning that by adding more pleats, one also adds more impermeable crease lines which in fact reduce the available air passage. For instance, increasing the pleat count by a factor of 2 does not decrease the face velocity by a factor of 2.

In Figure 3.7, note that the collection efficiency is almost 100%, independent of the loaded mass, for the filter challenged with particles with a diameter of 10 µm (Figures 3.7a and 3.7b). In contrast, collection efficiency of the same filter, when exposed to 1 µm-diameter particles, increases from less than 10% to 100% after collecting about 0.12 kg/m^2 of dust per unit filtration area (corresponding to about 150 and 200 days of operation for the filter with 2 and 4 pleats per inch, respectively), as can be seen in Figures 3.7c and 3.7d. The initial collection efficiency (mass-based) of the filter challenged with the aforementioned poly-dispersed aerosol falls between those obtained for 1 and 10 micrometer particles, and unlike the two other cases, is sensitive to the number of pleats (see Figures 3.7e and 3.7f). In Figure 3.7, it can also be seen that pressure drop in filters loaded with large particles (e.g., 10 µm particles) is less than that of the same filters loaded with small particles (e.g., 1 µm particles) for the same mass per unit filtration area (see Figures 3.7a, 3.7c, and 3.7e). This is simply because for a given mass the cake made of small particles has a higher surface area causing more friction with the air flow.

Expectedly, for the poly-dispersed particles, the pressure drop falls in between those of the two mono-dispersed extremes.

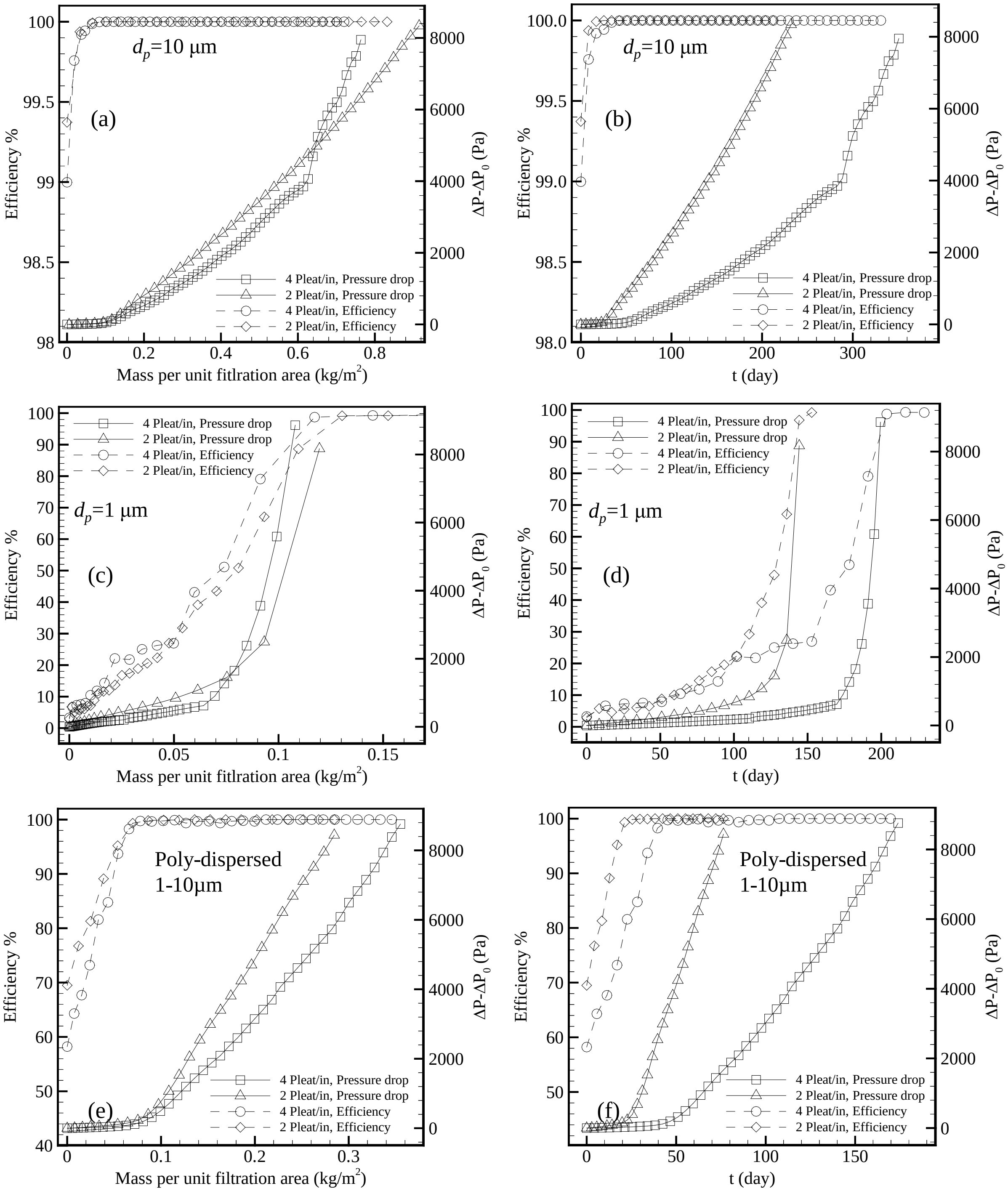

Figure 3.7: Instantaneous pressure drop and collection efficiency of filters with 2 and 4 pleats per inch with an inlet velocity of 0.5 m/s. Mono-dispersed aerosols with a particle diameter of 10 µm (a) and (b), mono-dispersed aerosols with a particle diameter of 1 µm (c) and (d), and poly-dispersed aerosols with a particle diameter of 1-10 µm (e) and (f).

Plotting the pressure drop and collection efficiency values versus time in service reveals additional information about the performance of a pleated filter. It can interestingly be seen in Figures 3.7b, 3.7d, and 3.7f that the pressure drop of the filters considered in our study increases faster when they are exposed to the poly-dispersed dust. For instance, the filter with 2 pleats per inch reaches a pressure drop of 6 kPa in about 190 days, if exposed to the aerosol flow with 10 µm particles, about 140 days, if exposed to the aerosol flow with 1 µm particles, and about 60 days, if exposed to the aerosol flow poly-dispersed particles. This indicates that the filters considered here reach the end of their service-life in less number of days when exposed to the poly-dispersed aerosol. To better understand the reason for this counter intuitive behavior note that the above filters have very low initial collection efficiencies when challenged with the 1 µm particles. This means that the cake made up of 1 µm particles grows very slowly with time. The same filters when exposed to 10-µm particles have very high (almost 100%) collection efficiencies, i.e., their cakes, made up of 10 µm particles, grow very quickly. On the other hand, a cake made up of 1 µm particles causes a lot more pressure drop than the one made of 10 µm particles with the same mass, as discussed earlier. Therefore, the interplay between the diameter of the particles in a cake and the rate by which the filter collects the particles (i.e., filter’s collection efficiency) leads a shorter service-life for the filters exposed to poly-dispersed aerosols.

It is also interesting to note that, increasing the number of pleats per inch from 2 to 4 significantly improved the service life of the filters considered in our study when challenged with the poly-dispersed aerosols. More specifically, increasing the number of pleats per inch from 2 to 4 increased the service life of the filter exposed to the poly-dispersed aerosols from about 60 days to about 140 days (a factor of 2.33) for a maximum pressure drop of 6 kPa. Similar increase in the number of pleats for the same pressure drop 6 kPa, increased the filters' service life from about 140 days to about 200 days (a factor of 1.43), for the aerosol flow with 1-µm particles, and from about 190 days to about 320 days (a factor of 1.68), for the aerosol flow with 10-µm particles (see Figures 3.7b, 3.7d, and 3.7f). The reason is that increasing the pleat count decreases the face velocity. As can be seen in the cell model calculation results shown in Figure 3.8, the initial collection efficiency of the filter considered here depends on the face velocity only when challenged with particles with a diameter between about 2 to 7 µm. For an inlet velocity of 0.5 m/s, theoretical face velocities of 0.125 and 0.0625 m/s can be obtained for the filters with pleat counts of 2 and 4 pleat per inch, respectively (neglecting the aforementioned impermeable fold line). Therefore, for particles with a diameter of 1 or 10 µm, the collection efficiency is not affected when increasing the number of pleats. However, for particles with a diameter of about 2 to 7 µm, increasing the pleat count reduces the collection efficiency due to inertial impaction, and consequently, the total initial filtration efficiency (see Figure 3.7f).

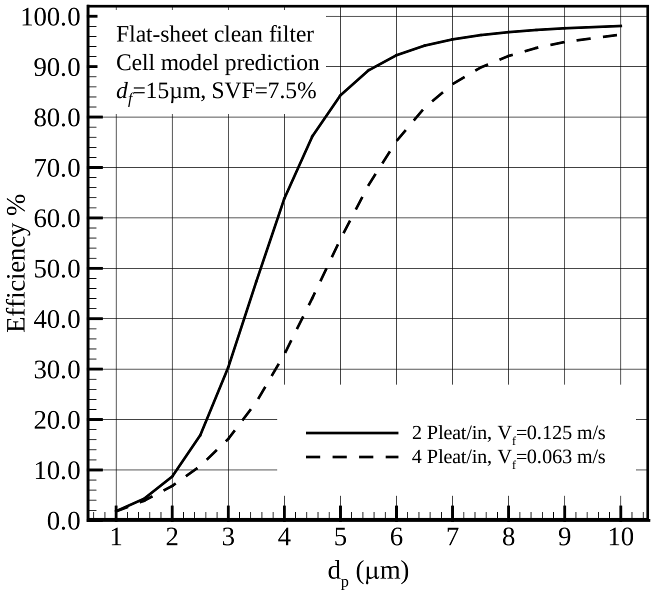

Figure 3.8: Initial (clean) collection efficiency predictions obtained using the cell-model equations for the flat-sheet filter discussed in Figure 7. Face velocities of 0.125 and 0.0625 m/s are used for when the pleat count is increased 2 to 4 pleats per inch.

Figure 3.9 shows the macroscopic dust-cake in filters discussed in Figure 7 at the moment when all the filters reached an instantaneous pressure drop of 8 kPa. The amount of deposited mass per unit filtration area (in kg/m^2) and the time in service (in days) are also shown in the figures for better comparison. The filter shown in the left column (Figures 9a, 9c, and 9e) and the ones shown in the right column (Figures 9b, 9d, and 9f) have a pleat count of 4/inch and 2/inch, respectively. The filters shown in the first, second, and third row in this figure are challenged with the 10 µm, 1 µm, and poly-dispersed aerosol flows, respectively. Note that deposition pattern becomes less uniform when decreasing the particle size or increasing the pleat count.

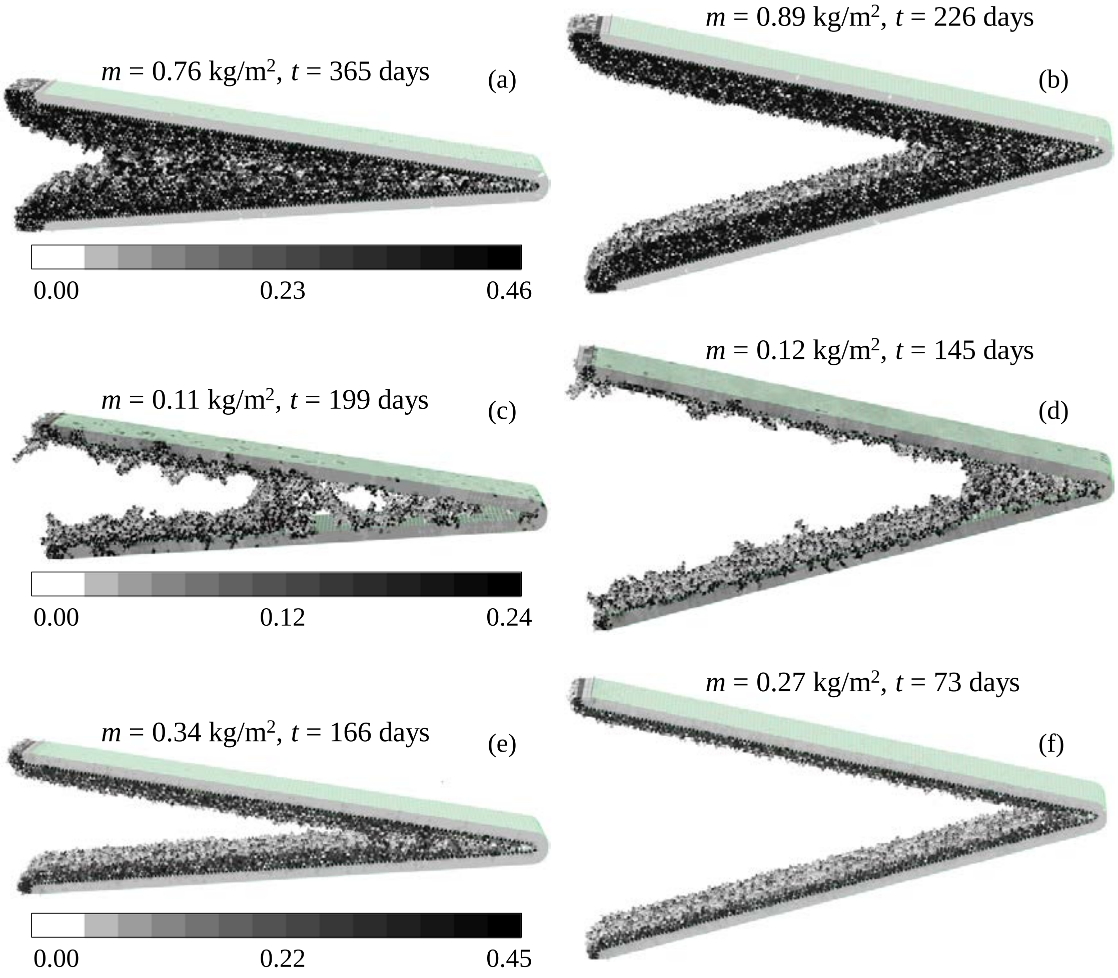

Figure 3.9: An example of 3-D dust deposition pattern in pleated filters with 4 and 2 pleats per inch challenged with different particle sizes at a pressure drop of 8 kPa and an air inlet velocity of 0.5 m/s. Mono-dispersed aerosols with a particle diameter of 10 µm (a) and (b), mono-dispersed aerosols with a particle diameter of 1 µm (c) and (d), and poly-dispersed aerosols with a particle diameter of 1-10 µm (e) and (f).

3.5. Chapter Conclusions

A CPU-friendly 3-D simulation method is developed to model the service life of pleated fibrous filters when challenged with mono- and poly-dispersed aerosols. The model is capable of simulating pressure drop and collection efficiency of such filters in both the surface and depth filtration regimes over time, and is suitable for parameter study and product design. The novelty of the macroscale simulation method presented here is that it is computationally fast, and therefore allows one to simulate and compare the lifecycle of pleated filters of different properties with one another. The method however, requires calibration with experiment or simulations conducted on smaller scales (i.e., more accurate simulations).

As an example, the lifecycle of an arbitrary filter with 2 and 4 pleats per inch is simulated when challenged with poly-dispersed particles having diameters in the range of 1 to 10 µm, as well as mono-dispersed particles of 1µm diameter and mono-dispersed particles of 10µm diameter. It was found that the life of a filter is elongated by increasing the number of pleats, but the relationship is not linear. Increasing the pleat count from 2 to 4, for instance, improved the service life of the filter by a factor greater than 2 when loaded with the poly-dispersed particles, and a factor smaller than 2 when loaded with the mono-dispersed particles of 1 or 10 µm diameter. It was also found that the life of the filter is shorter when it is loaded with the poly-dispersed particles in comparison to when it is loaded with the above mono-dispersed aerosol of 1 or 10 µm particles, under the same mass flow rate. This peculiar behavior can be explained in terms of the diameter of the particles in the cake and the rate by which the filter collects the particles (i.e., filter's collection efficiency).

Chapter 4

Filtration Performance of Dust-Loaded Trilobal Fibers[6]

4.1. Introduction

In the half-century long history of modern aerosol filtration theory, the interactions between the aerosol flows with a clean single fiber with a circular cross-section has been the basis for developing correlations to estimate the collection efficiency of a filter (Kuwabara 1959, Stechkina and Fuchs, 1965; Brown 1993; Spurny 1998; Hinds, 1999; Tien, 2012). During a filter's service, particles deposit on the fibers and change the morphology of the filter's structure. As a result, the flow experiences higher resistance and the deposited particles enhance the collection mechanisms. The effect of particle deposition on the filtration performance (i.e., collection efficiency and pressure drop) of fibers with circular cross-section has been investigated previously in a many studies (e.g., Filippova and Hanel, 1997; Hinds and Kadrichu, 1997; Kanaoka et al., 2001; Przekop et al., 2003; Lantermann and Haenel, 2007; Li and Marshall, 2007; Kasper et al., 2009; Dunnett and Clement, 2009 and 2012; Hosseini and

---

[6] The contents of this chapter appears in the following publication:
A.M. Saleh, H.V. Tafreshi, On The Filtration Performance of Dust-Loaded Trilobal Fibers, 2015. Separation and Purification Technology, 149, 295–307

Tafreshi, 2012). Although trilobal fibers are becoming increasingly more available (Jung *et al.*, 2010; Geisler *et al.*, 2008; Karaca and Ozcelik 2007; Omeroglu *et al.*, 2010; Tascan and Vaughn, 2008), the literature is very scarce (and controversial sometimes), when it comes to using such fibers for aerosol filtration (Lamb and Gostanza, 1975, 1980a and 1980b; Sanchez et al., 2007, 2010). In fact, there are too many unanswered questions with regards to the actual advantage of such fibers over fibers with circular cross-sections. In this Chapter, we specifically aim to shed some light on the differences between the performance of fibers with trilobal and circular cross-sections. This chapter is an extension for the previous study reported in (Fotovati *et al.*, 2011), which was focused on performance of clean trilobal fibers, by taking the dust-deposition on the fibers into consideration.

In the remainder of this chapter, we first present the governing equations considered in this study to simulate the flow of air and airborne particle over a single fiber. In Section 4.3, we discuss our microscale and macroscale simulations strategies as well as fiber geometries and other numerical parameters considered in our study. In Section 4.4, we present our results and discussion where we compare the performance of trilobal fibers under dust loading conditions with their circular counterparts. In this section, we also study the effects of fibers' through-plane orientation on their filtration performance. The main conclusions drawn from this chapter are given in Section 4.5.

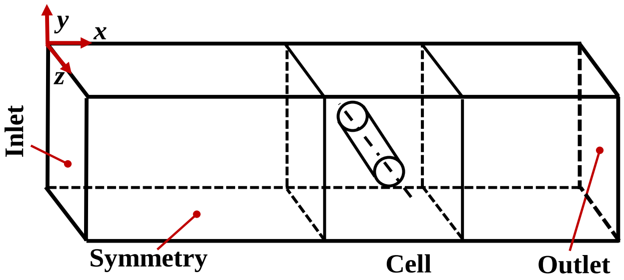

Figure 4.1: Simulation domain and boundary conditions used in the study.

4.2. Governing Equations

The equation governing the flow of air around a single fiber is the Stokes Equation which will be solved using ANSYS–Fluent code with appropriate boundary conditions as shown in Figure 4.1.

$$\frac{\partial u_i}{\partial x_i} = 0 \tag{4.1}$$

$$\frac{\partial p}{\partial x_j} = \mu\left(\frac{\partial^2 u_j}{\partial x_i \partial x_i}\right) \tag{4.2}$$

The air enters the simulation domain from a velocity inlet boundary, far upstream from the fiber, and exits the domain from a pressure outlet boundary. The inlet was placed far upstream the fiber so that the flow can adapt before reaching the fiber, and the outlet boundary condition was chosen so that no reversed flow takes place which may affect the accuracy of the calculation. A no-slip boundary condition is considered for the flow at the fiber surface. The particles are tracked via a Lagrangian approach in which the forces acting on the particle are integrated in order to update the particle position and velocity with time.

$$\frac{du_i^p}{dt} = \frac{18\mu}{d_p^2 \rho_p c^c}\left(u_i - u_i^p\right) + n_i \tag{4.3}$$

The first term in the right hand side of the above equation is the drag force and the second is the Brownian force term (Li and Ahmadi, 1992):

$$n_i = G_i \sqrt{\frac{\pi S_0}{\Delta t}} \tag{4.4}$$

where $S_0 = \frac{216\mu\sigma T}{\pi^2 \rho_p^2 d_p^5 S^2 c^c}$ is the spectral intensity of the fluctuations, $\sigma = 1.38\times10^{-23}(m^2kgs^{-2}K^{-1})$ is the Boltzmann constant and G_i is a zero-mean variant from a Gaussian probability function obtained by using two randomly chosen numbers λ_1 and λ_2 from a uniform distribution function (Box and Miller, 1958):

$$G_i = \sqrt{2\ln\lambda_1}\cos(2\pi\lambda_2) \tag{4.5}$$

The Brownian forces were only considered for particles with a diameter of 0.75 μm or smaller. The Brownian forces were incorporated in our particle tracking via a user-defined function for the Fluent code (Longest and Jinxiang, 2007; Hosseini and Tafreshi, 2010a, 2010b). In both models, the surface of the fiber is treated like a wall boundary condition. If the center of a particle reaches a distance from the fiber equal or less than the particle diameter, it is treated as a deposited particle (i.e., intercepted). Therefore, a user-defined function has been used to constantly monitor the distance between the airborne particles and the surface of the fiber or any previously deposited particle (Hosseini and Tafreshi, 2010b).

4.3. Simulation Strategies and Parameters

As the relative size of the particles and fibers with respect to one another can vary by orders of magnitudes, it is not always feasible (or computationally economical) to simulate such systems on a fixed scale for the entire range of variable. In this concern, we have considered two different modeling strategies for simulating particle loading on a fiber. These modeling strategies are referred to as microscale and macroscale models. The former is utilized when the particles are generally comparable to fibers in diameter (e.g., a particle-to-fiber diameter ratio of greater than 0.1, corresponding to a particle diameter greater than 1 μm in this study), whereas the latter is employed when the particles are much smaller than the fibers (e.g., a particle-to-fiber diameter ratio of smaller than 0.1, corresponding to a particle diameter less than 1 μm here). For the microscale simulations, the computational domain has to be meshed on scales smaller than the particle diameter and as a result, each deposited particle will be represented by a number of computational cells (Saleh *et al.*, 2013). Therefore, the computational cost of conducting microscale simulations rapidly increases for particles with small diameters relative to the fibers. Our macroscale modeling strategy, on the other hand, is designed for simulations in which resolving the actual shape of the particles in a dendrite has no real significance, and therefore the dendrite can be simulated with a coarser resolution as discussed in our previous work (Fotovati *et al.*, 2011, 2012; Saleh *et al.*, 2014a). In the macroscale model, each computational cell in the dendrite can accommodate more than one particle. The dendrite in this approach is modeled as a macroscopic porous medium comprised of randomly packed particles. The macroscale simulations, therefore, do not require excessively refined cells. In addition, to accelerate the formation of dendrites on a fiber in the macroscale models, the particles can be injected in clusters rather than individually (see Fotovati *et al.*, 2012 and Saleh *et al.*, 2014a for more detailed information).

In our macroscale approach, permeability of the dust-cake (i.e., cells containing particles) is predicted using the Kozeny–Carman equation (Carman, 1956).

$$k_g = \frac{d_p^2 c^c}{180}\frac{(1-\alpha)^3}{\alpha^2} \tag{4.6}$$

where α is the cell solid volume fraction, d_p is the particle diameter, and c^c is the Cunningham slip correction factor. The maximum solid volume fraction (SVF) that a computational cell can attain in the macroscale model is predicted using Equation 3.8, which is empirical correlation presented in the previous chapter. If the SVF of a cell reaches $\alpha_{\max}$, the cell is considered to be filled and is made impermeable to the particles. The unfilled cells, on the other hand, are treated as individual filters, and the amount of particle deposited in each of them is calculated using the cell model equations given in Appendix B.

To investigate how a trilobal geometry can influence the filtration performance of a fiber under dust-loading, we consider a trilobal fiber comprised of three overlapping ellipses (united in their focal points) similar to the work of Fotovati *et al.*, 2011. Our objective in this Chapter is to compare the performance of a trilobal fiber with its circular counterparts under different levels of dust-load (i.e., time in service). The counterpart circular fibers considered for this comparison are a fiber with an Area-Based Circular (ABC) diameter (the circular fiber with a cross-sectional area equal to that of the trilobal fiber) and a fiber with a Circumscribed Circular (CC) diameter (the circular fiber with a diameter equal to the circumscribed circle to the trilobal fiber) as shown in Figure 4.2a. This objective is motivated by the lack of a clear understanding of the advantages of using grooved fibers (e.g., trilobal fibers) over their circular counterparts. This question was addressed when the fibers are clean in Fotovati *et al.*, 2011; It was concluded that clean trilobal (or multi-lobal) fibers have no significant advantage over their circular counterparts. In this chapter, we discuss this question for when the fibers are loaded with aerosol particles (fiber's dust-hold capacity). For this study, we have arbitrarily chosen a major diameter of d_{maj} = 8 µm and a minor diameter of $d_{\min}$ = 4 µm for the ellipses constituting our trilobal fibers. Figure 4.2a also shows the ABC (9.5 µm) and CC (15 µm) diameters of the trilobal fiber for comparison. Note that in comparing a trilobal fiber with its circular circumscribed counterpart, we considered two different cases. In the first case, we simply replaced the trilobal fiber with the circumscribed fiber allowing the filter's SVF to increase from 10% to 19.6% (i.e., keeping the cell dimensions constant). In the second case, we increased the cell dimensions in order to maintain the same

SVF of 10% for the filter. Two extreme conditions are considered for the cross-sectional orientation of the trilobal fibers with respect to the direction of the incoming aerosols. The first case is when one of the grooves with its imaginary entrance plane normal to the flow direction is upstream of the fiber (facing the flow), and the second case is when this groove is downstream of the fiber (back to the flow) as shown with red dashed lines in Figure 4.2b. The former and the latter are referred to here as Normal Grooves Upstream Trilobal (NGUT) fiber and Normal Grooves Downstream Trilobal (NGDT) fibers, respectively.

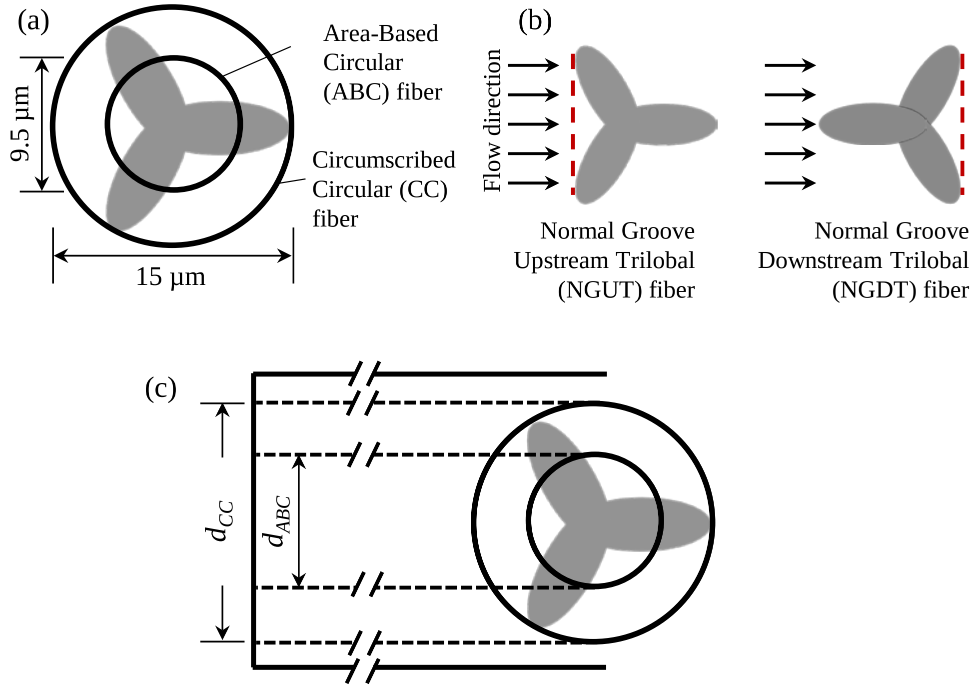

Figure 4.2: The trilobal fiber considered in the study and its circular counterparts is shown in (a). The two extreme orientations of a trilobal fiber with respect to flow direction: Normal Groove Upstream Trilobal (NGUT) fiber and Normal Groove Downstream Trilobal (NGDT) fiber in (b). The SFE definitions considered in the study for non-circular fibers are graphically shown in (c). Dashed and solid lines represent the circular diameters and the symmetric boundary conditions, respectively.

The SFE was originally developed for fibers with circular cross-sections and was defined as the ratio of the number of particles collected by a fiber to the number of particles that passed through an imaginary projected area of the fiber. No distinctive definition has yet been proposed for the SFE of fibers with non-circular cross-sections, due in part to the lack of axial symmetry of such geometries making the orientation of the cross-section with respect to the flow an additional parameter to be included in the analysis. In this chapter, we define the SFE of a trilobal fiber as the ratio of number of particles deposited on the fiber to the number of particles that passed through an imaginary projected area of its corresponding ABC fiber as shown in Figure 4.2c. Note that SFE may exceed unity indicating the capability of a single fiber to collect a number of particles greater than that of injected particles from its corresponding defined projected area. This is in agreement with the previous work in the literature (Hosseini and Tafreshi, 2012; Raynor, 2008; Regan and Raynor, 2009). For the CC fibers, we use the above-mentioned conventional circular-fiber definition of the SFE.

Aerosol particles with diameters of 0.125, 0.25, 0.75 and 2 µm are considered in our study. For particles with a diameter greater than 1 µm, we considered a microscale model, and for those smaller than 1 µm in diameter we used our macroscale approach. As mentioned earlier in Section 4.2, injecting the particles in the form of clusters allows one to significantly speed up the formation of a dust-cake on a fiber. However, this is at the cost of losing the morphology of the dendrites. As described elsewhere in the previous chapter, the outcomes of our macroscale model depends on the choice of the so-called *cluster-to-cell volume ratio* (CCVR) considered for the aerosol particles. Simulations conducted with a large CCVR are faster but less accurate. Decreasing the CCVR slows down the simulations but results in dendrites with more realistic morphologies. To select a suitable CCVR, we monitored the effects of varying the CCVR on the pressure drop values obtained for a NGUT fiber loaded with 0.5 µm particles. For the mesh volume of 1 µm^3 considered in this approach, we used a cluster volume of 0.06 µm^3 (i.e., CCVR=0.06) as the pressure drop values seemed to converge for CCVR values smaller than 0.06

(see Figure 4.3a). As shown in the figure, using CCVR greater to 0.06 causes the pressure drop to deviate from those values obtained with 0.06 or less CCVR.

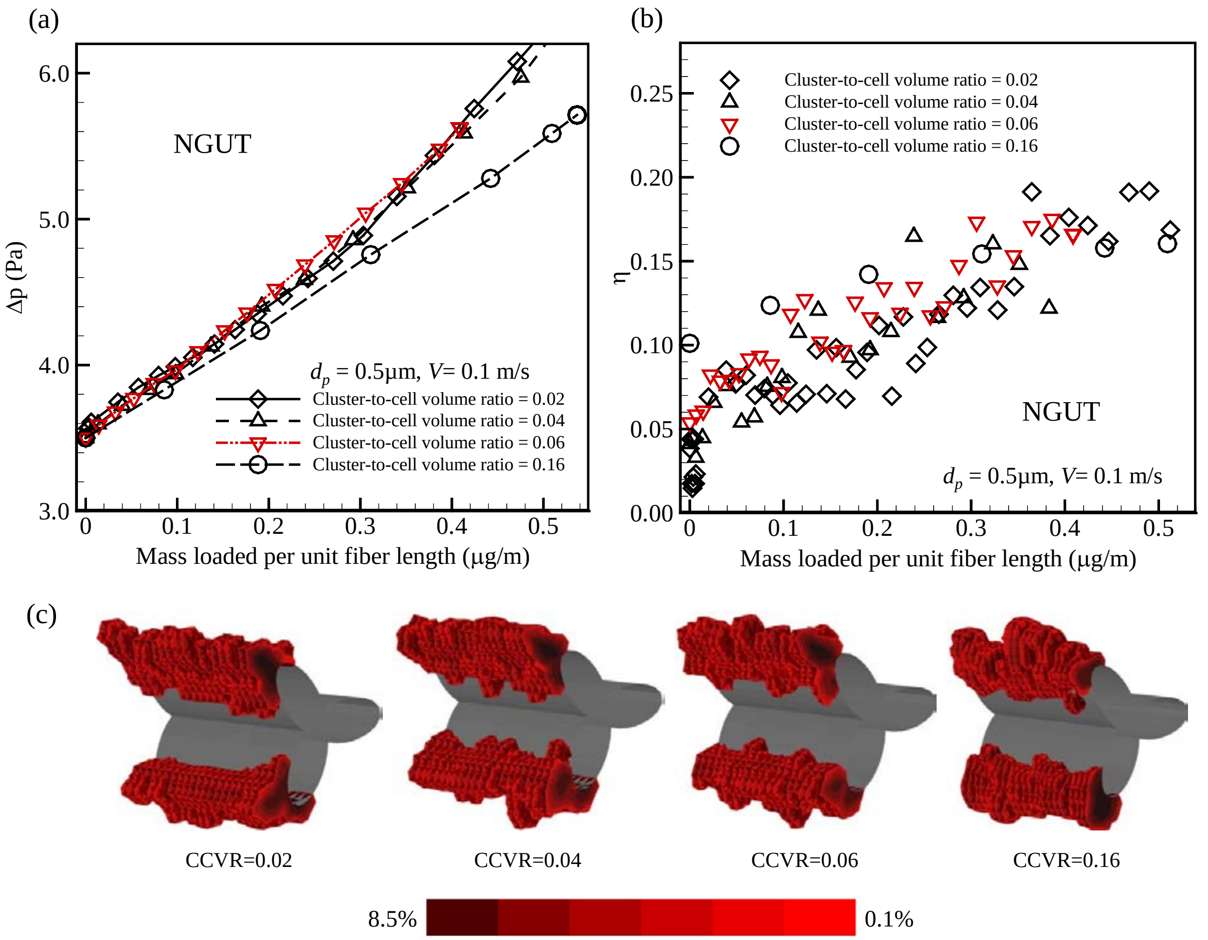

Figure 4.3: Effects of cluster-to-cell volume ratios (CCVR) on the pressure drop (a) and SFE (b) for a NGUT fiber loaded with particles with a diameter of 0.5 μm at a velocity of 0.1 m/s. Dust deposition profiles for the different CCVRs at a pressure drop of 5.7 Pa are shown in (c).

Figure 4.3b shows the effects of CCVR on SFE with loading. Although the SFE convergence is not as perfect as that of pressure drop, we believe that the error associated with this is insignificant from the perspective of the goals of this study as will be discussed later in this Chapter. The scatter in the SFE values shown in Figure 4.3b is due to the random injection. We inject the particles from random points near the inlet surface inside the domain to ensure the formation of a realistic dust deposition. Figure 4.3c shows dust deposition on a NGUT fiber obtained using different CCVRs at a pressure drop value of 5.7 Pa. It can be seen that the location of the dust cake on the surface of the fiber is not affected by the choice of CCVR, and except for the case of CCVR=0.16, all other dust deposition patterns are comparable to one another. It is important to mention that particles tracked here have a density of 1000 kg/m^3. The domain was meshed with about 22 grid points around the trilobal fiber. The flow was recalculated after injecting 200 clusters and calculated till the residuals reach a value of 1×10^{-10}.

Additionally, we compared our microscale model SFE values of a circular fiber with the experimental work of Kasper *et al.* 2009. It is important to mention that in their experimental work, the authors report the SFE values with mass loading per unit fiber length in addition to the adhesion probability of the particles to stick to the bare stainless fibers. The adhesion efficiency for the fiber considered is defined as a function of Stokes number (Kasper *et al.* 2009):

$$h_{adh} = \frac{Stk^{-3}}{Stk^{-3} + 0.0365\, Re_f^{2.46} + 1.91} \tag{4.7}$$

In order to compare our model results with the experimental work reported in Kasper *et al.* 2009, we included the probability of a particle intercepting with the fiber to adhere (and not to rebound) in our model using Equation 4.7 presented in their paper. The fiber considered here has a diameter of 30 µm loaded with 2.6 µm polystyrene particles with a corresponding Stokes number of 3. The fiber is placed in a cell with an SVF of 0.4%. Figure 4.4 shows the comparison of the SFE of the circular fiber as a function of mass loaded per unit length predicted by our microscale simulation model and the experiment presented in Kasper *et al.* 2009. The microscale simulations were repeated three times to avoid any statistical error resulting from the random injection and the adhesion probability processes. It is important to note that our simulation model does not take into account particles break off which might occur in the experiment with such high-inertia particles. This is the reason why our predictions slightly over predicts the SFE when compared with the experimental results.

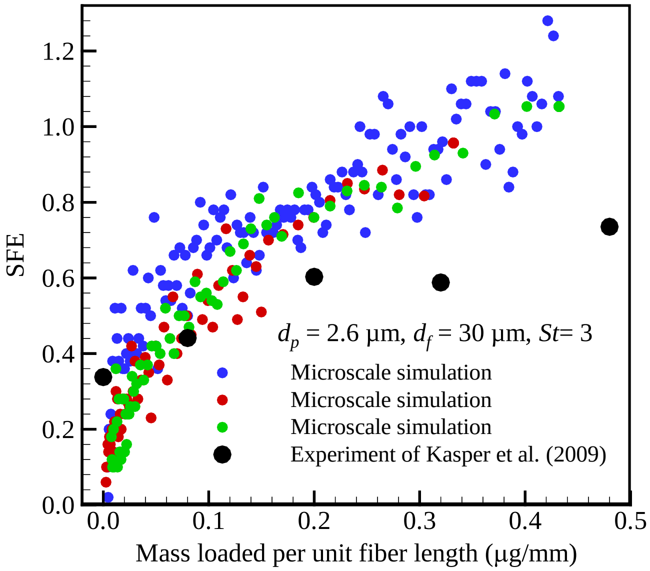

Figure 4.4: A comparison between the experimental data of Kasper et al. (2009) and our microscale simulation model. Fiber considered here has a diameter of 30 µm loaded with 2.6 µm polystyrene particles with a Stokes number of 3. Black symbols represent the experimental SFE values while blue, red and green represents three different repetitions of our microscale simulations considering particle to fiber rebound.

4.4. Results and Discussion

In this section, we present the results of our simulations conducted to study the performance of trilobal fibers of different cross-sectional orientations and their corresponding ABC and CC fibers under dust loading (Section 4.4.1). We will also study the effects of fibers through-plane orientation on the filtration performance of the above fibers under dust loading condition (Section 4.4.2).

4.4.1 Trilobal Fibers vs. Circular Fibers

In this section, we report the instantaneous performance (pressure drop and SFE) of a trilobal fiber when loaded with particles of different diameters at different velocities and compare the results with those obtained for the fiber's circular counterparts.

To better illustrate how the cake morphology on a fiber varies with the size and velocity of the depositing particles, contour plots of cells' SVF are shown in Figure 4.5 for two particle diameters of 0.25 µm and 0.5 µm and two flow velocities of 0.5 m/s and 5 m/s. The figures show the dust deposit for each case at a pressure ratio of $\Delta p / \Delta p_0 \cong 2$. It can be seen that particles with higher inertia tend to deposit on the front side of the fibers whereas the smaller particles mostly deposit on the fiber's lateral sides. Particle deposited on a fiber's lateral sides can significantly increase the fiber's projected frontal area and consequently increase the fiber's pressure drop. Note that the maximum packing fraction $\alpha_{\max}$ is smaller for smaller particles. This means that for a given mass of deposit, dendrites made of small particles occupy larger volumes of the void space between the fibers. It is interesting to note that the subfigures in Figure 4.5 show a smaller dust cake for the case of d_p=0.25 µm than the case of d_p=0.5 µm (see for instance the Figures in 4.5a, 4.5b, and 4.5c). This is because smaller particles cause more pressure drop, and therefore less number of particles (in volume) was needed to raise the initial pressure drop of the fiber by a factor of 2. Of particular interest here is the difference between performance of NGUT and NGDT fibers. It can be seen that having the normal groove facing the flow can be useful if the particles have sufficient inertia to penetrate deep into the stagnant air inside the groove. Among the particle diameters and flow velocities shown in Figure 4.5, this happened only for $d_p = 0.5 \mu m$ and $V = 5 m/s$ (see Figure 4.5a–4.5f). In other words, the trilobal fibers showed no advantage over their circular counterparts when the particles are not highly inertial. The dust deposits shown in Figures 4.5c, 4.5f, 4.5i, 4.5l, and 4.5o indicate that it is in fact easier for the low-inertia particles to deposit on the front face of a fiber if the fiber is circular rather than trilobal (these particles tend to deposit on the lateral sides of trilobal fibers leaving the grooves between the lobes clean).

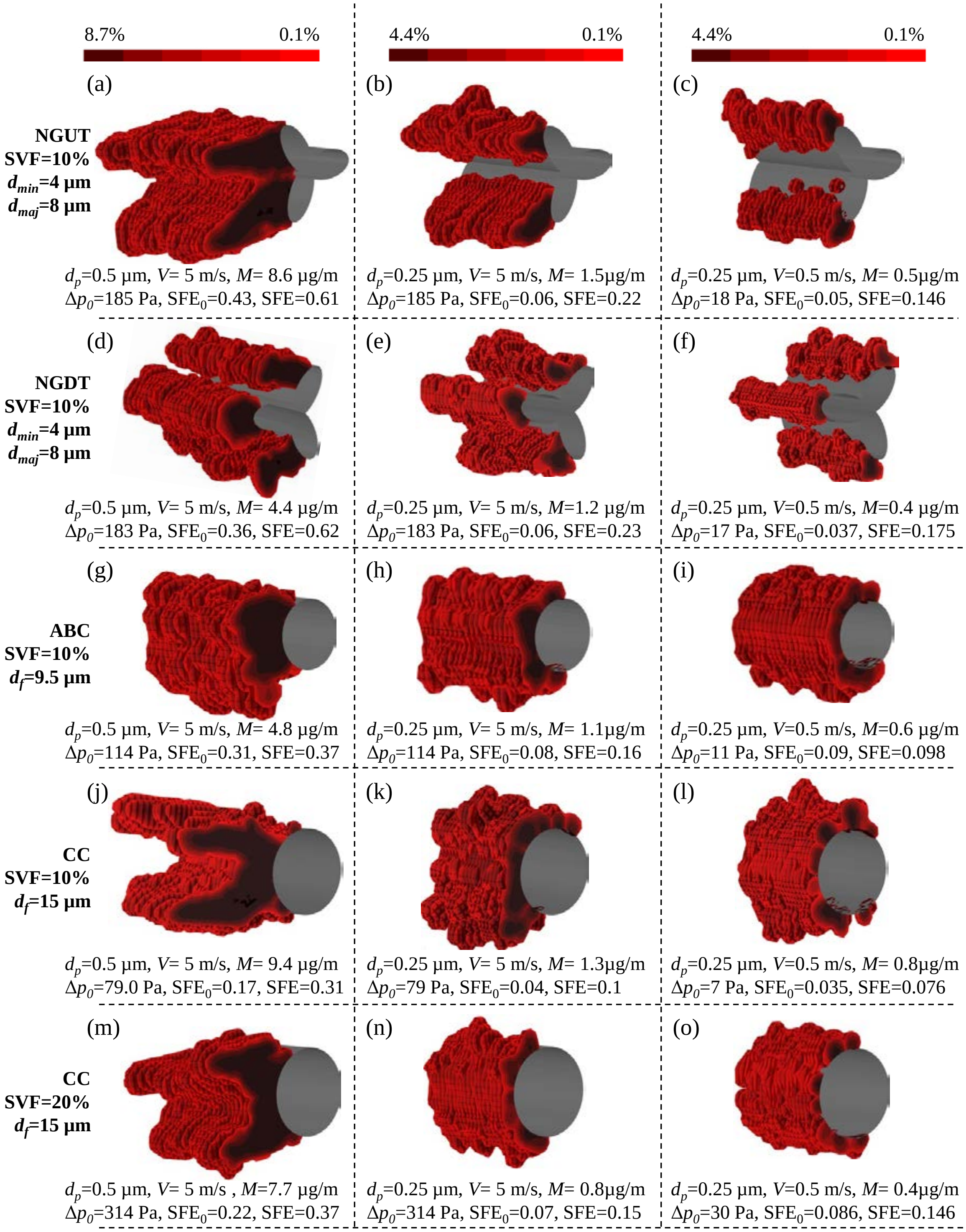

Figure 4.5: Dust deposition profiles at a pressure of $\Delta p / \Delta p_0 \cong 2$ for the different fibers when loaded with particles with diameters of 0.5 and 0.25 µm at velocities of 0.5 and 5 m/s.

More quantitative comparison between the rate of increase of pressure drop and collection efficiency of these fibers is given in Figures 4.6a–4.6f as a function of the mass of particles loaded on the fiber per unit length M . The initial values of the pressure drop at different air inlet velocities for the five cases considered in this figure are presented in Table 4.1. In generating these data, the fibers were loaded with particles until their pressure drop reached a value about two times greater than their clean pressure drop. Although the trilobal fibers and their ABC and CC counterparts have the same cross-sectional area (i.e., their unit cells have the same SVF), the trilobal fibers have higher initial pressure drop. This is because the trilobal fibers have larger surface areas. Moreover, the trilobal fibers have larger projected frontal area than their ABC counterparts. The results shown in Figures 4.6a–4.6c are selected from a larger group of data generated in this study. Figures 4.6a–4.6c show that regardless of the cross-sectional shape of the fiber, the rate of increase of pressure drop is higher when the particles are smaller, as expected. For instance, with a mass per unit length of 1 µg/m, the pressure drop ratio of the NGUT fiber reaches a value of about 1.6 if loaded with particles with a diameter of 0.25 µm at 5 m/s inlet velocity, and about 1.1 if loaded with particles of 0.5 µm diameter at the same velocity (see Figures 4.5a and 4.5b). The reason for this is twofold: 1) larger particles have smaller specific surface areas leading to less resistance against the flow, and 2) larger particles tend to deposit on the front side of the fiber (facing the flow) as opposed to the lateral sides of the fiber. Therefore, the rate of increase of a fiber's frontal projected area is slower when the fiber is loaded with large (inertial) particles.

Table 4.1: Initial (clean) pressure drop values for different fibers with a zero through-plane fiber orientation.

***V* (m/s)**	**0.5**	**1**	**5**
Δp_0 , NGUT, SVF=10% (Pa)	17.5	29.0	185.4
Δp_0 , NGDT, SVF=10% (Pa)	17.3	28.7	182.9
Δp_0 , ABC, SVF=10% (Pa)	10.9	17.5	114.4
Δp_0 , CC, SVF=10% (Pa)	7.2	14.4	79.0
Δp_0 , CC, SVF=20% (Pa)	30.0	51.6	314.3

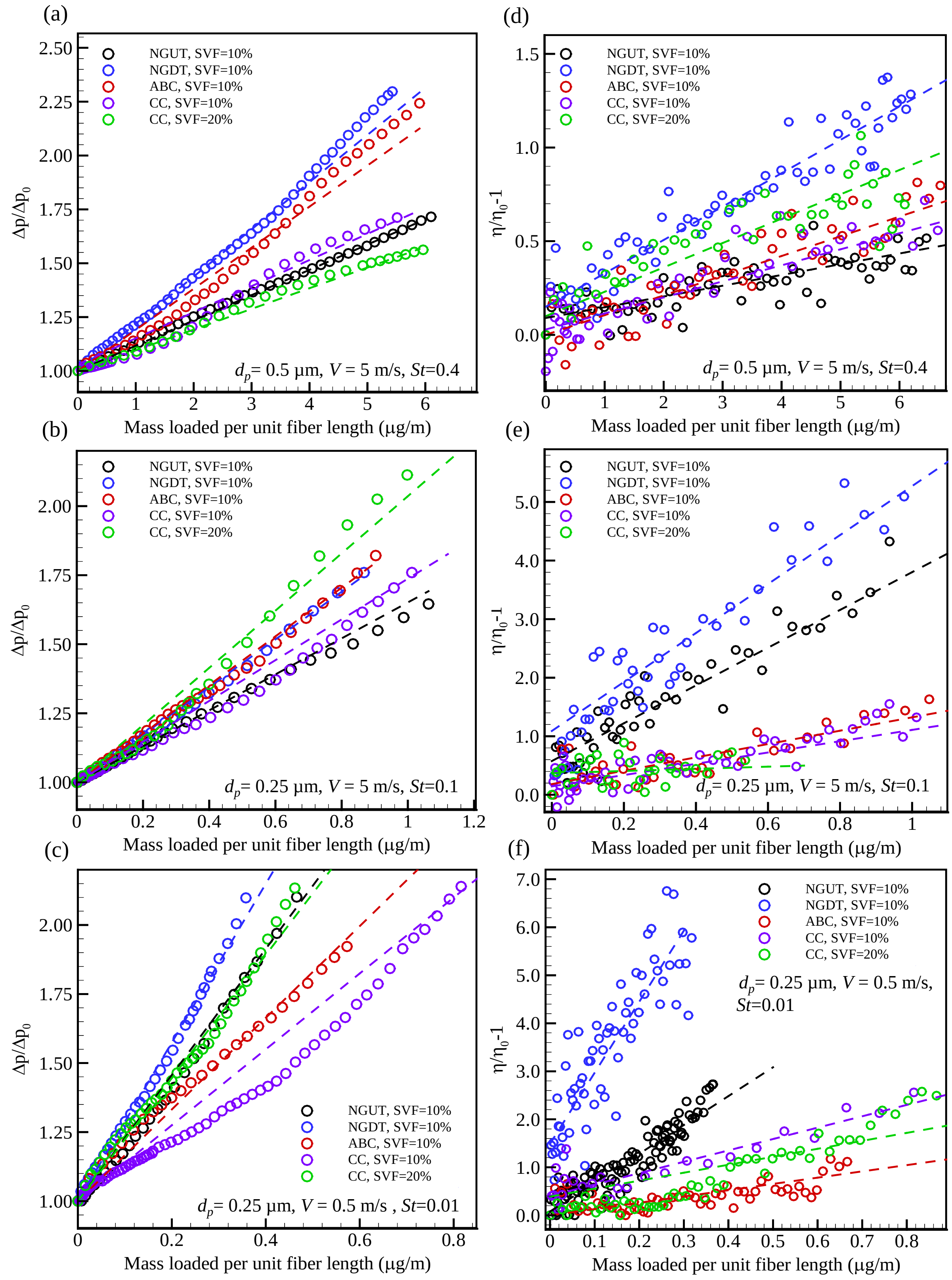

Figure 4.6: Pressure drop and SFE ratios for fibers of different cross-sectional shapes versus mass per unit fiber length loaded with particles of different diameters of 0.25 and 0.5 μm and at different velocities of 0.5 and 5 m/s are given in (a) through (f). Linear least square regression lines are given for each case.

Figures 4.6d–4.6f show the ratio of the instantaneous SFE η to that in the absence of dust deposit η_0 for the same fibers. Negative values shown in the scatter points in these figures occur when the instantaneous SFE (η) is less than the initial value of SFE (η_0), this is due to the random injection of the particles.

Similar to the case of pressure drop, the rate by which the SFE increases depends strongly on the particle deposition pattern. In the case of high-inertia particles (e.g., Figure 4.6d), the cake formation takes place mostly on the upstream face of the fibers as shown in the dust profiles (see Figures 4.5a, 4.5d, 4.5g, 4.5j, and 4.5m), whereas for the low-inertia particles (e.g., Figure 4.6f) the cake tends to grow laterally leading to a faster rate of increase in the fiber's collection efficiency (see Figures 4.5c, 4.5f, 4.5i, 4.5l and 4.5o).

The trend of the data shown in Figure 4.6a–4.6c implies that the pressure ratio varies almost linearly with the mass of particles deposited on the fibers,

$$\frac{\Delta p}{\Delta p_0} = \varphi M \tag{8}$$

where φ is the slope of the line obtained by curve fitting, and M is the mass per fiber length in µg/m. This equation is curve fitted into our data and also shown in Figure 4.6a–4.6c. The coefficient φ is plotted versus the product of Stokes number $St = \frac{\rho_p d_p^2 C^c V}{18\mu d_f}$ and particle-to-fiber diameter ratio $R = \frac{d_p}{d_f}$ for 0.125 $< d_p <$ 0.75 µm and 0.5 $< V <$ 5 m/s (see Figure 4.7). Here $d_f = d_{ABC}$ for the trilobal and ABC fibers, and $d_f = d_{CC}$ for the CC fibers. Note that d_{ABC} is the diameter of the ABC fiber.

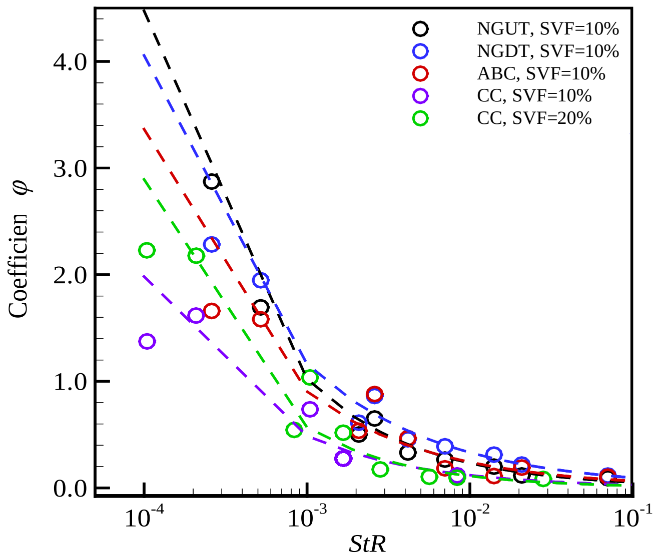

Figure 4.7: Coefficient φ representing the rate at which fiber pressure drop increases with loading is given for the fibers considered in the current study. Dashed-lines show the power-law curve fits.

Power-law curve fits are also generated for the relationship between the slope φ and $R\,St$ in the form of

$$\varphi = \gamma \left(R\,St\right)^{\chi} \tag{9}$$

where the values of γ and χ are shown in Table 4.2.

Similarly, the data given in Figure 4.6d–4.6f in addition to other data not shown here for the sake of brevity are used to develop correlations that describe the behavior of the SFE with loading as a function of mass loaded M (µg/m) as shown in the following form:

$$\frac{\eta}{\eta_0} - 1 = \xi + \psi M \tag{10}$$

where ξ and ψ are the curve fit parameters.

Table 4.2: Curve fit parameters for the pressure drop ratio correlation of Equation 9.

d_p (μm)	**0.25**	**0.25**	**0.50**
V (m/s)	**0.5**	**5.0**	**5.0**
ξ, NGUT, SVF=10%	0.08	0.58	0.09
ξ, NGDT, SVF=10%	1.49	1.09	0.15
ξ, ABC, SVF=10%	0.00	0.18	0.00
ξ, CC, SVF=10%	0.00	0.14	0.03
ξ, CC, SVF=20%	0.39	0.37	0.10
ψ, NGUT, SVF=10%	6.01	3.22	0.06
ψ, NGDT, SVF=10%	14.78	4.18	0.18
ψ, ABC, SVF=10%	1.31	1.14	0.11
ψ, CC, SVF=10%	1.68	0.96	0.09
ψ, CC, SVF=20%	1.66	0.18	0.13

The coefficients ξ and ψ are presented in Table 3 as a function of particle diameter for the different fiber cross-sections.

As mentioned earlier in this section, there are some requirements for a particle to be able to deposit inside a flow-facing groove: 1) the particle should be smaller than the groove; and 2) the particle should be highly inertial to penetrate into the stagnant layer of air inside the groove.

Table 4.3: Curve fit parameters for the SFE ratio correlation of Equation 10.

d_p (μm)	**0.25**	**0.25**	**0.50**
V (m/s)	**0.5**	**5.0**	**5.0**
ξ, NGUT, SVF=10%	0.08	0.58	0.09
ξ, NGDT, SVF=10%	1.49	1.09	0.15
ξ, ABC, SVF=10%	0.00	0.18	0.00
ξ, CC, SVF=10%	0.00	0.14	0.03
ξ, CC, SVF=20%	0.39	0.37	0.10
ψ, NGUT, SVF=10%	6.01	3.22	0.06
ψ, NGDT, SVF=10%	14.78	4.18	0.18
ψ, ABC, SVF=10%	1.31	1.14	0.11
ψ, CC, SVF=10%	1.68	0.96	0.09
ψ, CC, SVF=20%	1.66	0.18	0.13

To better quantify this, we present the inertial and interception components of the SFE for the ABC fiber in Table 4 using the conventional cell model equations for a circular fiber (see Appendix C). For the trilobal fibers, we used an ABC circular diameter in these equations for the lack of a better alternative. It was found that when the inertial impaction is the dominant deposition mechanism and interception is negligible, the NGUT fiber shows the slowest rate of increase of pressure drop and collection efficiency. On the other hand, when interception is the dominant mode of particle capture, the particles tend to deposit in the lateral sides of the fiber and cause rapid increase in the fiber’s pressure drop and collection efficiency. In contrast, the streamlined shape of the NGDT fiber seems to make the grooves inaccessible to the particles and promote the growth of the cake in the lateral directions even in the inertial impaction dominant regime causing them to experience the highest rate of increase in pressure drop and collection efficiency. For instance, consider the case of loading the trilobal and circular fibers with particles having a diameter of 0.5 µm at a velocity of 5 m/s (i.e., St=0.4). In this case, the NGUT fiber has one of the least increases in pressure drop ratios and collection efficiency (Figures 4.6a and 4.6d). Here, the ratio of SFE due to impaction to the total SFE is almost 1 whereas the same ratio for SFE due to interception is 0.02. This explains why the dust profiles shown in the left column of Figure 4.5 is mainly on the upstream side of the fiber rather than the lateral sides. When loading the above fibers with 0.25 µm particles at inlet velocity of 0.5 m/s which represents low-inertia particles of St= 0.01 (Figures 4.6c and 4.6f), both configurations of the trilobal fiber show undesirable rate of increase of pressure drop with loading. In this case is almost zero (negligible deposition due to inertial impaction) as can be seen in the dust profiles shown in the right column in Figure 4.5. This indicates that that the NGDT fibers, having a somewhat aerodynamic shape, can hardly accommodate any particles in any of their grooves at any loading condition.

Table 4.4: Ratios of impaction and interception SFEs to the total SFE for different particle diameters and flow velocities calculated based on the cell model equations for ABC fiber.

d_p (μm)	**0.125**	**0.25**			**0.5**			**0.75**		
***V* (m/s)**	5	0.5	1	5	0.5	1	5	0.5	1	5
η_I/η_Σ	0.02	0.00	0.01	0.77	0.06	0.40	1	0.32	.85	1
η_R/η_Σ	0.13	0.21	0.29	0.13	0.58	0.47	0.02	0.59	0.21	0.01

To compare the performance of the fibers with different cross sectional shape from a different perspective, we normalized the performance for the five different fibers considered here with the initial values of the ABC fiber in Figure 4.8. We only included the two extreme cases (the highest and the lowest inertial particles) among the three cases discussed in Figure 4.6.In the first case as shown in Figure 4.8a and 4.8b, we plotted the normalized pressure drop and the SFE of the different fibers when loaded with 0.5 μm at 5 m/s inlet velocity. It is clearly shown that the CC fiber with 20% SVF has the maximum pressure drop; in spite of that, it does not experience the maximum SFE. Instead, both trilobal fibers (NGUT and NGDT) experience the maximum SFEs. The pressure drop is lower of course in the case of NGUT for the same reasons discussed above and more importantly it experiences the slowest increase with loading. The ABC fiber in this case has average pressure drop and SFE, but its pressure drop increases faster with loading; which makes the NGUT performs better that circular ones as discussed before. Note that the CC fiber experience the least pressure drop and the SFE values compared to the rest of the fibers.

In the second case as shown in Figure 4.8c and 4.8d, we plotted the normalized pressure drop and SFE of the different fibers with the initial values of ABC fiber when loaded with 0.25 μm at 0.5 m/s inlet velocity. In this case with lowest inertia particles, both trilobal fibers experience almost the same pressure drop values initially and with loading. Their pressure drop values increase faster in this case than the circular fiber. The ABC fiber showed low pressure drop with slow increase with loading in addition to good SFE initially higher than the trilobal ones.

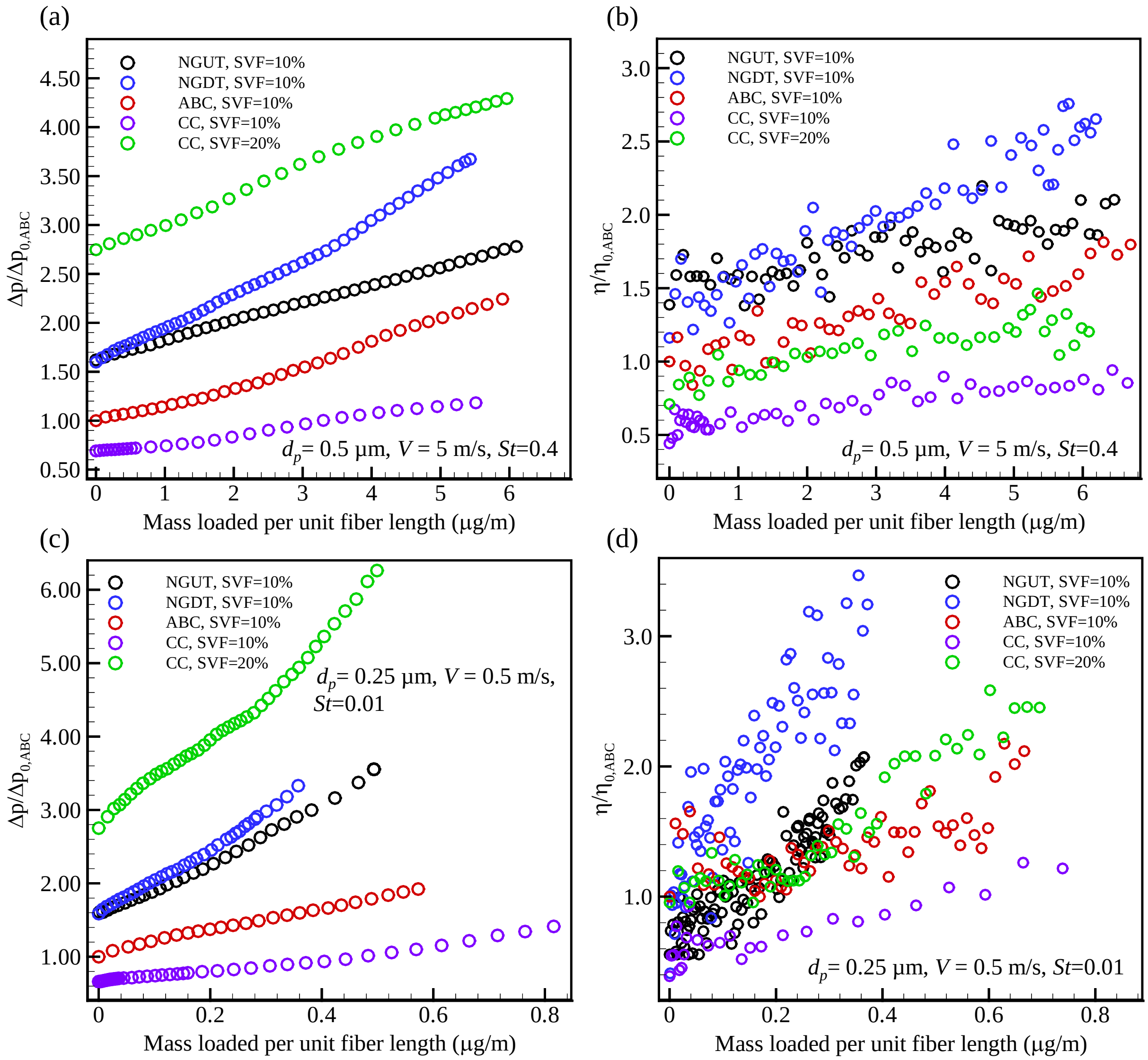

Figure 4.8: Pressure drop and SFE for fibers of different cross-sectional shapes versus mass per unit fiber length loaded with particles of different diameters of 0.25 and 0.5 µm and at different velocities of 0.5 and 5 m/s are given in (a) through (d). Pressure drop and SFE values here are normalized with the initial values of the ABC circular fiber.

To study the instantaneous performance of our trilobal fibers when challenged with larger particles we use the aforementioned microscale simulation method. Figure 4.9 shows our microscale simulation results obtained for a particle size of 2 µm at a velocity of 5 m/s (*St*= 6.3). Examples of our particle dendrites on the aforementioned fibers are shown in Figure 4.9a at a pressure ratio of $\Delta p / \Delta p_0 \cong 1.5$. It can be seen that particles tend to deposit inside of the normal groove in the NGUT fiber and the cake growth in the lateral directions is minimal.

Note that in our microscale dust-cake simulations, the particles are released in the simulation domain from random locations at the inlet. This allows us to produce particle dendrites with realistic morphologies. As such, the simulations should be repeated a few times to reduce the statistical uncertainty of the results. Therefore, the pressure drop and collection efficiency values reported here are the averaged values over three repetitions of the same particle-fiber combinations (see Figures 4.9b and 4.9c).

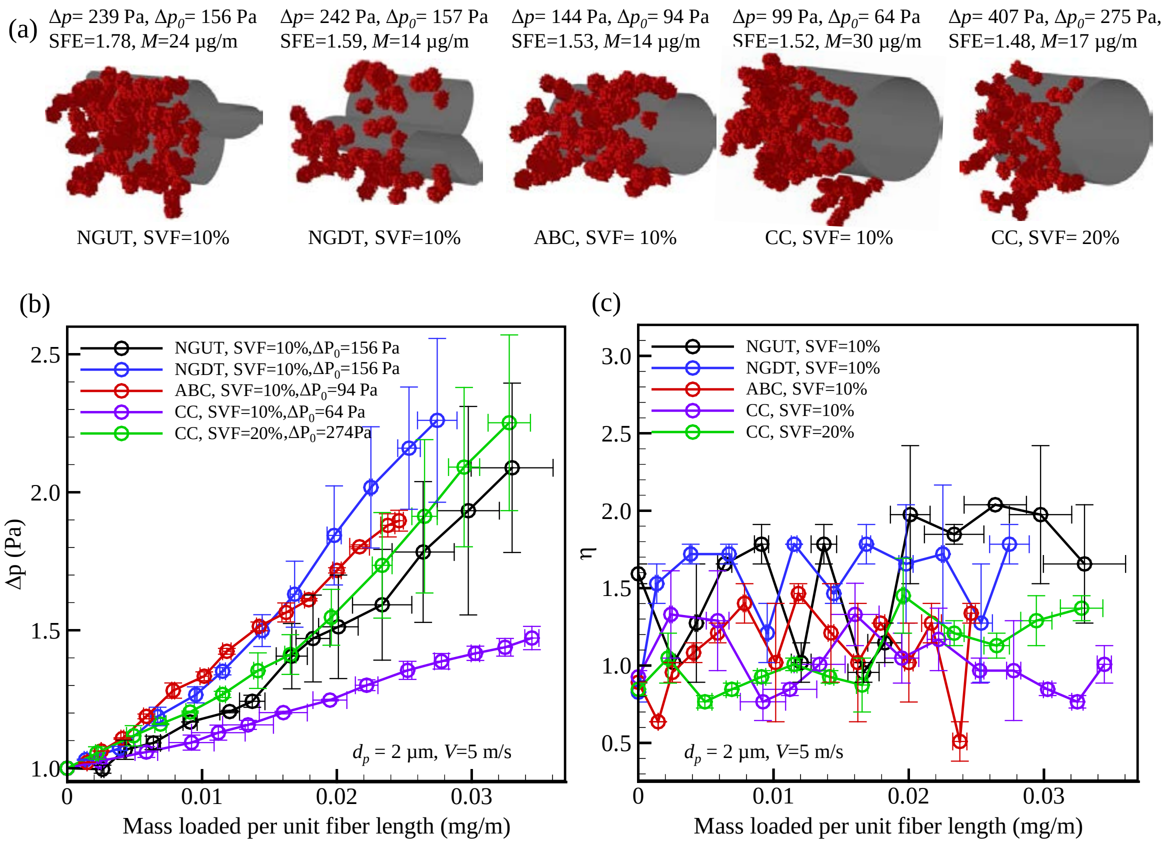

Figure 4.9: Microscale simulation results for the instantaneous pressure drop and SFE of the fibers discussed in the study when loaded with particles with a diameter of 2 μm at a velocity of 5 m/s. (a) Dust profiles at a pressure drop ratio of $\Delta p / \Delta p_0 \cong 1.5$; (b) instantaneous pressure drop ratio; and (c) instantaneous SFE.

As can be seen in Figure 4.9b, the NGUT fiber performs quite well relative to other fibers in terms of the rate of pressure drop increase with loading. This is due to the aforementioned ability of the inertial particles to deposit deep inside the normal groove in the NGUT fibers. In contrast, the NGDT configuration has resulted in the highest rate of pressure drop increase as the particles tend to deposit on the tips of the lobes and grow in the lateral directions. Figure 4.9c shows the SFE of these fibers as functions of deposited mass. Despite the inherent statistical noise of the calculations, one can note that the NGUT and NGDT fibers have higher overall SFE values. Note also the rate of increase of SFE is quite slow in the case shown here as particles are highly inertial ($St = 6$).

4.4.2 Effects of Fiber's Through-Plane Orientation on Dust-Loaded Performance

We previously studied the effects of fibers' through-plane orientations on the pressure drop and collection efficiency of a clean filter (Fotovati *et al.*, 2011CES). It was shown that pressure drop and collection efficiency of a clean filter decrease with increasing the through-plane orientation of the fibers. In this section, we study the effects of fiber's through-plane orientation on a filter's dust-loaded performance. More specifically, we conduct a series of macroscale simulations to investigate if the grooves on a trilobal fiber may actually become more effective when the axis of the fiber is not necessarily perpendicular to the flow direction. We considered three particle diameters of 0.25, 0.5, and 0.75 µm and two air flow directions of 22.5° and 45° with respect to the *x*-axis. For these simulations, we used periodic boundary conditions for the side boundaries in contact with the fiber as shown in Figure 4.10a. This allows one to consider inlet angles for the incoming air flow. The top and bottom boundaries were kept symmetric.

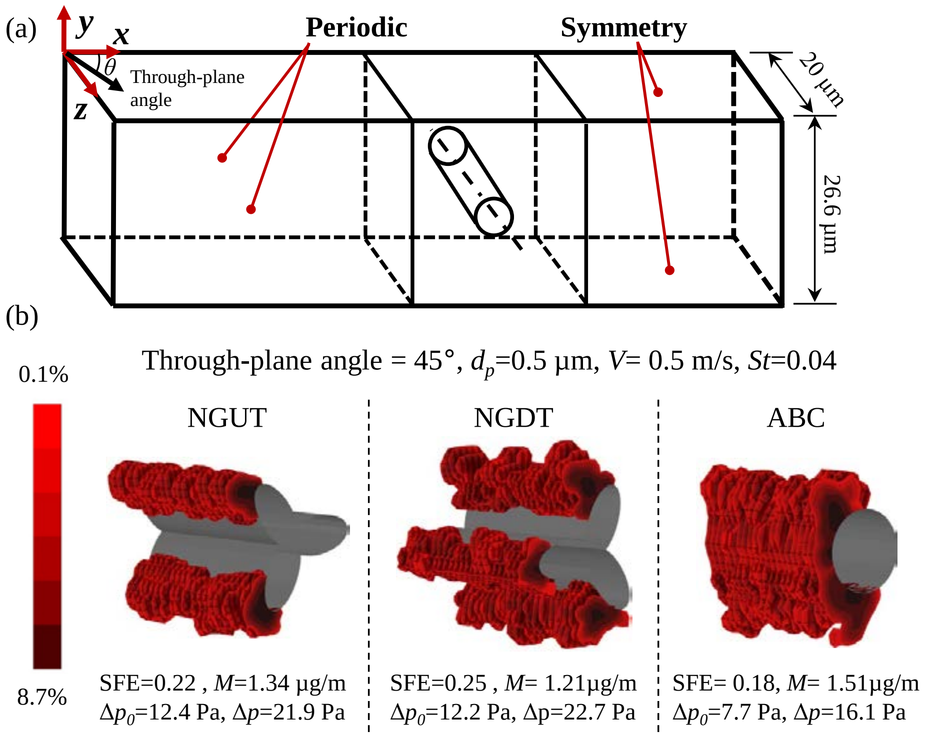

Figure 4.10: Simulation domain and boundary conditions used for fibers with a non-zero through-plane orientation (a), and dust deposition profiles on NGUT, NGDT and ABC fibers at a pressure drop ratio of $\Delta p / \Delta p_0 \cong 2$ and a flow velocity of 0.5 m/s consisting of particles with a diameter of 0.5 µm (b).

Figure 4.10b compares the dust deposit on a trilobal fiber in the NGU and NGD configurations with its ABC counterpart at a pressure ratio of $\Delta p / \Delta p_0 \cong 2$ for a fiber through-plane orientation of 45 degrees loaded with particles with a diameter of 0.5 µm and a velocity of V= 0.5 (St =0.04). Obviously, this is not an impaction-dominant deposition mechanism (η_I / η_Σ = 0.06 and η_R / η_Σ =0.58), and that is why the particles have not been able to deposit inside the grooves of the trilobal fiber. More importantly, these results show no evidence of an improved performance for the trilobal fiber relative to its ABC counterpart when the fibers have a through-plane orientation of 45 degrees. More quantitative comparison between the pressure drops of these fibers is given in Figure 4.11a through 4.11d for particle diameters of 0.5 and 0.25µm, flow velocities of 0.5 and 5m/s, and fiber through-plane orientations of $\theta = 0$ and 45 degrees as a function of mass loaded per unit fiber length.

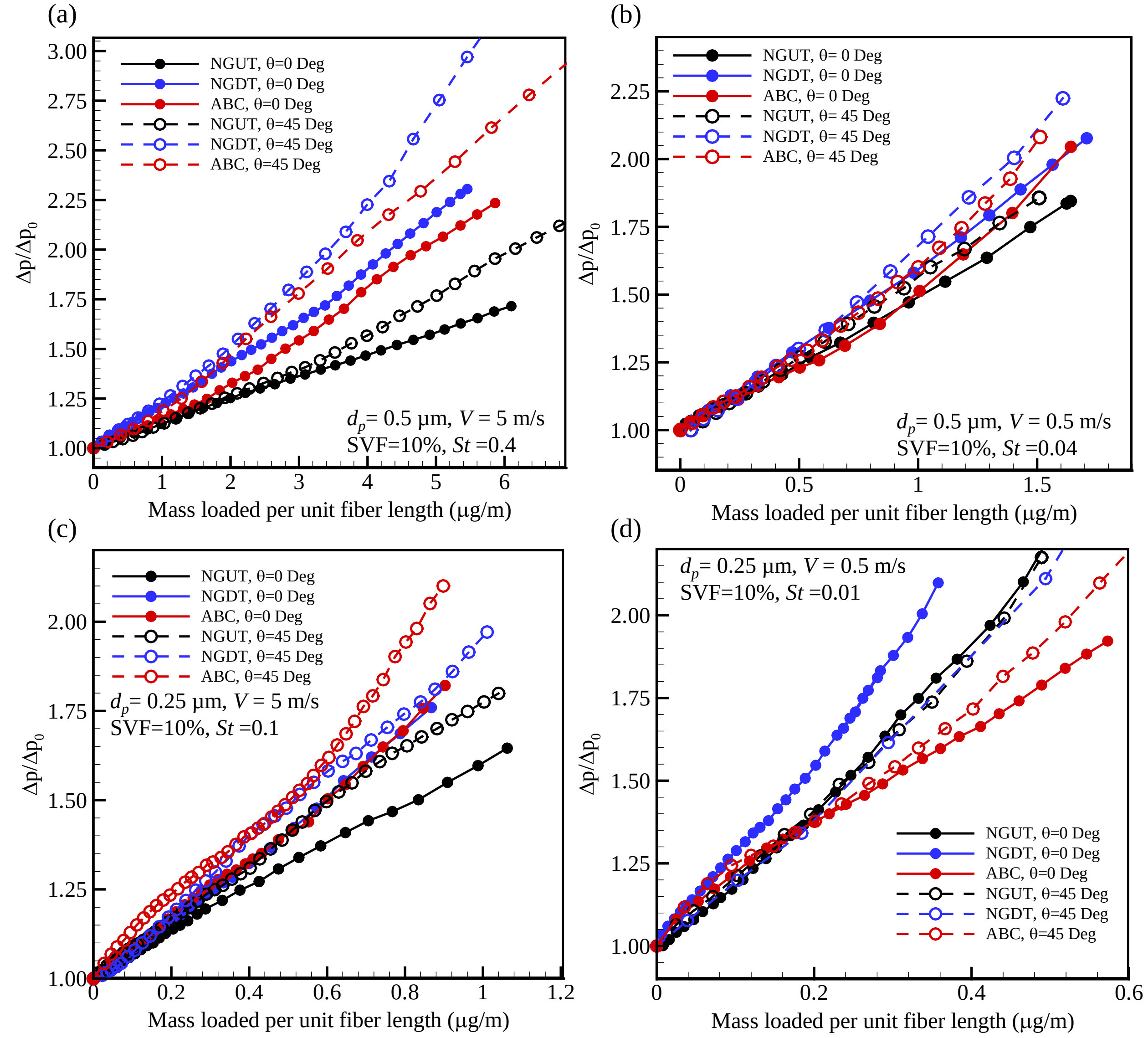

Figure 4.11: Instantaneous pressure drop as a function of mass loaded per unit fiber length for the NGUT fiber, NGDT fiber, and the ABC fiber with through-plane orientations of 0 and 45 degrees are shown in (a) through (d) for particle diameters of 0.25 and 0.5 µm and air velocities of 0.5 and 5 m/s.

In general, increasing the flow velocity reduces the rate of increase in pressure drop for all fiber cross-sections as more particles tend to deposit on the upstream face of the fibers. Therefore, more mass can deposit on the fibers before its pressure drop reaches twice the initial (clean fiber) value as shown in Figures 4.11a–4.11b and Figures 4.11c–4.11d for particles with a diameter of 0.5 and 0.25 µm, respectively. In agreement with the discussion given in the previous section, the NGUT fiber shows the best performance when the particles are highly inertial (*St*=0.4), as can be seen in Figure 4.11a for both 0 and 45° through-plane angles. As shown in Table 3, the corresponding SFE ratio η_I/η_Σ for this case is almost one, indicating that inertial impaction is the dominant deposition mechanism. Similarly, the NGUT fiber has the best performance for the case shown in Figure 4.11c for both through-plane orientations when loaded with particles with a diameter of 0.25 µm at an inlet velocity of 5 m/s (*St*=0.1). For this case, we have η_I/η_Σ = 0.77, again signifying that importance of inertial impaction in particle capture. In contrast, the NGUT fiber does not show a good performance relative to other cross-sections when the particles are not inertial, and the above-mentioned through-plane orientation made no contribution to improvement the problem. This is shown in Figures 4.11b and 4.11d, where the fibers are loaded at a flow velocity of 0.5 m/s with particles with diameters of 0.5 µm (*St*=0.04) and 0.25 µm (*St*=0.01), respectively. The ratio η_I/η_Σ is 0.06 and 0 for the results shown in Figures 4.11b and 4.11d, respectively, indicating that inertial impaction is insignificant in both cases. It is important to note that we normalized the pressure drop value of each fiber with its own initial pressure drop. Note that the initial pressure drop in the case of higher oriented fibers is less than that in fibers with no through plane orientation. This is the reason why in most of the cases shown in Figure 4.11 the pressure drop ratios of oriented fibers are higher than their normal counterparts as they are normalized with smaller number.

4.5. Chapter Conclusions

In this chapter, micro- and macroscale approaches were utilized to study and quantify the unsteady-state behavior of a fiber under particle loading. In particular, we compared the performance of trilobal fibers with their circular cross-sections when other parameters are kept constant to better understand the merits of using trilobal fibers in aerosol filtration. We used the

ANSYS–Fluent code as the platform for our simulations and enhanced its capabilities with a series of in-house User-Defined Functions. We conducted a parameter study (particle diameters between 0.125 µm to 2 µm) to produce correlations for the instantaneous pressure drop and collection efficiency of trilobal and circular fibers as a function of the mass deposited per unit length of the fiber. A trilobal geometry consisting of three overlapping elliptical lobes with major and minor diameters of 8 and 4 µm was considered here as representative example of trilobal fibers used in aerosol filtration applications. For the range of particle and fiber diameters considered, the trilobal fibers are found to perform superior to their circular counterparts only when the particles are highly inertial, and only if the trilobal cross-section is in the NGUT configuration. Therefore, one may summarize that the probability of an aerosol filter comprised of trilobal fibers performing better than its counterpart made of circular fiber is not very high, given the lack of control over the orientation of the grooves on a trilobal fiber in a fibrous filter with respect to the flow direction. We also studied the effects of the through-plane orientation of the trilobal fibers on their performance relative to that of their circular counterpart. While both the clean and dust-loaded pressure drop values are lower for trilobal or circular fibers with a non-zero through-plane orientation, a trilobal fiber can only perform better than its circular counterpart if placed in the NGUT position.

Chapter 5

Semi-Numerical Model for Pleated Air Filters[7]

5.1. Introduction

As discussed in Chapter 1, most air filters are made of pleated fibrous media. This is to accommodate as much filtration media as possible in a limited space available to an air filtration unit. A variety of parameters contribute to the performance of a pleated filter. These parameters include, but are not limited to, geometry of the pleat (e.g., pleat height, width, and count), microscale properties of the fibrous media (e.g., fiber diameters, fiber orientation, and solid volume fraction), aerodynamic and thermal conditions of the flow (e.g., flow velocity, temperature, and operating pressure), and particle properties (e.g., diameter, density, and shape). In addition, an important parameter that strongly affects the performance of a filter through its service life is the dust deposition pattern—a non-linear function of the above-mentioned parameters (Bourrous *et al*., 2014; Gervais *et al*., 2014; Fotovati *et al*., 2011, 2012; Saleh *et al*., 2014). Two filters with identical clean pressure drop and collection efficiency values, for instance, may exhibit very different performances as they collect particles over time. Despite its obvious importance, effects of dust loading on the performance of pleated filters have not been

---

[7] Contents of this chapter appear in the following publication:
A.M. Saleh, H.V. Tafreshi, Semi-Numerical Model for Predicting the Service Life of Pleated Filters, Sep. Purif. Technol. 137 (2014) 94–108

sufficiently studied in the literature, especially from a computational viewpoint. In this context, we have contributed to the state of the art in modeling dust-loaded pleated filters by developing macroscale Computational Fluid Dynamics (CFD) simulation methods for surface and depth filtration of mono- and poly-disperse aerosols (Fotovati *et al*., 2011, 2012; Saleh *et al*., 2014). These macroscale CFD simulation methods were developed using the information that was previously obtained from microscale simulations of both clean and dust-loaded flat sheet media (Wang, *et al*., 2006; Hosseini and Tafreshi 2010a, 2010b, 2010c; Fotovati *et al*.,2010; Hosseini and Tafreshi, 2012; Saleh *et al*., 2013). Again, note that the terms microscale and macroscale simulations are used here to refer to simulations on scales comparable to fiber and filters dimensions, respectively. These studies themselves were inspired from the many pioneering simulations for clean or dust-loaded single fibers such as those given in the work done by (Payatakes and Tien, 1976; Payatakes and Gradon, 1980; Kanaoka *et al*., 1980; Filippova and Hanel 1997; Kanaoka *et al*., 2001; Przekop *et al*.,2003; Lantermann and Haenel 2007; Li and Marshall, 2007). All the above studies, as well as many others similar to them in nature, are developed on the basis of solving some simplified forms of the Navier–Stokes equations via a numerical method, i.e., solving a partial differential equation. Such CFD simulations are often computationally very expensive making the approach unattractive for a real-life industrial product development. The semi-numerical method presented in this chapter, is therefore aimed at developing a simulation method that is practically CPU-independent (i.e., the CPU time is extremely short). This model allows one to simulate the entire lifecycle of a pleated filter in a few minutes, rather than few days CPU time (the typical completion time for the above-mentioned CFD simulations). As expected, this model can only produce an average profile for the shape of the dust-cake in a pleated filter, and so will be inaccurate in predicting phenomena that arise from the heterogeneity of the dust morphology such as premature clogging due to dendrites bridging across the pleat channel.

In the remainder of this chapter, we first present our model formulations for rectangular and triangular pleats with and without dust-loading (Secs. 5.2 and 5.3). We then discuss the implementation of the surface and depth filtration formulations in Sec. 5.4. In Sec. 5.5, we compare the predictions of the semi-numerical model to those obtained from more accurate macroscale CFD simulations and some experimental data from literature. Our results and discussion are given in Sec. 5.6 followed by our conclusions in Sec. 5.7.

5.2. Formulations for Rectangular Pleats

In this section, we first present our formulations for the flow and particle trajectory calculations in a clean rectangular pleat (Sec. 5.2.1). We then discuss two different patterns for the growth of dust-cakes inside rectangular pleats: cakes with uniform thickness (Sec. 5.2.2), and cakes with linearly growing thickness (Sec. 5.2.3). A mathematical treatment is given in Sec. 5.2.4 for the onset of clogging in the pleated filters followed by our modifications for the entrance region of rectangular pleats when formulating the flow of air and particles in Sec. 5.2.5.

5.2.1 Clean Pleats

Clean pleated filters have been studied in many previous investigations (Chen *et al*., 1995; Lucke *et al*., 1996; Subrenat *et al*., 2003; Wakeman *et al*., 2005; Waghode *et al*., 2007; Rebai *et al*., 2010; Lo *et al*., 2010). Some studies divide the pressure drop of by a pleated filter into a pressure drop due to geometry and pressure drop caused by the fibrous media, and some neglect the former in comparison to the latter, especially for filters having fibrous fabrics with low permeability (e.g., HEPA filets). Likewise, we ignore the pressure drop due to geometry. For clean fibrous media with uniform properties, the filtration velocities in the x and y directions, $u(l)$ $v(h)$, across the media is given by Darcy's law:

$$v(h) = u(l) = \frac{\Delta p}{t_m}\frac{k}{\mu} \tag{5.1}$$

where Δp is the pressure drop across the media, k is the permeability of the media, t_m is the thickness of the fibrous media, and μ is the air viscosity.

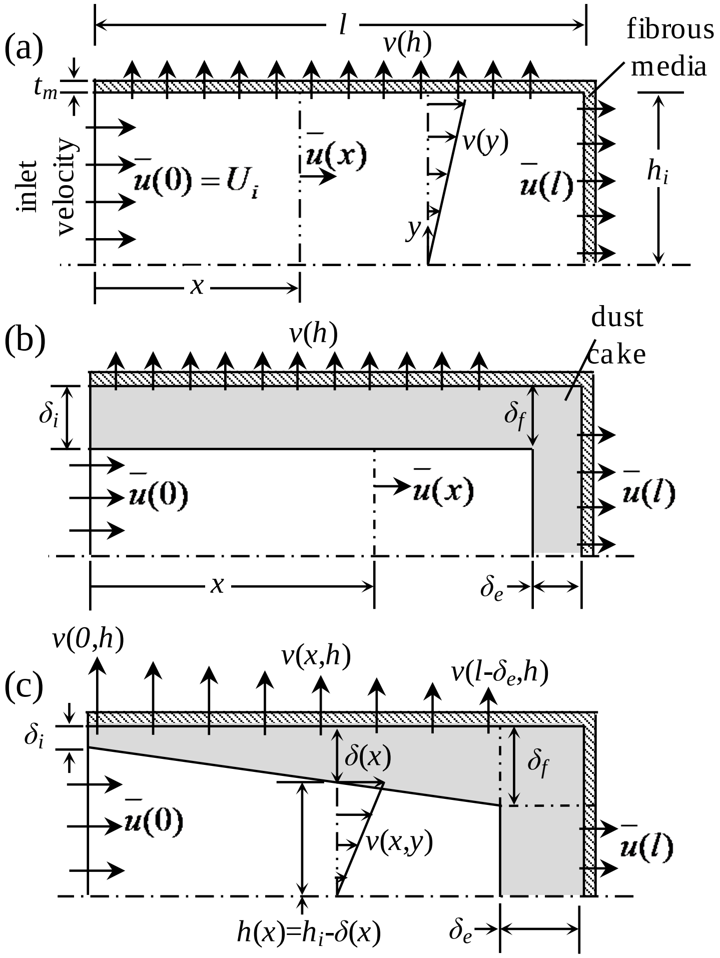

Fig. 5.1: Schematic drawing representing our model for rectangular pleats. Clean (a), uniformly loaded (b), and linearly loaded (c) channels.

Considering a control volume inside the pleat channel, the conservation of mass can be used to develop a relationship between filtration and inlet velocities:

$$U_i h_i = v\left(h_i\right) l + \bar{u}\left(x\right) h_i \tag{5.2}$$

where U_i is the inlet velocity, l is the pleat height, and h is the pleat half-width as shown in Fig. 5.1a. The average velocity $\bar{u}\left(x\right)$ can similarly be obtained using the conservation of mass,

$$\bar{u}\left(x\right) = U_i \left(1 - \frac{x}{l + h_i}\right) \tag{5.3}$$

In other words, the average axial velocity changes linearly with the axial position in the channel. The linear reduction in the axial velocity is due to the constant filtration velocity $v\left(h\right)$ by which air exits the channel from the top (note that for a clean filter $\bar{u}\left(l\right) = v\left(h\right)$).

In this work, we include the particle drag force in both axial and lateral directions. Trajectory of the particles can be obtained by integrating the force balance equation in the *x* and *y* directions written as follow

$$\frac{d^2 x_p}{dt^2} + \frac{1}{\tau}\frac{dx_p}{dt} = \frac{1}{\tau} u(x, y) \tag{5.4}$$

$$\frac{d^2 y_p}{dt^2} + \frac{1}{\tau}\frac{dy_p}{dt} = \frac{1}{\tau} v(x, y) \tag{5.5}$$

where $\tau = d_p^2 \rho_p c^c \mu^{-1} / 18$ is the particle relaxation time, and with the initial conditions given as $x(t=0) = 0$, $y_p(t=0) = y_p^i$, $\frac{dx_p}{dt}(t=0) = u_p^i$, and $\frac{dy_p}{dt}(t=0) = v_p^i$. The system of Ordinary Differential Equations (ODEs) given in Eqs. 5.4 and 5.5 can numerically be solved using a conventional Runge–Kutta method.

5.2.2 Uniform Dust Profile

The macroscale CFD simulations of (Fotovati *et al.*, 2011) revealed that particles with low inertia (e.g., small particles) tend to uniformly deposit on the horizontal walls of a rectangular pleat. On this basis, we have developed a uniform cake growth model for pleated filters loaded with such particles (see Fig. 5.1b). The thickness of the cake on the horizontal and the vertical walls of the channel are denoted by $\delta_i = \delta_f$ and δ_e respectively, and the filtration velocities across these walls, $v(h)$ and $\bar{u}(l)$, can be calculated based on the corresponding fractions of the particles that deposit on each one from the particle trajectory calculations.

$$\Delta p = v(h) r_i = \bar{u}(l) r_e \tag{5.6}$$

where $r_i = \frac{\mu t_m}{k} + \frac{\mu \delta_i}{k_c}$ and $r_e = \frac{\mu t_m}{k} + \frac{\mu \delta_e}{k_c}$ are the resistances to the flow across horizontal and vertical walls of the channel, and t_m is the thickness of the fibrous media. The cake permeability k_c can be obtained based on the Kozeny–Carman equation (Carman 1956):

$$k_c = \frac{d_p^2 c^c}{180} \frac{\varepsilon^3}{(1-\varepsilon)^2} \tag{5.7}$$

In this equation, the cake porosity ε is obtained from an empirical correlation proposed in the experimental work of Kasper *et al.*, 2010:

$$\varepsilon = 0.36 + 0.64 \exp\left(-0.29 \frac{\rho_p}{\rho_w} d_p \right) \tag{5.8}$$

Writing the continuity equation for a channel accommodating uniform dust-cake with thicknesses of δ_i and δ_e on its horizontal and vertical walls, we obtain

$$U_i h_i = v(h)(l - \delta_e) + \bar{u}(l)(h_i - \delta_i) \tag{5.9}$$

Solving the above equations, we can obtain expressions for filtration velocities across the horizontal and vertical fibrous walls, and consequently, predict the filter's instantaneous pressure drop. Likewise, the axial velocity along the pleat axis can be obtained as,

$$\bar{u}(x)=\frac{U_i h_i - xv(h)}{h_i-\delta_i} \tag{5.10}$$

The above expressions for the average air velocity in a pleat channel accommodating uniform dust can be used in the ODEs of Eqs. 5.4–5.5 to obtain the pressure drop and the particle collection efficiency of the dust-loaded filters.

5.2.3 Linear Dust Profile

For highly inertial particles (e.g., large particles), the macroscale CFD simulations of Fotovati *et al*., 2011 indicated that dust-cake tends grow from the pleat end, leaving clean areas on the horizontal walls near the channel entrance. Therefore, we considered a linear growth pattern for the dust-cake composed of such inertial particles as can be seen in Fig. 5.1c. In this model, with the dust-cake growing linearly on the pleat's horizontal wall, it is assumed that the filtration velocity also changes linearly along the pleat axis from $v(0,h)$ to $v(l-\delta_e,h)$. The pressure inside the pleat channel is assumed to be uniform and therefore the filtration velocities on the horizontal and vertical walls can be related as:

$$\Delta p = v(0,h)r_i = v(l-\delta_e,h)r_f = \bar{u}(l-\delta_e)r_e \tag{5.11}$$

where $r_i=\frac{\mu t_m}{k}+\frac{\mu\delta_i}{k_c}$, $r_f=\frac{\mu t_m}{k}+\frac{\mu\delta_f}{k_c}$,and $r_e=\frac{\mu t_m}{k}+\frac{\mu\delta_e}{k_c}$. Writing the continuity equation for the flow in the channel with the above filtration velocities and a uniform axial velocity of $\bar{u}(l-\delta_e)$ on the vertical wall, we obtain

$$U_i h_i = \frac{1}{2}\left(l-\delta_e\right)\left[v\left(0,h\right)+v\left(l-\delta_e,h\right)\right]+\overline{u}\left(l-\delta_e\right)\left(h-\delta_f\right) \tag{5.12}$$

Solving the above equations, we can obtain expressions for $v\left(0,h\right)$, $v\left(l-\delta_e,h\right)$ and $\overline{u}\left(l-\delta_e\right)$ in terms of the inlet flow velocity U_i. The filtration velocity across the horizontal wall $v\left(x,h\right)$ is given as,

$$v\left(x,h\right)=v\left(0,h\right)-\left[v\left(0,h\right)-v\left(l-\delta_e,h\right)\right]\frac{x}{l-\delta_e} \tag{5.13}$$

The average axial velocity at any cross-section along the pleat axis can be obtained as,

$$\overline{u}\left(x\right)=\frac{1}{h_i-\delta\left(x\right)}\left[U_i h_i - xv\left(0,h\right)+\frac{v\left(0,h\right)-v\left(l-\delta_e,h\right)}{2\left(l-\delta_e\right)}x^2\right] \tag{5.14}$$

As mentioned earlier, the method presented in the current work is built on the basis of the knowledge that was generated using our more accurate micro- and macroscale CFD simulations. The CFD results for flow inside a rectangular channel indicates that the *x* and *y* components of the velocity field can be represented by parabolic and sinusoidal profiles, respectively. Therefore, we assume

$$u\left(x,y\right)=\frac{3}{2}\overline{u}\left(x\right)\left[1-\left(\frac{y}{h\left(x\right)}\right)^2\right] \tag{5.15}$$

$$v\left(x,y\right)=v\left(x,h\right)\mathrm{Sin}\left(\frac{\pi}{2}\frac{y}{h\left(x\right)}\right) \tag{5.16}$$

Substituting these profiles in Eqs. 5.4 and 5.5, one can obtain the trajectory of the particles in the channel and thereby predict the collection efficiency and the pressure drop of the filter. Figure 5.2a shows the velocity profiles in different locations along the axis of a rectangular channel of a filter with 4 pleats per inch and an inlet velocity of 1 m/s. The fibrous medium in this filter is a mat of 9 µm fibers with an SVF of 7.5%. It can be seen that velocity decreases along the axis of the channel (the accuracy, e.g., mesh independence, of the CFD results shown here is examined in our previous studies as shown in Chapter 3, Fotovati *et al*., 2011 and Saleh *et al*., 2014. Figure 5.2b shows the flow axial velocity profile normalized by its local average value for different locations inside the pleat channel obtained from our CFD simulations. As can be seen in this figure, velocity profiles obtained from different locations along the axis have identical dimensionless profiles. We have, therefore, approximated the axial velocity profile inside the channel with a parabolic profile. Figure 5.2b also shows the y-velocity profiles across the length of the channel normalized using the maximum vertical velocity at pleat horizontal wall. We have approximated the y-velocity profile with a sinusoidal profile. Figure 5.2c shows the variation of the axial and lateral velocities across the pleat length obtained from the CFD simulations and those used here for our present approach.

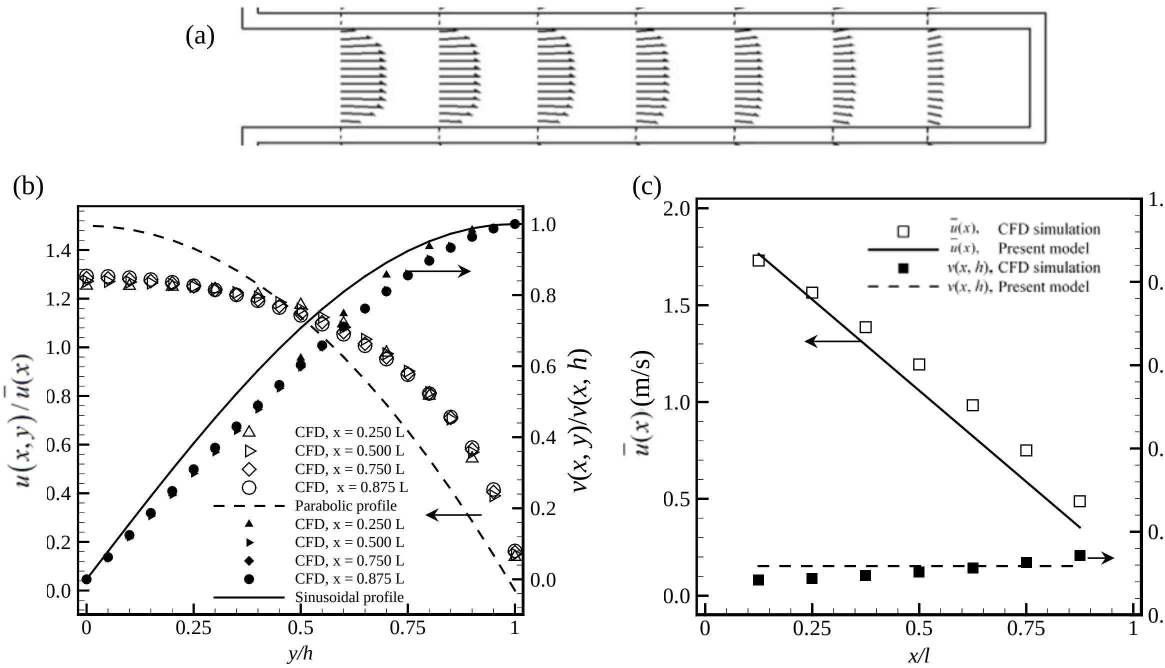

Fig. 5.2: Velocity vectors inside a rectangular channel obtained from CFD calculations for a filter with 4 pleats per inch (a). The *x* and *y* velocity components from CFD calculations are used to produce parabolic and sinusoidal profiles utilized in our present model (b). The average axial and maximum vertical velocities are shown as a function of position along the channel (c).

5.2.4 Onset of Clogging

The onset of clogging is defined here as the moment when the cake thickness somewhere on the channel's horizontal wall grows enough to reach the pleat axis. This definition is applied here regardless of which cake growth model (uniform or linear) is considered. For the case of uniform cake growth, we expect that the cake on the vertical wall (pleat end) will always be close to or equal to the thickness of the cake on the horizontal wall. For the case of linear cake growth, we have considered two sets of formulations for the onset of clogging. The first set is used when the cake thickness at the pleat end is thinner than the cake thickness on the horizontal wall near the end (Fig. 5.3a), and the second set is for when the cake thickness at the end has grown to become equal to that on the horizontal wall (Fig. 5.3b). In the latter, we have assumed that the channel end becomes impermeable. For as long as $\delta_e < h$, the flow is allowed to pass through the pleat end (that is for when $x \geq x_m$, where x_m is the distance at which the cake thicknesses are equal in the vertical and horizontal directions).

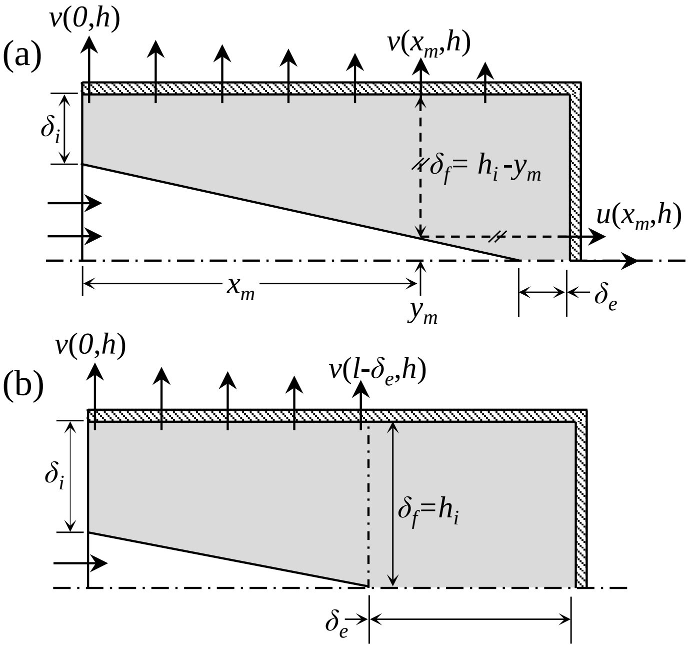

Fig. 5.3: Schematic drawing for linearly cake growth in the case of clogging for $\delta_e < h$ in (a) and $\delta_e > h$ in (b).

Following the aforementioned constant pressure assumption in the pleat channel, we can now obtain the following relationships between the filtration velocities.

$$\varDelta p = v(0,h)r_i = v(l-\delta_e,h)r_f = u(x_m,h)r_m = u(l-\delta_e,0)r_e \tag{5.17}$$

where $r_i = \frac{\mu t_m}{k}+\frac{\mu\delta_i}{k_c}$, $r_f = \frac{\mu t_m}{k}+\frac{\mu h}{k_c}$, $r_m = \frac{\mu t_m}{k}+\frac{\mu\delta_f}{k_c}$ and $r_e = \frac{\mu t_m}{k}+\frac{\mu\delta_e}{k_c}$.

Similarly, we can apply the continuity equation to provide another equation for filtration velocities:

$$U_i h_i = 0.5(l-\delta_e)\left[v(0,h)+v(l-\delta_e,h)\right] + 0.5y_m\left[u(l-x_m,h)+u(l-\delta_e,0)\right] \tag{5.18}$$

Solving Eqs. 5.17 and 5.18 simultaneously, one can obtain expressions for the velocities across the fibrous media $v(0,h)$, $v(x_m,h)$, $u(x_m,h)$ and $u(l-\delta_e,0)$ in terms of the inlet velocity. The filtration velocities across the top and the end of the pleat $v(x,h)$ and $u(x,h)$ can be represented as,

$$v(x,h) = \begin{cases} v(0,h) - \left[v(0,h)-v(l-\delta_e,h)\right]\dfrac{x}{l-\delta_e}, & x \le l-\delta_e \\ 0, & x > l-\delta_e \end{cases} \tag{5.19}$$

$$u(x,h) = \begin{cases} 0, & x < x_m \\ u(x_m,h) - \dfrac{x-x_m}{l-x_m-\delta_e}\left[u(x_m,h)-u(l-\delta_e,0)\right], & x \ge x_m \end{cases} \tag{5.20}$$

Accordingly, the flow axial velocity can be obtained as

$$\bar{u}(x) = \frac{1}{h(x)}\begin{cases} U_i h_i - \dfrac{x}{2}\left[v(0,h)+v(x,h)\right], & x \le x_m \\ U_i h_i - \dfrac{x_m}{2}\left[v(0,h)+v(x_m,h)\right] - \dfrac{y_m}{2}\dfrac{x-x_m}{l-\delta_e-x_m}\left[u(x_m,h)+u(x,h)\right] & \\ \qquad - \dfrac{x-x_m}{2}\left[v(x,h)+v(x_m,h)\right], & x > x_m \end{cases} \tag{5.21}$$

Same as before, with these updated velocity profiles Eqs. 5.4 and 5.5 can be solved to obtain the trajectory of the particles and the collection efficiency of the filter.

For the second scenario, i.e., when $\delta_e \geq h$, the resistance to the flow is higher at the pleat end. Therefore, we assumed that air flows through the pleat top only ($0 < x < l - \delta_e$). Therefore,

$$\Delta p = v(0,h) r_i = v(l-\delta_e,h) r_f \tag{5.22}$$

where $r_i = \frac{\mu t_m}{k} + \frac{\mu \delta_i}{k_c}$, and $r_f = \frac{\mu t_m}{k} + \frac{\mu h}{k_c}$.

Additionally, from the continuity equation we have,

$$U_i h_i = 0.5(l-\delta_e)\left[v(0,h) + v(l-\delta_e,h)\right] \tag{5.23}$$

Solving Eqs. 5.22 and 5.23, one can obtain expressions for $v(0,h)$ and $v(l-\delta_e,h)$ in terms of the inlet velocity (the filtration velocity across the horizontal wall of the pleat $v(x,h)$ follows Eq. 5.13 as discussed earlier). The average axial velocity $\bar{u}(x)$ inside the channel can be obtained from Eq. 5.14. The velocity components $u(x,y)$ and $v(x,y)$ can be obtained using the aforementioned parabolic and sinusoidal profiles, respectively. This information is then used to obtain the particle trajectories from Eqs. 5.4 and 5.5.

5.2.5 Initial Conditions for Particles Entering Rectangular Pleat Channels

The macroscale simulations of (Fotovati *et al*., 2011; 2012; and Saleh *et al*., 2014) showed that the air streamlines (and so the particle trajectories) contract as the flow enters into a rectangular pleat leading to the formation of a *vena contracta* at the channel's entrance. The vena contract forces the particles to move toward the axis of the pleat as can be seen in Figs. 5.4a and 5.4b. In order to obtain quantitative information for the initial position and velocity of the particles, a series of CFD simulations were conducted for the range of parameters of interest, i.e., pleat densities of 2–8 pleat/inch, flow velocities of 0.5–5 m/s, and particle diameters of 1–10 µm, along with a pleat height of 2.54 cm. These simulations were used to obtain the fraction of the incoming particles that actually enter into the pleat channel, referred to here as Pleat Entrance Ratio (PER) ψ. As can be seen in Fig. 5.4c, PER is different for filters with different pleat counts, and it varies from 0.6 for a filter with a pleat count of 8 per inch to about 0.72 for the case of 2 per inch in the case of tracking 10 µm particles. The number concentration of the particles injected into the domain was varied to ensure that our PER calculation is independent of the number of the particles injected. For these calculations the particles were injected from a distance equal to the height of the pleats, i.e., 2.54 cm, upstream of the pleat channel. Note that ψ is assumed to be one for filters with triangular pleats.

As can be seen from the example particle trajectories shown in Fig. 5.4b, the initial angle (with respect to the *x*-axis) by which a particle enters the pleat channel, i.e., entrance angle, depends on the position of the particle at the channel entrance. The entrance angle is a function of the flow velocity, particle inertia (here diameter), and pleat height, and is greater for particles farther away from the pleat axis.

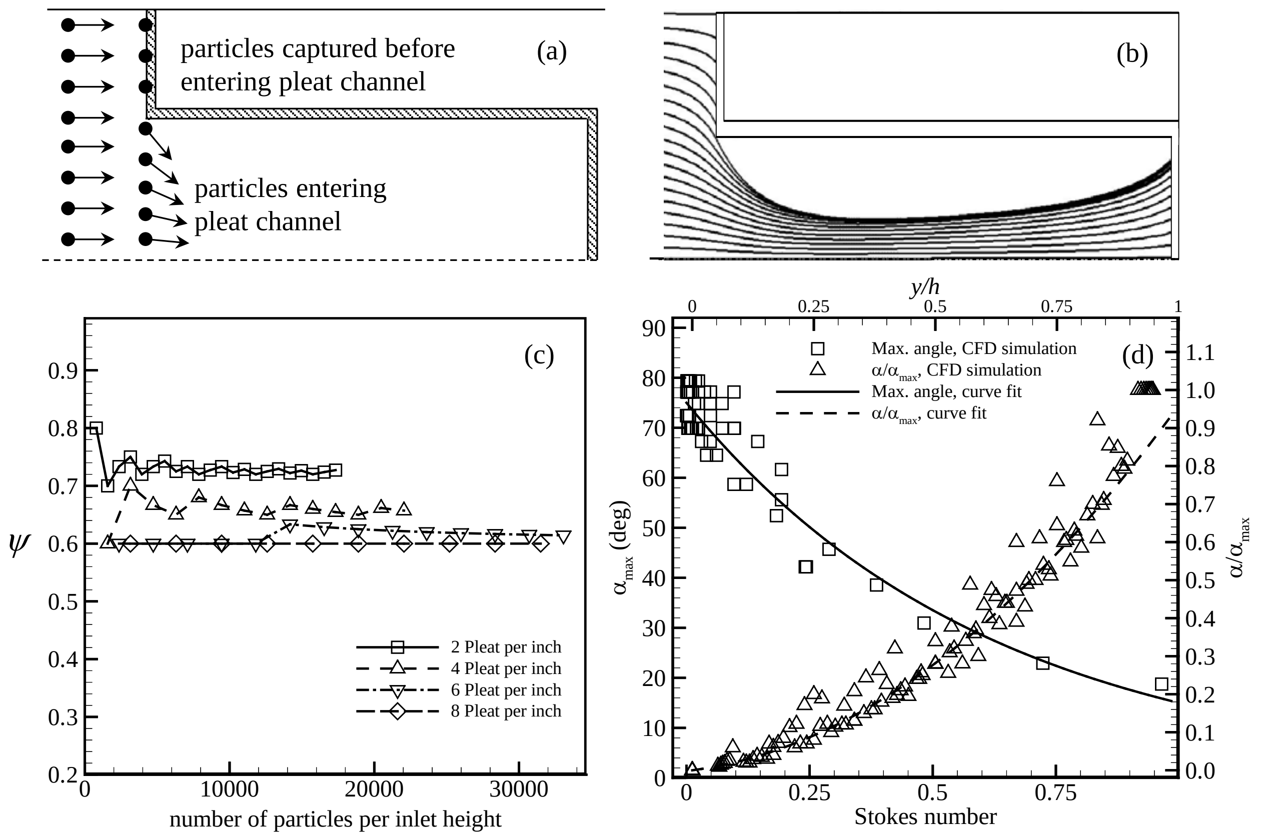

Fig. 5.4: Schematic drawing (a) and CFD particle trajectories (b) illustrating the definition of the PER. Particle inlet concentration effect on PER for filters with 2, 4, 6, and 8 pleats per inch challenged with particles with a diameter of 10 µm and at an air velocity of 5 m/s (c). Normalized and maximum inlet angles plotted versus Stokes number (d). The data are obtained from CFD simulations filters with 2, 4, 6, and 8 pleats per inch and particle diameters of 1, 2, 5, and 10 µm. The air velocities of 0.5, 1, 2, and 5 m/s are considered.

In fact, the entrance angle is smaller for inertial particles, as they do not follow the curvature of their streamlines very closely, and for filters with lower pleat counts. Particle entrance angles obtained from the abovementioned CFD simulations are normalized by their corresponding maximum values $\alpha_{\max} = \alpha(y = h_i)$ and plotted in Fig. 5.4d. A polynomial curve fit is then used to generate a mathematical expression for normalized entrance angle as a function of normalized particle position at the pleat entrance:

$$\frac{\alpha}{\alpha_{\max}} = \chi\left(\frac{y}{h_i}\right)^2 + \varsigma\frac{y}{h_i} \qquad (5.24)$$

where $\chi = 0.78$ and ς=0.16. Figure 5.4d shows the maximum entrance angle $\alpha_{\max}$ as a function of Stokes number defined here in terms of pleat width as $\mathrm{St} = \frac{\rho_P\, d_P^2\, c^c\, U_i}{18\mu(2h_i)}$, where c^c is the Cunningham slip correction factor. We curve fitted an exponential function into our CFD simulation data to obtain an expressions for the maximum entrance angle in terms of Stokes number,

$$\alpha_{\max} = \zeta e^{-\omega St} \tag{5.25}$$

where $\zeta = 75$ and $\omega = 1.61$.

Equations 5.24 and 5.25 provide the necessary information for correctly assigning an initial (i.e., entrance) angle to the particles at the pleat entrance.

For the sake of simplicity, we have assumed that the particles entering a rectangular pleat are distributed uniformly across the entrance plane. While this is not exactly accurate, as the off-axis streamlines may tend to be closer to one another, the error associated with this assumption is negligible as can be seen in Fig. 5.5a. In this figure, the spatial distribution of particles of 1 to 10 micrometer in diameter is shown as they enter the pleat channel. Inlet velocities and pleat counts in the range of 0.5 to 5 m/s and 2 to 8 per inch, are considered in this figure, respectively.

Our semi-numerical model (while written in terms of flow velocity upstream of the filter), is developed for the flow inside the pleat channel only. Therefore, the flow and particle velocities at the channel entrance should be modified before the formulation can correctly represent the actual flow facing a pair of pleats (see the inset in Fig. 5.5b).

In this concern, we have obtained the ratio of the average air velocity at the pleat entrance to the flow velocity upstream of the filter from our CFD simulations (see Fig. 5.5b). It can be seen that flow velocity entering the channel is about two times higher than that upstream of the filter. In addition, some of the particles deposit on the pleat vertical wall, and so, do not enter the pleat channel (see Fig. 5.4a and 5.4b).

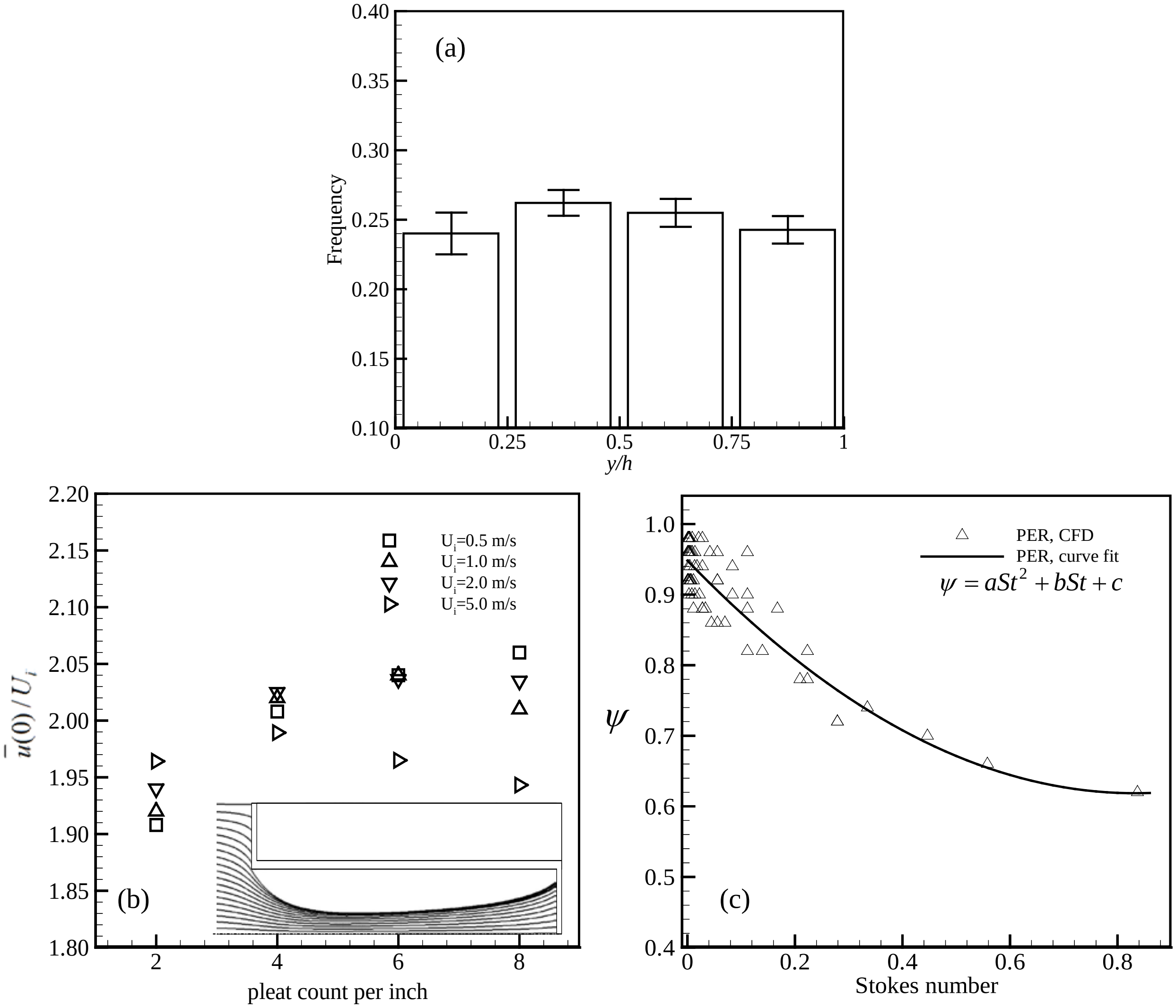

Fig. 5.5: Particle distribution at channel entrance averaged over particles with diameters in the range of 1 to 10 µm entering channels with 2, 4, 6, and 8 pleats per inch with inlet velocities of 0.5 to 5 m/s (a). Average air velocity at channel entrance normalized with the far field upstream velocity (b). PER calculated from the CFD simulation results and its curve fit.

A correction factor is therefore needed to account for these particles. Hence, we plotted ψ as a function of Stokes number from CFD simulations for inlet velocities, particle diameters, and pleat counts in the range of 0.5 to 5 m/s, 1 to 10 µm, and 2 to 8 per inch, respectively. These results are used to produce a mathematical correlation in the form of $\psi = aSt^2 + bSt + c$ where a, b and c are constant values obtained from curve fitting (see Fig. 5.5c).

Figure 5.6 shows the effects of Stokes number on particle trajectories in rectangular pleats. It can be seen that particles with higher Stokes number tend to deposit deeper in the pleat channel. In this figure, note the region on the horizontal wall inaccessible to particles with high Stokes numbers. This peculiar property of the particle trajectories is the key factor here in deciding between the choice of a uniform or a linear growth pattern for the dust cakes.

Our observations of the particle trajectory patterns inside rectangular channels indicated that a Stokes number of 0.1 is a good criterion for deciding between the two models. For $St < 0.1$ particle deposition (and so the cake growth) is considered uniform, whereas for $St > 0.1$ the cake growth is better represented with a linear profile. The ratio of the cake thicknesses at half way through the channel and at the channel end $\delta(l/2)/\delta_f$ is set equal to the ratio of the number of particles deposited on the first half of the channel horizontal wall to that on the second half, as shown in Fig. 5.6f.

(a) d_p =1 μm, inlet velocity =0.5 m/s (St ▯ 0)

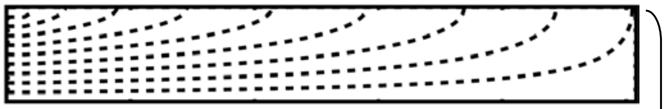

(b) d_p =10 μm, inlet velocity =0.5 m/s (St=0.05)

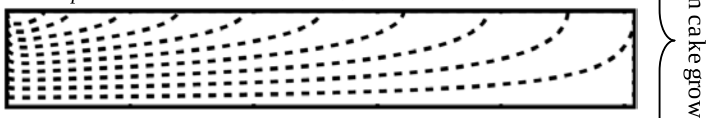

(c) d_p =10 μm, inlet velocity =1 m/s (St=0.10)

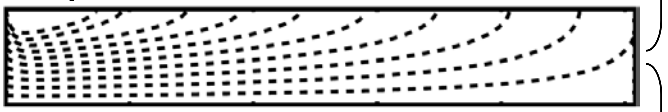

(d) d_p =10 μm, inlet velocity =1.5 m/s (St=0.15)

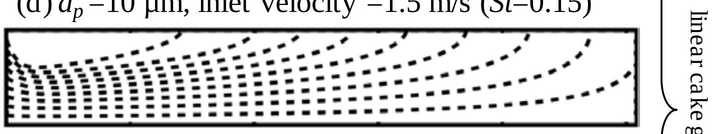

(e) d_p=10 μm, inlet velocity =5 m/s (St=0.5)

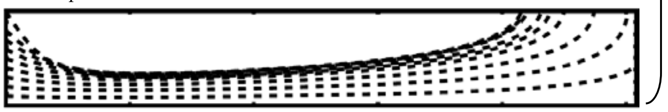

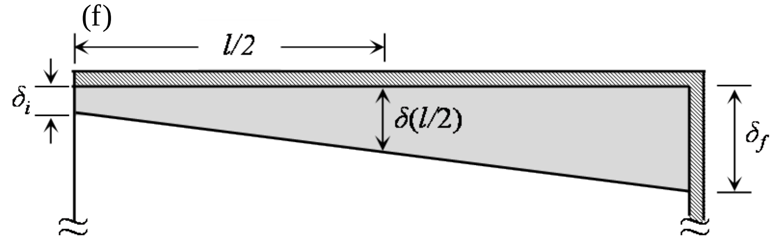

Fig. 5.6: Effects of Stokes number on particle trajectory for Stokes numbers ranging from about zero to 0.5 from (a) through (e) for a filter with 4 rectangular pleats per inch. Beyond a Stokes number of 0.1 the particle deposition inside the channel starts to become non-uniform. Dashed lines show the particle trajectories inside the pleat channel. A schematic drawing illustrating the ratio of the cake thicknesses obtained on the basis of the fraction of particles deposited on the first and second halves of the pleat horizontal wall.

5.3. Formulations for Triangular Pleats

The filtration velocity, being normal to the fibrous media, forms an angle $\pi/2-\theta$ with the x-direction for the case of triangular pleats with a half pleat angle of θ (see Fig. 5.7a). Using the continuity equation for clean filters

$$U_i h_i = v_w W = v(x,h)\frac{W}{cos\theta} \tag{5.26}$$

where W is the length of the pleat wall, and v_w is the filtration velocity perpendicular to it. The average axial velocity along the *x*-direction in the pleat channel can be derived as

$$\bar{u}(x) = \frac{1}{h(x)}\left(U_i h_i - v(x,h)\frac{xW}{l\,cos\theta}\right) \tag{5.27}$$

The vertical filtration velocity $v(x,h)$ can be obtained from the following expression:

$$v(x,h) = v_w\,cos\theta \tag{5.28}$$

These flow velocity expressions can be used in Eqs. 5.4 and 5.5 to obtain the trajectory of the particles inside the pleat channel. Since a *vena contracta* is not likely to form in a triangular pleat, we assumed that the dust growth on the pleat walls will be uniform as depicted in Fig. 5.7b.

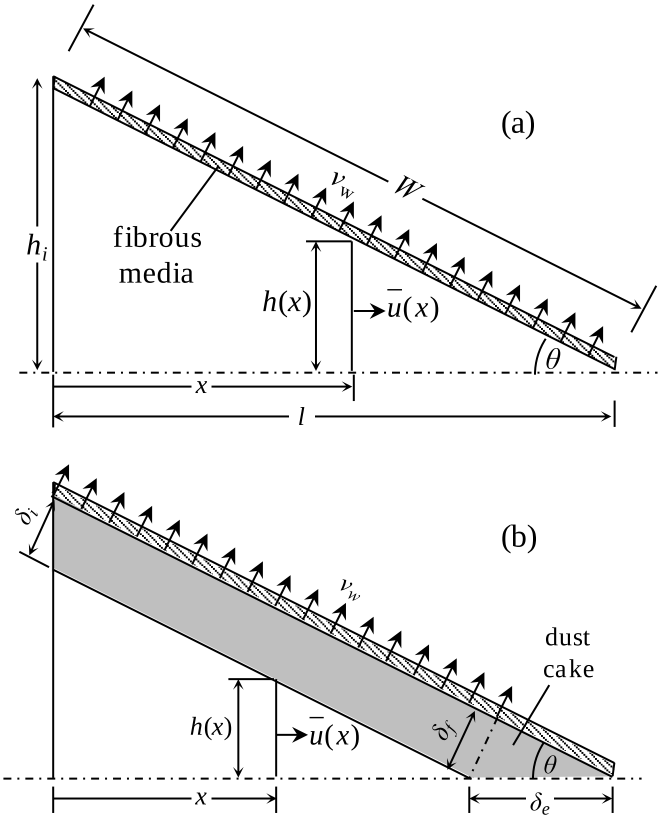

Fig. 5.7: Schematic drawing representing our present model for triangular pleats. Clean (a), and dust-loaded (b) pleats.

A constant cake thickness, obviously, leads to a constant filtration velocity across pleat walls. For dust-loaded filters, we again use Darcy's law and continuity equation to derive equations for vertical filtration velocity $v(x,h)$,

$$\Delta p = \frac{v(x,h)}{\cos\theta} r \tag{5.29}$$

$$U_i h = \frac{v(x,h)}{\cos\theta}\left(W - \delta_e \cos\theta\right) \tag{5.30}$$

where $r = \frac{\mu t_m}{k} + \frac{\mu \delta_f}{k_c}$.

The average axial velocity along the axis of a dust-loaded triangular pleat channel can be expressed as:

$$\bar{u}(x) = \frac{1}{h(x)}\left(U_i h_i - \frac{v(x,h)}{\cos\theta}\left(W - \delta_e \cos\theta\right)\frac{x}{l - \delta_e}\right) \tag{5.31}$$

On the basis of our CFD simulation results, we used parabolic and fourth order profiles for the *x* and *y* components of the velocity field inside a triangular pleat, respectively (see Sec. 5). Therefore, $v(x,y) = v(x,h)\left[a\left(\frac{y}{h(x)}\right)^4 + b\left(\frac{y}{h(x)}\right)^3 + c\left(\frac{y}{h(x)}\right)^2 + d\,\frac{y}{h(x)}\right]$ (5.32)

where $a,\ b,\ c,$ and d are obtained via curve fitting.

Figure 5.8a shows an example of a velocity field inside a triangular channel in a filter with a pleat count of 4 per inch made of a fibrous medium with a fiber diameter of 15 µm and an SVF of 7.5%. Figure 5.8b depicts the non-dimensionalized axial and vertical velocity profiles at different locations along the pleat channel. It can be seen that a parabolic profile seems to be a reasonable approximation for axial velocity in the channel. For the y-velocity, we have approximated the profile with a fourth-order polynomial function of (y/h) as shown in Fig. 5.8b (the coefficients in Eq. 5.32 are obtained by curve fitting to the data shown in this figure). The x and y velocity components in Fig. 5.8b are normalized with the average axial velocity $\bar{u}(x)$ and the vertical velocity at the fibrous medium $v(x,h)$ (see Fig. 5.8c). Note that $\bar{u}(x)$ and $v(x,h)$ in triangular pleats do not significantly vary along the length of the channel, unlike the case of flow in rectangular pleats.

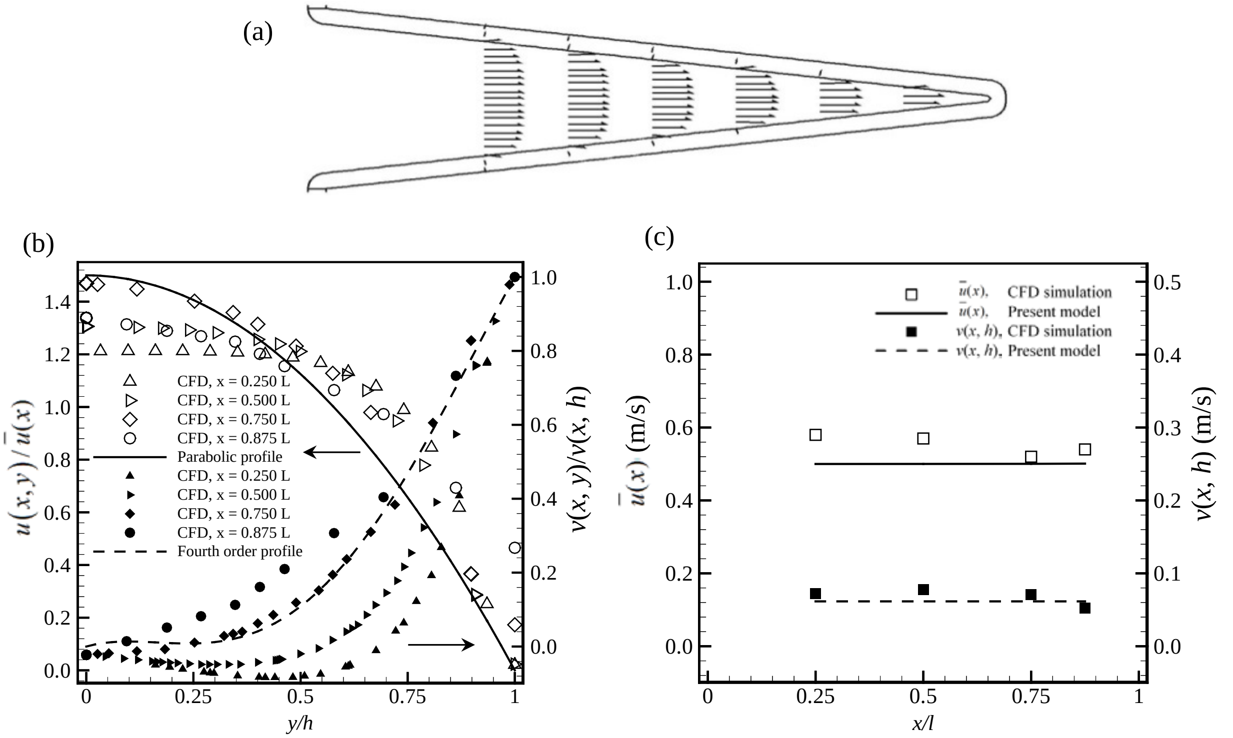

Fig. 5.8: Velocity vectors inside a triangular channel obtained from CFD calculations for a filter with 4 pleats per inch (a). The *x* and *y* velocity components from CFD calculations are used to produce parabolic and forth order profiles utilized in our present model (b). The average axial and maximum vertical velocities are shown as a function of position along the channel (c).

Figure 5.9 shows the effect of Stokes number on particles trajectories in triangular pleats. As can be seen in this figure, Stokes number has a negligible effect on the particle trajectories or the particle deposition sites. Therefore, the cake is assumed to grow uniformly in the direction normal to the wall.

(a) 4 pleat/inch, inlet velocity =0.5 m/s (*St*=0.02)

(b) 4 pleat/inch, inlet velocity =1m/s (*St*=0.05)

(c) 4 pleat/inch, inlet velocity =5 m/s (*St*=0.24)

Fig. 5.9: Effects of Stokes number on particle trajectory for Stokes numbers ranging from about 0.02 to 0.24 from (a) through (c) for a filter with 4 triangular pleats per inch. Dashed lines show the particle trajectories inside the pleat channel.

5.4. Depth and Surface Filtration

As mentioned earlier, the model presented in this work can predict both the collection efficiency and pressure drop of dust-loaded pleated filters. For the efficiency predictions, we obtain the initial efficiency of the pleated filter from the cell model equations using the filtration velocities derived in Secs. 5.2 and 5.3.

Particle collection efficiency of a fibrous sheet can be estimated using the well-known Single Fiber Efficiencies (SFEs) from literature as shown in appendix A. These equations are developed for clean fibrous structures (valid only for the early stages of a filter's service life). Our approach to model the collection efficiency of particle-loaded media has been to assume that the deposition of particles inside a fibrous structure only affects its SVF. The loaded particles increase the SVF of the filter and hence its collection efficiency. For the sake of simplicity in our present model, we also assume that the filtration efficiency of a fibrous structure increases linearly with the mass of the particles deposited within the structure (Chapter 3). We assume collection efficiency of the filter reaches 100% when the SVF of the particles within the fibrous media reaches a maximum value defined by the porosity value in Eq. 5.8 (SVF is equal to $1-\varepsilon$). The instantaneous efficiency of the filter for SVFs smaller than the maximum allowable value is calculated via linear interpolation between the clean efficiency, at the SVF of the media, and 100%, at the maximum SVF.

For calculating the pressure drop of particle-loaded fibrous media, we use a more realistic approach: we assume that pressure drop of the particle-loaded media is the summation of pressure drop caused by the clean fibers and that due to deposited particles. We used the un-weighted resistivity method of (Mattern and Deen, 2007) for its simplicity as well as accuracy. The un-weighted resistivity model adds up the above-mentioned resistances with no weight factors:

$$r_l = r_m + r_p = \frac{\mu t_m}{k\ (\phi_m)} + \frac{\mu t_m}{k_c(\phi_p)} \qquad (5.33)$$

where r_l, r_m, and r_p are the resistance of particle-loaded media, clean media, and the particles deposited within the media.

5.5. Comparison with CFD Simulation

Like any measurement tool, the accuracy of a low-resolution computational tool can be verified using a computational tool that has a better resolution. This is of course in addition to benchmarking the results with accurate and reliable experimental data if available. In this section, we present three different studies in which we compare the results of our simple analytical model with those obtained from the more sophisticated (and so more realistic) CFD simulations (as discussed in Chapter 3). We also present a comparison with the experimental data of (Gervais *et al.*, 2014) obtained for pleated HEPA filters.

5.5.1 Surface Filters with Rectangular Pleats

Figure 5.10 presents the pressure drop values and cake profiles of rectangular surface filters (collection efficiency of 100%) when loaded with dust particles with a diameter of 10 µm at inlet velocity of 1 m/s. The fibrous media has a through-plane permeability value of k=5.4×10^{-11} m^2 (see Fotovati *et al.*, 2011 for more information about the in-plane and through-plane permeability of fibrous structures). We considered a fiber diameter of 9 µm, a media thickness of 0.5 mm, and an SVF of 7.5% for this comparison. Figure 5.10a shows the pressure drop vs. mass loading per unit area for a 4 pleats per inch rectangular filter at an inlet velocity of 1 m/s. Two particle diameters of 1 µm (*St*=0.002) and 10 µm (*St*=0.2) are considered to represent the uniform and linear dust-cake growth patterns, respectively.

The CFD predictions are obtained and compared with the predictions of our semi-numerical method. Figures 5.10b and 5.10c compare the dust-cake profiles obtained from our present model with the more accurate, but CPU-intensive, CFD calculations. As can be seen in these figures, increasing the particle diameter (Stokes number) results in non-uniform dust-cake formation leaving a large portion of the pleat's horizontal wall practically clean. As mentioned earlier, in constructing a linear dust-growth pattern, we use the particle trajectories to determine a slope of the cake profile. For instance, for the case with 10 µm particles, the ratio of the particles deposited in the first half of the horizontal wall to that in the second half was found to be about 0.25 (based on our semi-numerical model particle trajectory calculations). Therefore, a slope of $\delta_i / \delta_f = 0.125$ was considered for the cake profile (see Fig. 5.6f).

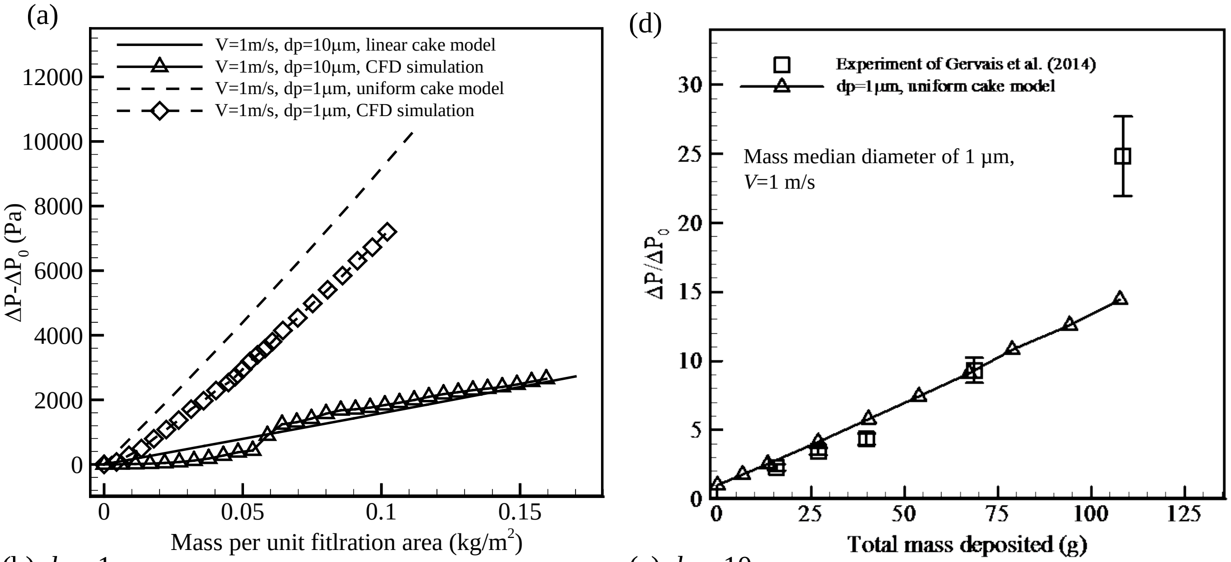

(b) d_p = 1 μm (c) d_p = 10 μm

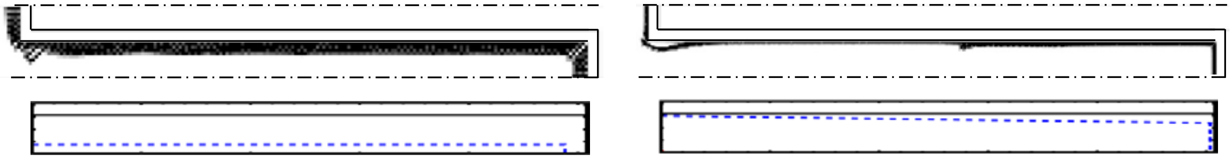

Fig. 5.10: Comparison between pressure drop predictions of the present model and our CFD calculations for a filter with 4 rectangular pleats per inch in surface filtration regime (a). Two particle diameters of 1 and 10 μm are considered at an air velocity of 1 m/s. Dust-cake profiles obtained from the present model and the macro-scale CFD calculations at a mass loading of 0.1 kg/m^2 mass deposited per unit filtration area are compared in (b) and (c). The blue dashed lines show the dust-cake in the present model.

In addition, in this section we also present a comparison with the recent experimental data given in the work of (Gervais *et al.*, 2014) for pleated HEPA filters loaded with poly-dispersed alumina dust (ρ=3970 kg/m^3) with a mass median diameter of 1μm and a geometric standard deviation of 3.2. The fabric of the filter used in the experiments of (Gervais *et al.*, 2014) is reported to have a thickness of 521 μm, a packing density of 7.1%, and was made of fibers with a count median diameter of 0.6 μm. The pleat height and pitch are reported to be 27.5 and 2.2 mm, respectively.

The study by Gervais *et al*., 2014 reports pressure drop measurements as a function of the cake mass.

To predict the pressure drop of the pleated filter, we first obtained the permeability constant of its fabric from the reported initial pressure drop (200 Pa) and air velocity (0.046 m/s) using Darcy's law. We then considered our uniform dust-cake growth model based on the Stokes number of the particles. Since our model is developed for mono-dispersed dust, we considered the mass median diameter of the particles (1 µm) as a representative size in Eqs. 5.7–5.8. Our predictions of the filter's pressure drop are plotted in Fig. 5.10d as a function of cake mass. Good agreement between the simulation and experimental data is evident except for when the filter is about to be totally filled with particles (about 110 g according to the experiments reported in the work of Gervais *et al*., 2014 and 120 g in our semi-numerical simulations).

5.5.2 Surface and Depth Filters with Rectangular Pleats

In this section, we considered a more complicated filtration regime in which the particles can deposit both inside and outside the fibrous media in a pleated filter. We compare the results of our present model with those of the 3-D macroscale simulations. The fibrous medium considered here has an SVF of 7.5% with a fiber diameter of 15 µm. The corresponding fibrous media has a through-plane permeability constant of k=1.6×10^{-10} m^2. The macroscale model was discussed in detail in Chapter 3. In Fig. 5.11 we present the predictions of the present model along with those of the above-mentioned 3-D macroscale CFD simulations for a filter with a pleat count of 4 per inch loaded with 1 µm particles at an inlet velocity of 0.1 m/s. Given the complexity of the problem at hand, the general agreement shown in Fig. 5.11a is appreciable (see the complicated cake morphology and its present model counterpart in Figs. 5.11b). Note that pressure drop and collection efficiency predictions obtained from the CFD simulations show slower rates of increase in comparison to those obtained from the analytical formulations. This is because, unlike the case with our semi-numerical model, the dust cake in the CFD simulations (and in reality) does not start as a perfectly thin layer of particles deposited uniformly all over the pleat channel. In reality, the deposition starts non-uniformly but becomes more uniform over time as the areas with thicker cake resist against the air flow and so redirect the particles toward areas with less deposition. Also, recall that our present model does not consider any premature clogging or dendrite bridge formation across the pleat channel. Therefore, the pressure drop prediction from the model does not show a sudden increase, as may be the case with the CFD simulations. Particle trajectories, obtained from the CFD calculation and our semi-numerical method, are shown in Fig. 5.10c for comparison.

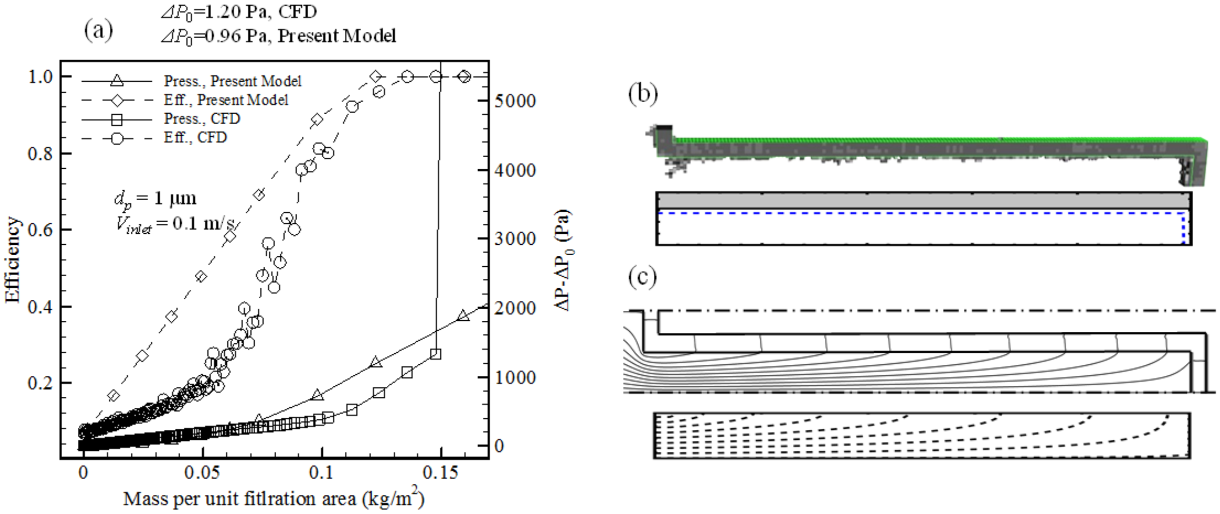

Fig. 5.11: Comparison between pressure drop and collection efficiency predictions of the present model and our CFD calculations for a filter with 4 rectangular pleats per inch in surface and depth filtration regimes (a). A particle diameter of 1 µm is considered at an air velocity of 0.1 m/s. Dust deposition patterns and clean particle trajectories are compared in (b) and (c), respectively. The mass loading shown in (b) is 0.11 kg/m^2. The blue dashed lines show the dust-cake in the present model. The black dashed and black solid lines show the particle trajectories in the present and CFD simulations, respectively. Figure (d) shows a comparison between the results of our present model and the experimental data of Gervais *et al.,* 2014.

5.5.3. Surface and Depth Filters with Triangular Pleats

Similar to the case discussed in Sec. 5.5.2, here we also consider both the surface and depth depositions, but now for a triangular pleat with a pleat count of 4 per inch. Similarly, fiber diameter, SVF, inlet velocity, and particle diameter are 15 µm, 7.5%, 0.5 m/s, and 1 µm, respectively. Figure 5.12 presents a comparison between the predictions of our model with those of the aforementioned 3-D macroscale CFD simulations for a filter with a 4 triangular pleats per inch loaded with 1 µm particles at an inlet velocity of 0.5 m/s. Once again, the agreement between the two methods is reasonably good, given the complexity of the problem (see Fig. 5.12a). The dust-cakes and particle trajectories are also compared in Fig. 5.12b and 5.12c.

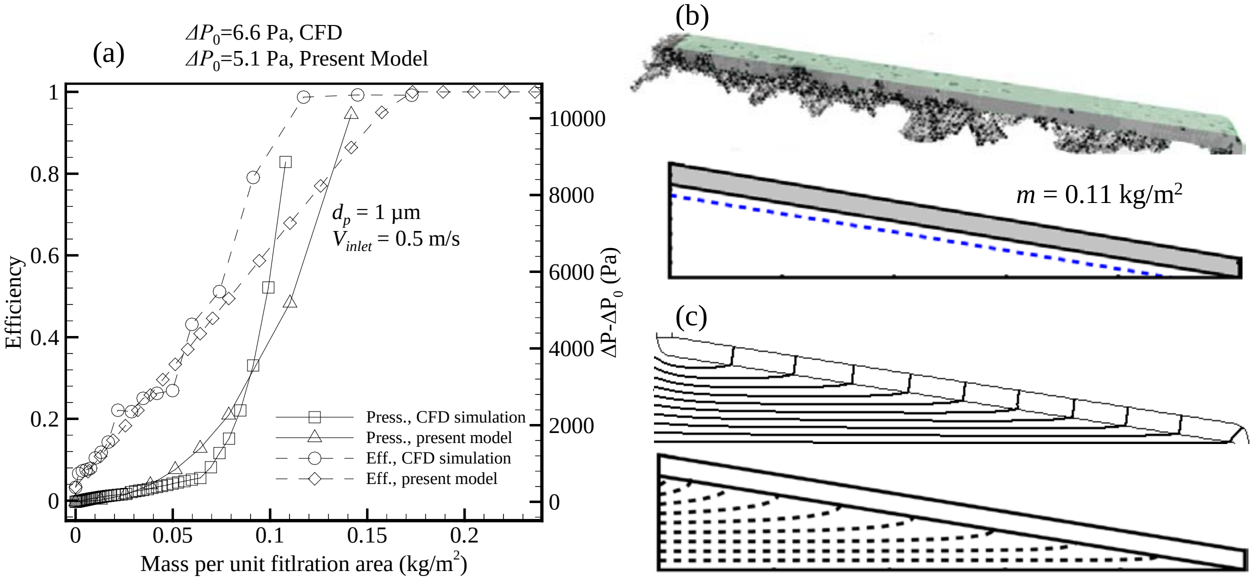

Fig. 5.12: Comparison between pressure drop and collection efficiency predictions of the present model and our CFD calculations for a filter with 4 triangular pleats per inch in surface and depth filtration regimes (a). A particle diameter of 1 µm is considered at an air velocity of 0.5 m/s. Dust deposition patterns and clean particle trajectories are compared in (b) and (c), respectively. The mass loading shown in (b) is 0.11 kg/m^2. The blue dashed lines show the dust-cake in the present model. The black dashed and black solid lines show the particle trajectories in the semi-numerical and CFD simulations, respectively.

5.6. Results and Discussion

In this section, we present a brief parameter study investigating the effects of pleat geometry and aerosol properties on the service life of rectangular and triangular pleated filters. Figure 5.13 shows the instantaneous collection efficiency and pressure drop increase values of filters with 2 and 4 pleats per inch for rectangular pleats when loaded with particles of 1, 5, and 10 µm diameters at an inlet velocity of 1 m/s as a function of time and loading per unit filtration area. An aerosol mass concentration of 2.52×10^{-7} kg/m^3 is considered for all simulations. As expected, increasing the pleat count generally helps to reduce the rate by which pressure drop (and collection efficiency) increases over time because, when the pleat count is higher, each pleat channel receives less mass per unit time. To better illustrate the growth of the dust-cakes in filters discussed in Fig. 5.13, we have also presented sample cake profiles for each case for arbitrary mass depositions corresponding to points marked with a star in Fig. 5.13. Note that the cake thickness is about the same in both filters with 2 and 4 pleats per inch. This is because at a given mass per unit filtration area, there is more mass deposited in the filter with the higher pleat count as it has a higher surface area (the filter with 4 pleats per inch has a filtration area about two times greater than the filter with 2 pleats per inch and so it has about two times the mass loaded). The pressure drop caused by the filter with higher pleat count is lower as its face velocity is about two times smaller.

In Fig. 5.13, note how the filtration regime changes from the initial depth-and-surface filtration to surface filtration as more mass deposit in the filters challenged with 1 and 5 µm particles. It is important to mention that collection efficiency reaches 100% with almost the same amount of mass deposited for both pleat counts. This is because it takes the same amount of mass (but not the same amount of time) to clog the pores of the filter media, regardless of the pleat count. Beyond this point, the filter operates in the surface filtration regime. For particles of 10 µm diameter, the filters operate in surface filtration regime as 10 µm particles, cannot penetrate through the fabric of the filter. Also note that, the initial collection efficiency (efficiency in the absence of dust loading) does not vary significantly with varying the pleat count for the case of aerosols with 1 and 10 µm particles. However, this is not the case for particles with a diameter of 5 µm as shown in Figs. 5.13b.

To better understand the underlying reason behind this effect, one should pay a closer attention to how the collection efficiency of a fibrous sheet varies with particle diameter for face velocities corresponding to those experienced by the channel walls (see Fig. 5.14). It can be seen that, for particles of 1 and 10 µm in diameter, collection efficiency is almost independent of face velocity (Equations 5.33–5.36). However, for particles with a diameter in the neighborhood of 5 µm, the dependence is noticeable.

Note that for all cases shown in Fig. 5.13, we have used a uniform cake growth model except for the case of filters with 4 pleats per inch loaded with 10 µm particles (the figure on the right in Fig. 5.13c) where a linear cake growth model is considered as a non-uniform cake growth was expected. In this figure, note the point at which the pressure drop starts to increase at a higher rate (at time of 440 days and a corresponding mass loading of about of 1.1 kg / m^2). This point depicts the onset of clogging for this filter. Note also the maximum SVF is higher for dust-cakes comprised of larger particles, i.e., it takes a larger amount of mass (not to be confused with the number of particles) to fill up the pleat channel with larger particles.

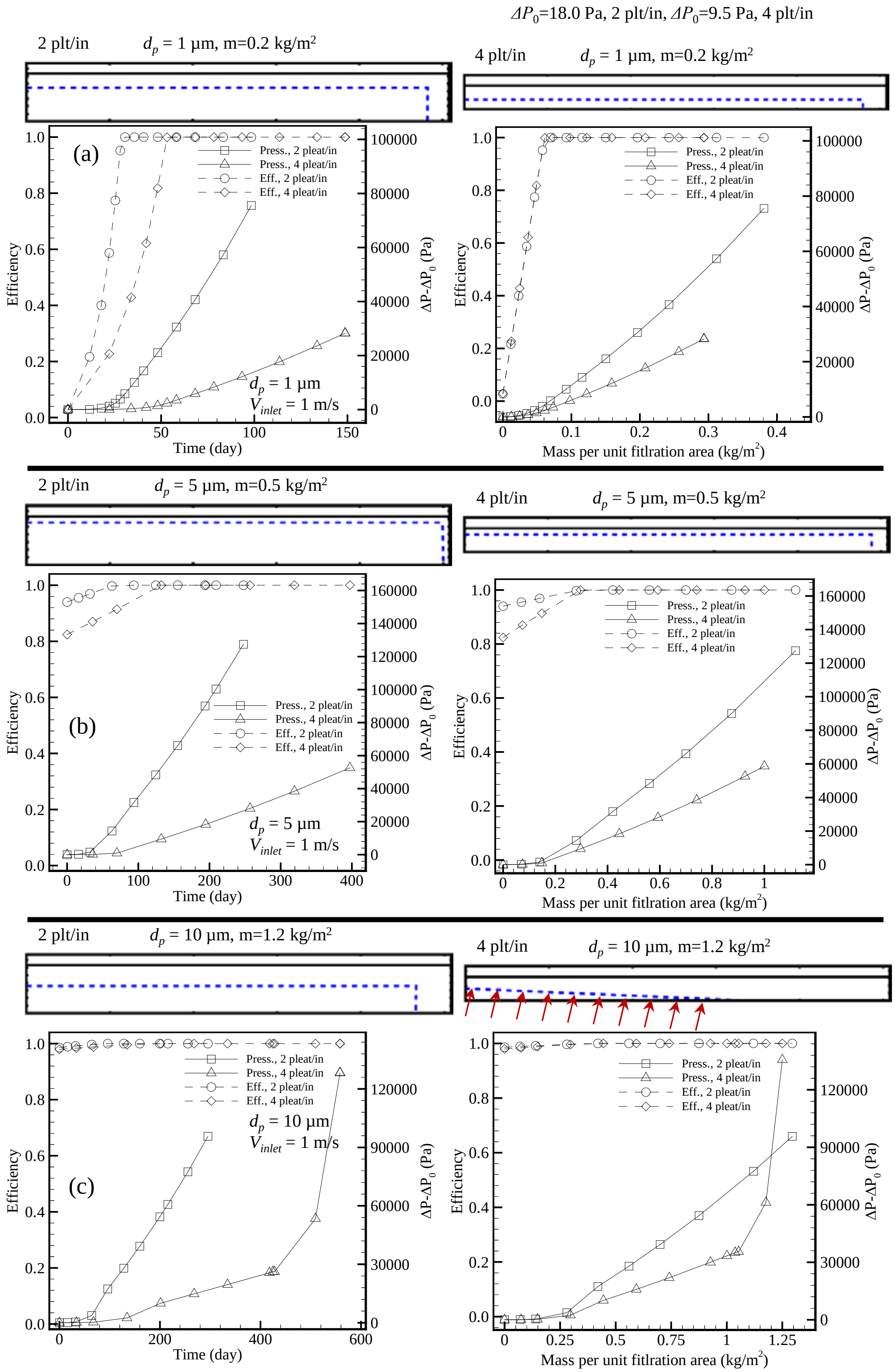

Fig. 5.13: The evolution of collection efficiency and pressure drop with time for filters with 2 and 4 rectangular pleats at an inlet velocity of 1 m/s as a function of loading time and mass deposited per unit filtration area. Particles with a diameter of 1, 5, and 10 µm are considered in (a), (b), and (c), respectively. Sample dust-cake profiles are given for each case for illustrations. The blue dashed lines show the dust-cake in the present model.

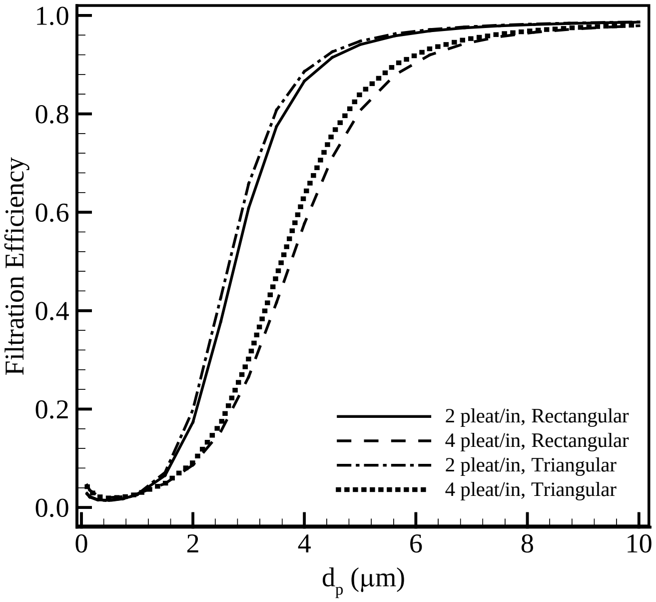

Fig.5.14: Cell-model clean-filter efficiency predictions as a function of particle diameter for flat-sheet fibrous media at face velocities equal to those of rectangular and triangular pleats having an inlet velocity of 1m/s.

Figure 5.15 shows the performance of triangular channels with pleat counts of 2 and 4 per inch challenged with the aerosol flow as described in Fig. 5.13. Similarly, sample dust-cake profiles are added to the figure for illustration purposes. These profiles correspond to points marked with a star in Fig. 5.15.

Comparing the predictions given in Fig. 5.13 and Fig. 5.15 indicates that the instantaneous pressure drop caused by loaded rectangular pleats is generally less than that of their triangular counterparts. The reason for this is threefold. First, some fractions of the incoming particles tend to deposit on the front face of the filter outside the channel for when the pleat shape is rectangular. This means that less number of particles actually enter the pleat channel. Note that the particles depositing outside the pleat channel may cause some pressure drop for a filter with rectangular pleats. This pressure drop, however, is expected to be relatively small, and is not included in our model. The second cause for the higher pressure drop in the triangular pleats is that the dust-cake can quickly grow to reach the channel axis and render a large portion of the fabric inaccessible to air flow in regions near the end of the pleats (see the regions shown with arrows in Fig. 5.13c and 5.15c). For instance, for the case shown in Fig. 5.15c, the area available to air flow is about (for both 2 and 4 pleats per inch filters) 25% larger in the case of rectangular pleats leading to a lower pressure drop value. The third reason for the rectangular pleats showing smaller pressure drop seems to be due to the fact that for the same pleat length and height, the total area of the filter (total surface area of the pleat walls) is up to about 4% higher when the pleats are rectangular (see the clean pressure drop values reported in Fig. 5.13 and Fig. 5.15.

Finally, as mentioned earlier, that the presnent model developed in this study does not include the effects of dendrite formation inside or outside the pleat channels. Therefore, despite their superior performance shown in Figs. 5.13 and 5.15, rectangular pleats may exhibit premature clogging due to particle dendrite formation at high mass loadings or high pleat counts.

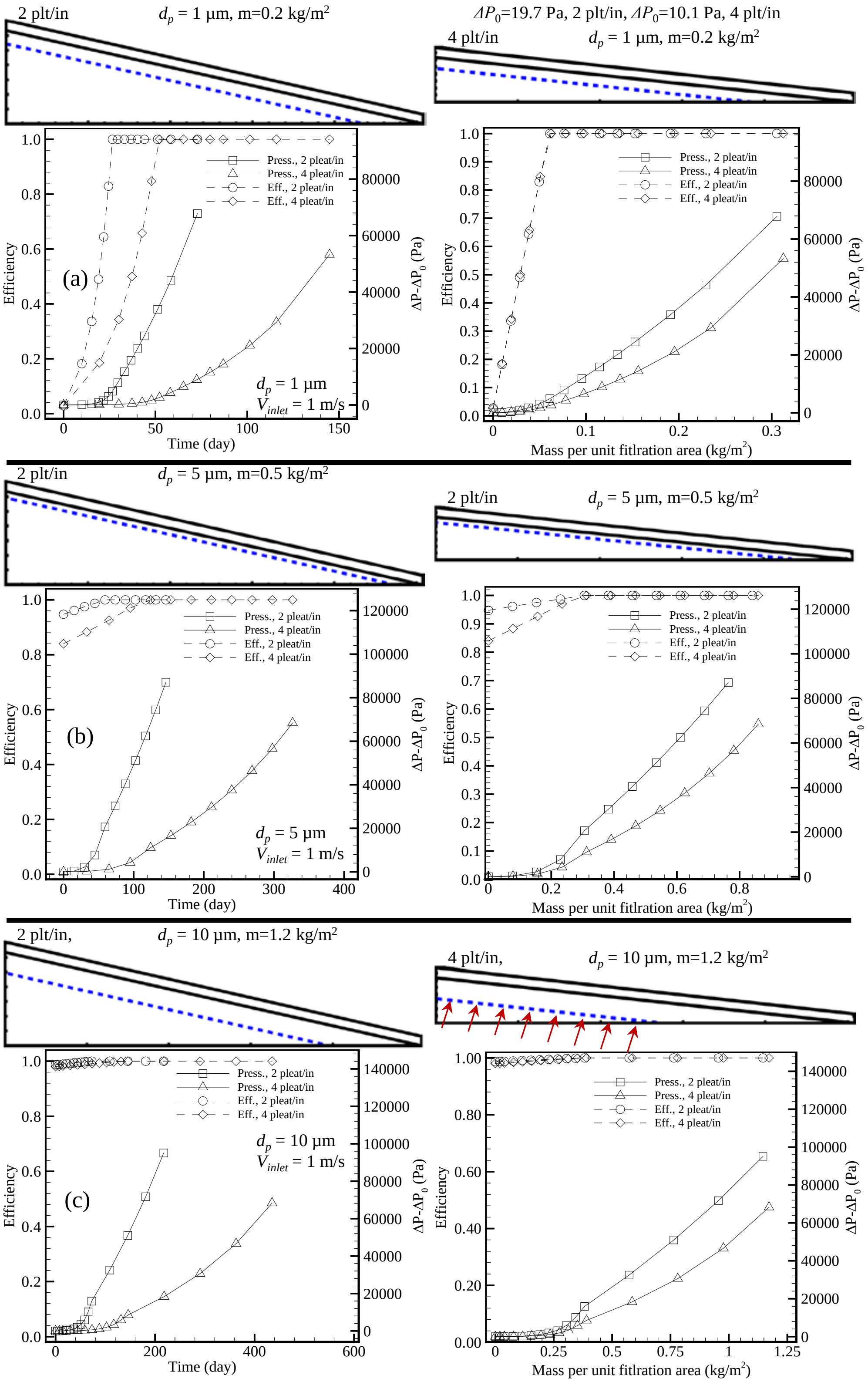

Fig. 5.15: The evolution of collection efficiency and pressure drop with time for filters with 2 and 4 triangular pleats at an inlet velocity of 1 m/s as a function of loading time and mass deposited per unit filtration area. Particles with a diameter of 1, 5, and 10 µm are considered in (a), (b), and (c), respectively. Sample dust-cake profiles are given for each case for illustrations. The blue dashed lines show the dust-cake in the present model.

5.7. Chapter Conclusions

This chapter presents a simple semi-numerical model to predict the instantaneous performance of rectangular and triangular pleated filters under dust loading. The model is developed on the basis of detailed information obtained from our more accurate and realistic, but yet computationally-expensive, CFD simulations on how air and particles behave inside the channels of a pleated filter. The analytical nature of the formulations developed in this work allows one to circumvent the need for solving partial differential equations, and therefore presents an attractive alternative to the CPU-extensive CFD calculations needed to predict the service life of a pleated filter. In our model, we used analytical expressions for the x and y components of the velocity field inside rectangular and triangular channels. The dust-cake pattern and its growth rate are determined by tracking the trajectory of the particles inside the pleat channel. Utilizing the conservation of mass and Darcy's law, we then obtain instantaneous pressure drop and collection efficiency estimates for pleated filters in presence of dust-loading in both depth and surface filtration regimes.

We observed reasonable agreement between the results of our semi-numerical model formulations and those of previously-developed macroscale CFD simulations especially for the case of triangular pleats where premature clogging of the channel is not common—our formulations are not accurate in predicting premature clogging that sometimes occurs in filters with high pleat counts. For model demonstration, a parameter study was conducted for filters with different pleat counts having rectangular and triangular shapes loaded with particles of 1, 5, and 10 µm in diameter. The effects of pleat shape and pleat count on instantaneous pressure drop and collection efficiency is quantified and discussed in detail. For instance, it is shown that filters with rectangular pleats can potentially provide better performance than their triangular counterparts under heavy loading.

Despite the approximate nature of its predictions, the speed by which a large parameter study can be completed makes the present model developed in this work very practical for design and development of pleated filters. One can start a design process with our semi-numerical method to narrow down the design variables and then continue with a more comprehensive CFD model for finalizing the design.

Chapter 6

Semi-Numerical Model for Circular Pleated Filters[8]

6.1. Introduction

Aerosol filters are often pleated into triangular or rectangular patterns and the resulting geometries are often rolled up into a circular shape to accommodate as much filtration media as possible in a confined space (see Figure 6.1a). Obviously, the inlet and outlet diameters of the pleats depend on the dimensions of the casing in which the circular cartridge will be used. Despite the widespread use of pleated filters, the effects of dust deposition and cake formation on the performance of such filters have only been reported in a very few studies (e.g., the computational studies in Rebai *et al.*, 2010; Fotovati *et al.*, 2011; Fotovati *et al.*, 2012; Saleh *et al.*, 2014a; Saleh *et al.*, 2014b or the experimental work in Lo *et al.*, 2010; Park *et al.*, 2012; Bemer *et al.*, 2012; Joubert *et al.*, 2010; Hasolli *et al.*, 2013). As such, no study has yet been reported to establish a link between the radial geometry of a circular pleated filter and its filtration performance (collection efficiency and pressure drop) when loaded with dust particles. This chapter is therefore devised to study the effects of geometric parameters on the filtration

---

[8] Contents of this chapter is submitted for publication and may appear as:
A.M. Saleh, H.V. Tafreshi, B. Pourdehimi, Service Life of Circular Pleated Filters vs. their Flat Counterpart, Submitted for publication, *Separation and Purification Technology*

performance of circular pleated filters over time. From the basic principles of fluid dynamics, one expects the flow field inside a circular pleat to be different from that of a flat pleat (flow into a sink versus a uniform flow). Therefore, the current work is particularly focused on the differences between the performance of a circular pleated filter and its flat counterpart (see Figure 6.1b), as pleated fibrous media are often tested in a flat configuration. The present study builds on the in-depth knowledge obtained from our previous computational fluid dynamics (CFD) simulations of dust-cake growth inside pleated filter media in a flat configuration (Fotovati *et al.*, 2011; Fotovati *et al.*, 2012; Saleh *et al.*, 2014a). However, in contrast to such CFD simulations, the approximate model presented in this chapter allows one to simulate the entire lifecycle of a filter in a few minutes.

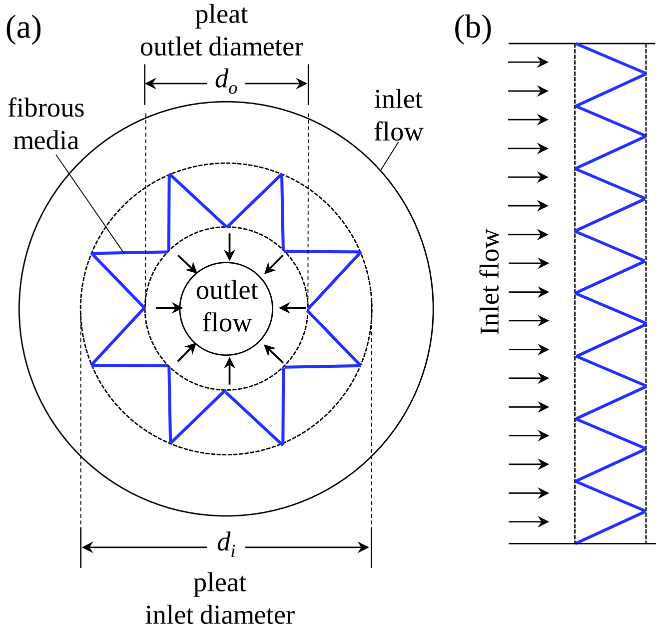

Figure 6.1: Circular pleated filter (a); flat pleated filter (b).

In the remainder of this chapter, we first present our formulations for predicting the pressure drop and collection efficiency of circular pleated filters with and without dust-cake (Sec. 6.2). In Sec. 6.3, we compare the predictions of our model to those obtained from more accurate CFD simulations. Our results and discussion are given in Sec. 6.4 followed by our conclusions in Sec. 6.5.

6.2. Modeling Circular pleated Filters

6.2.1 Clean Fitters

Assuming filter media to be the sole source of pressure drop in a pleated filter, the face velocity (air velocity normal to the media) can be obtained using Darcy's law:

$$v_w = \frac{\Delta p}{t_m}\frac{k}{\mu} \tag{6.1}$$

where Δp is the pressure drop across the media, k is the permeability of the media, t_m is the thickness of the fibrous media, and μ is the air viscosity. Considering a control volume inside the pleat channel, the conservation of mass can be used to develop a relationship between the face velocity v_w and the inlet velocity U_i,

$$U_i\, s_i = v_w w \tag{6.2}$$

where s_i is the arc length at the inlet, and w is the length of the pleat's fibrous wall, as shown in Figure 6.2a.

On the basis our CFD observations of the velocity field inside a pleat channel (see the next section), the face velocity over w is assumed to be constant in our formulation. The average radial velocity $\overline{v_r}(r)$ can also be obtained using the conservation of mass,

$$\overline{v_r}(r)s(r) = U_i s_i - v_w\left(w - \frac{r\sin\theta_{max}(r)}{\sin\gamma}\right) \tag{6.3}$$

where $s(r)$ is the arc length at any radius $r_o < r < r_i$, $\theta_{max}(r)$ is the angle of the pleat channel at a radius r (measured from the center of the pleat), and γ is the pleat's half-angle.

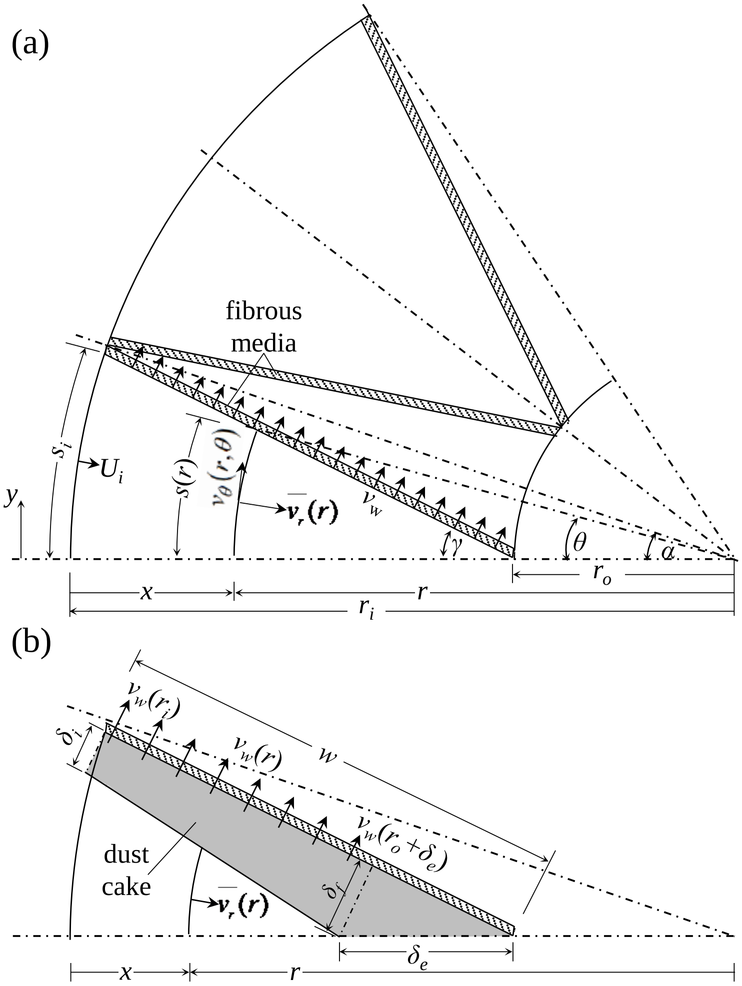

Figure 6.2: Computational domain for a clean circular pleat (a) and a circular pleat accommodating a dust-cake (b).

The flow velocity components in the *x* and *y* directions can then be obtained as,

$$u(x,y) = v_r(r,\theta)\cos\theta + v_\theta(r,\theta)\sin\theta \tag{6.4}$$

$$v(x,y) = v_\theta(r,\theta)\cos\theta - v_r(r,\theta)\sin\theta \tag{6.5}$$

These velocities are then used in the particle equation of motion, Equations 6.6 and 6.7, with $x(t=0)=0$, $y_p(t=0)=y_p^i$, $\frac{dx_p}{dt}(t=0)=u_p^i$, and $\frac{dy_p}{dt}(t=0)=v_p^i$ as the initial conditions, to obtain the instantaneous position and velocity of the particles in the pleat channel.

$$\frac{d^2x_p}{dt^2} + \frac{1}{\tau}\frac{dx_p}{dt} = \frac{1}{\tau}u(x,y) \tag{6.6}$$

$$\frac{d^2 y_p}{dt^2} + \frac{1}{\tau}\frac{dy_p}{dt} = \frac{1}{\tau} v(x, y) \tag{6.7}$$

In these differential equations, $\tau = d_p^2 \rho_p c^c \mu^{-1} / 18$ is the particle relaxation time.

6.2.2 Dust-Loaded Filters: Surface Filtration

Our CFD simulations of particle deposition in triangular pleat channels have revealed that dust-cake tends to grow uniformly over the length of the media regardless of the filter's pleat density (Fotovati *et al.*, 2011; Fotovati *et al.*, 2012; Saleh *et al.*, 2014a). Similar simulations conducted for circular pleated filters, on the other hand, indicate that dust particles tend to deposit somewhat deeper into the pleat channel especially when the filter's inlet-to-outlet diameter ratio $R_{io} = r_i / r_o$ increases (see the next section). Therefore, we considered a linear growth profile for the thickness of dust-cake on fibrous walls of the pleat channel. As shown in Figure 6.2b, the thickness of the cake normal to the pleat wall is assumed to vary linearly from δ_i at the channel entrance to δ_f where the cake reaches the channel's symmetry line. With this assumption, the face velocity varies linearly from $v_w(r_i)$ to $v_w(r_o + \delta_e)$. The face velocity can be calculated as,

$$\Delta p = v_w(r_i)\beta_i = v_w(r_o + \delta_e)\beta_f \tag{6.8}$$

where $\beta_i = \frac{\mu t_m}{k} + \frac{\mu \delta_i}{k_c}$, and $\beta_f = \frac{\mu t_m}{k} + \frac{\mu \delta_f}{k_c}$ are the resistances against the air flow. The cake permeability k_c can be obtained from the Kozeny–Carman equation (Carman, 1956),

$$k_c = \frac{d_p^2 c^c}{180} \frac{\varepsilon^3}{(1-\varepsilon)^2} \tag{6.9}$$

with the cake porosity ε obtained from an empirical correlation proposed in the work of Kasper *et al.*, 2010],

$$\varepsilon = 0.36 + 0.64\exp\left(-0.29\frac{\rho_p}{\rho_w}d_p\right) \tag{6.10}$$

Considering the conservation of mass for the air in a dust-loaded pleat (see Figure 6.2b), we obtain,

$$U_i s_i = \frac{1}{2}\left(w - \delta_e\, cos\,\gamma\right)\left(v_w(r_i) + v_w(r_o + \delta_e)\right) \tag{6.11}$$

Solving Equations 6.8 and 6.11, we can obtain an expression for the filtration velocity across the length of the pleat wall $v_w\left(r\right)$,

$$v_w(r) = v_w(r_i) - \left(v_w(r_i) - v_w(r_o + \delta_e)\right)\frac{r - \left(r_o + \delta_e\right)}{r_i - \left(r_o + \delta_e\right)} \tag{6.12}$$

Similar to the case of clean pleats, the average radial velocity at any cross-section inside the pleat channel can be obtained as,

$$\overline{v_r}(r) = \frac{1}{s(r)}\left[U_i s_i - \frac{1}{2}\left(v_w(r_i) + v_w(r)\right)\left(w - \frac{r\,sin\theta}{sin\gamma}\right)\right] \tag{6.13}$$

In order to obtain both the tangential and radial velocity distributions at any point inside the pleat channel, we conducted a series of CFD simulations for circular pleated filters with different pleat angles. The fibrous media considered in these calculations were assumed to be 2 mm thick with an SVF of 7.5%, and a fiber diameter of 15 µm. Our CFD simulations were conducted using ANSYS–Fluent code enhanced with a series of in-house subroutines (Fotovati *et al.*, 2011; Fotovati *et al.*, 2012; Saleh *et al.*, 2014a). Figure 6.3a shows the computational domain and the boundary conditions used in the CFD calculations (due to symmetry, only a half-pleat was simulated). Figure 6.3b shows examples of velocity field inside pleat channels with different inlet-to-outlet diameter ratios for illustration purposes. For these simulations, two arbitrary inlet radii of 76.2 and 152.4 mm were considered along with a varying outlet radius to obtain pleat channels with different pleat angles. Figures 6.3c and 6.3d show the normalized radial and tangential channel velocities at different normalized radii $r^* = (r_i - r)/(r_i - r_o)$ versus tangential normalized angle θ / θ_{max} for pleats with different inlet-to-outlet diameter ratios. The data included in these figures include pleat geometries with inlet radii of 76.2 and 152.4 mm having three different pleat angles of 20, 30, and 45°. These radial and tangential velocity components are normalized using the average radial velocity $\overline{v}(r)$ and the tangential velocity at the pleat fibrous wall $v_\theta(r, \theta_{max})$, respectively (see Figures 6.3e and 6.3d).

It can be seen in Figure 6.3c that the normalized radial velocity is independent of the angle θ except for when θ approaches θ_{max} (at the surface of the fibrous media) where it sharply decreases by about 20–40%. This trend has consistently been observed for all the pleat geometries considered in our study, and we have therefore assumed a uniform radial velocity at any radius:

$$v_r(r, \theta) = \overline{v_r}(r) \tag{6.14}$$

Note that the decrease in the radial velocity takes place in an area very close to the surface of the fibrous media, where particles can no longer remain airborne (they become intercepted by the pleat fibrous walls). Therefore, the assumption of uniform radial velocity does not impact the accuracy of our particle trajectory calculations. The permeability of the fibrous media was also varied in order to study its effect on the velocity profile inside the pleat channel.

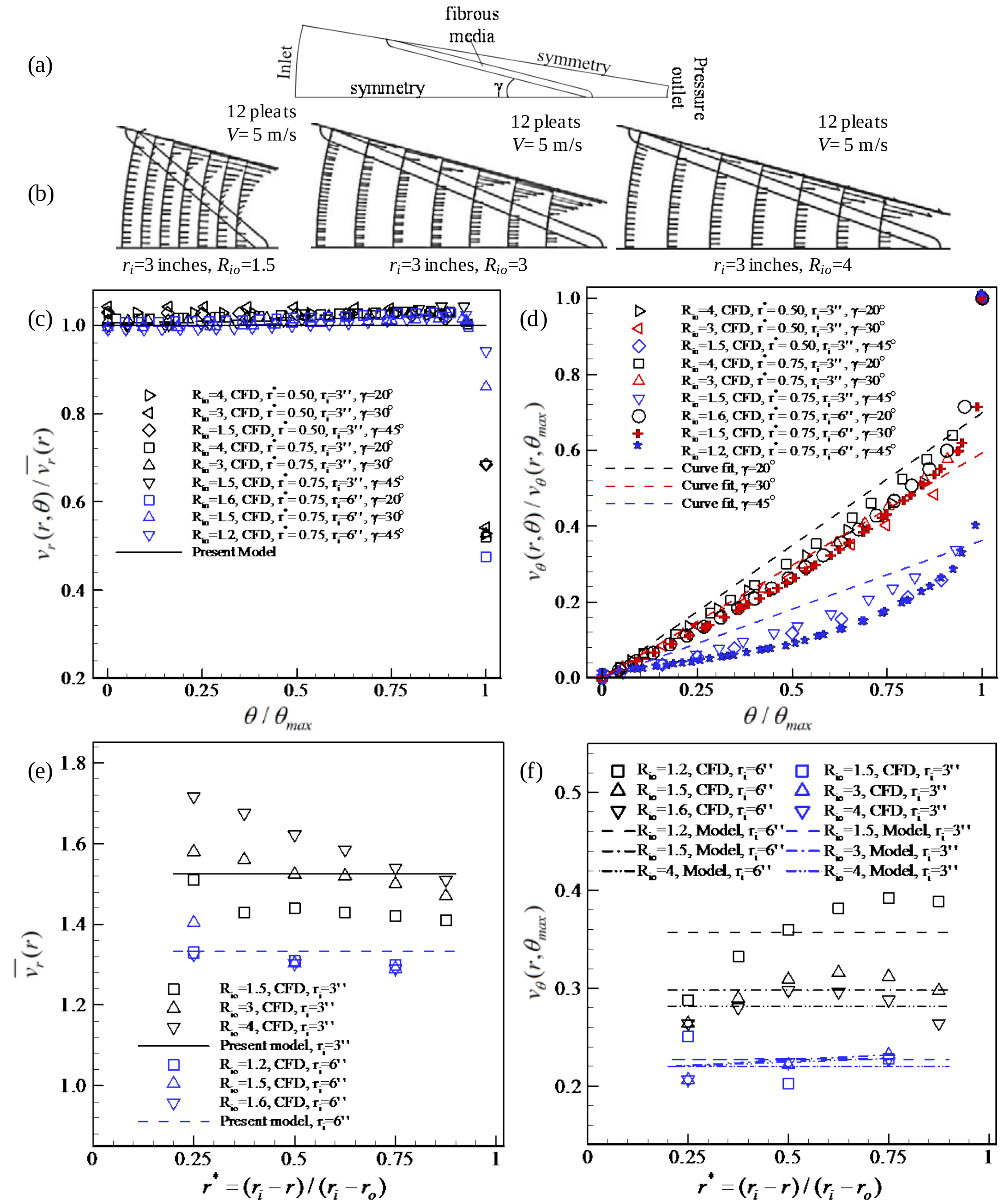

Figure 6.3: Computational domain used in CFD simulations is shown in (a). Velocity field obtained from CFD simulations for 12-pleat circular filters having a fixed inlet diameter of 152.4 mm but different outlet diameters are shown in (b). The radial and tangential components of the velocity field are obtained from our CFD calculations for pleated circular filters and are shown in (c) and (d). Average radial velocity and maximum tangential velocity are shown in (e) and (f) respectively.

It was observed that face velocity remains uniform along the length of the pleat walls except for when an unrealistically high permeability was considered for the fibrous media (e.g., greater than 5.4×10^{-10} m^2 for the geometry considered here). In that case, the face velocity was observed (not shown here for the sake of brevity) to increase slightly near the pleat end. Our results also showed that the tangential velocity inside the pleat channel can be best approximated with a linear profile and does not depend on the inlet diameter or the pleat count, as long as the pleat angle is fixed. The normalized tangential velocity inside the pleat channels (shown with open symbols in Figure 6.3d) was found to depend only on the pleat half angle γ. We therefore produced an expression for the flow angular velocity through curve fitting for $20^o < \gamma < 45^o$:

$$v_\theta(r,\theta) = \chi(\theta / \theta_{max}) v_\theta(r,\theta_{max}) \tag{6.15}$$

In this equation, $\chi = 1 - 0.9845\gamma + 0.2181\gamma^2$, and the angle γ is in radian. It is important to mention that the normalized tangential velocity was found to be independent of the pleat inlet diameter or the inlet-to-outlet diameter ratio R_{io}. However, the values of the maximum tangential velocities $v_\theta(r,\theta_{max})$ are different for each case as shown in Figure 6.3f. It is expected that $v_\theta(r,\theta_{max})$ increases with the increase of the angle γ as the pleat wall length decreases resulting from the increase in the filtration velocity. More importantly, the angles from which the normalized velocities are measured differ with changing the inlet diameters. Filters with smaller inlet diameters will cause stronger radial air flow toward the center point. But with higher inlet diameter (or R_{io} values close to 1), the center point is far from the pleat and the radial flow is not as strong as pleats with smaller inlet diameter. Having the velocity field inside the pleat calculated, one can obtain the trajectory of a particle traveling inside a pleat channel and predict the collection efficiency of the filter by solving Equations 6.6 and 6.7 using the velocity field given in Equations 6.14 and 6.15.

Figure 6.4a demonstrates how the pleat angle can influence the trajectory of particles in the pleat channel using particles with a diameter of 10 µm as an example. Looking closely at the particle deposition sites in Figure 6.4a, one can notice that decreasing the pleat angle forces the particles to deposit deeper into the pleat channel, forming a non-uniform cake profile (note that pleat angle increases when increasing the inlet diameter but keeping the length of the pleat wall w constant). Interestingly, circular pleated filters with $R_{io} \cong 1$ experience uniform particle deposition, and their performance tend to become similar to that of flat pleated filters (this was also observed in simulations conducted for circular filters with different pleat counts, but the results are not shown for the sake of brevity). Figure 6.4b shows the effects of varying R_{io} for a 12-pleat circular filter having a constant inlet diameter but varying pleat wall lengths w at a constant air flow rate. It can be seen that, the inlet-to-outlet diameter ratio R_{io} plays a major role in particle deposition profile: increasing R_{io}, while the inlet diameter is kept constant, forces the particles to deposit deeper into the pleat channel. Note that, particle position sites determine the slope of the cake profile. More specifically, the ratio of the number of particles deposited on the first half of the channel's wall to that deposited on the second half is taken here as the ratio of the cake thickness at the middle point of the pleat wall to that when the cake comes into contact with the channel's centerline $\left(\delta_i + \delta_f\right) / 2\delta_f$.

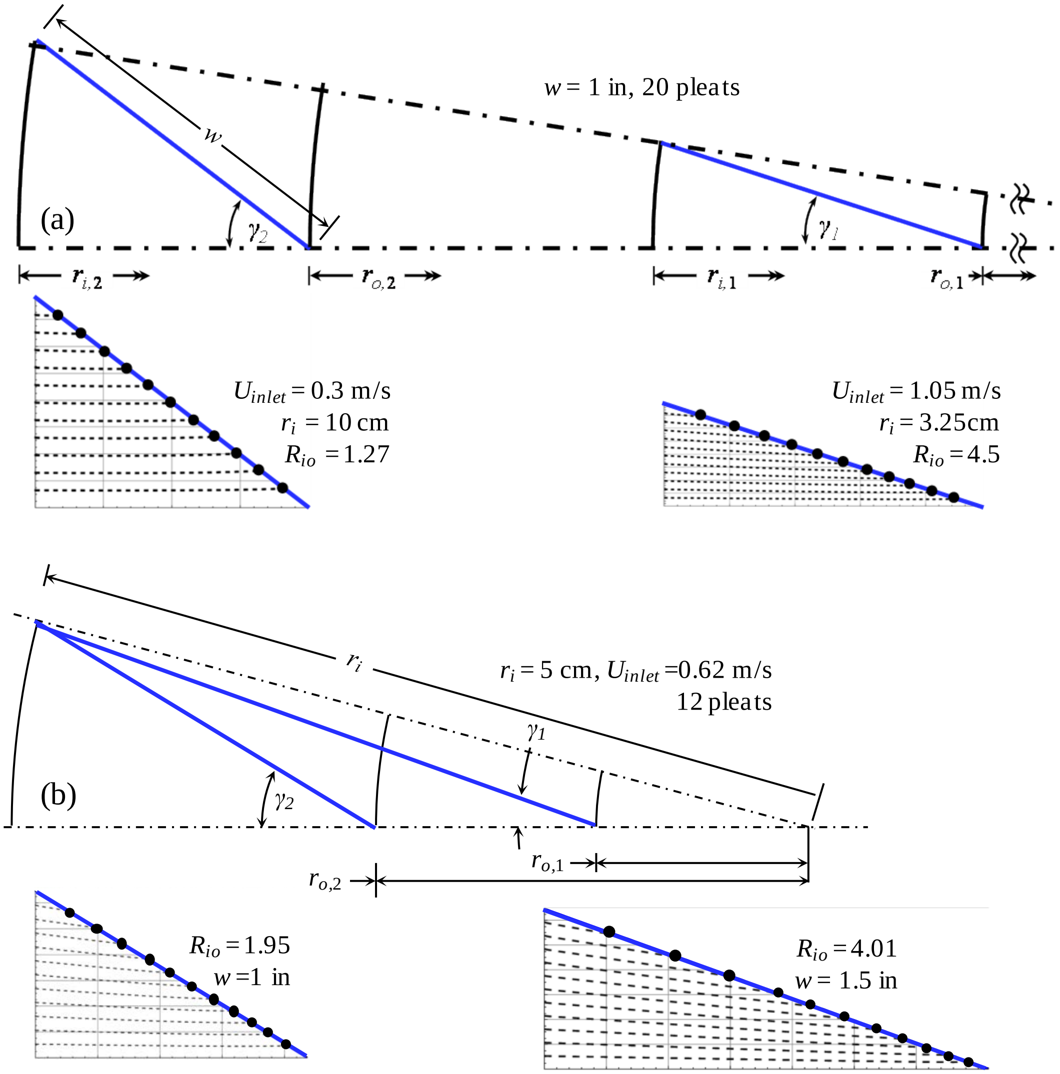

Figure 6.4: Effects of pleats' inlet-to-outlet diameter ratio on particle trajectory for circular pleated filters having the same pleat wall length (a), or having the same inlet diameter (b). The air flow rate is the same in both cases.

6.2.3 Dust-Loaded Filters: Depth and Surface Filtration

In the case of depth filters, our model calculates the filter's initial performance using the cell model equations (the equations are not presented here for the sake of brevity but they can be found in Chapter 5). Our model assumes that the efficiency of a filter changes linearly from its clean efficiency to 100%, as particles continue to deposit in the filter causing the media's SVF increase from its clean value to the maximum value defined by Equation 6.10. For pressure drop calculations, we use the un-weighted resistivity method of the work of Mattern and Deen, 2008.

In this method, the resistance of the loaded media is assumed to be the summation of both the resistance of the clean fibrous medium and that of the particle-loaded media:

$$\beta_l = \beta_m + \beta_p = \frac{\mu t_m}{k(\phi_m)} + \frac{\mu t_m}{k_c(\phi_p)} \tag{6.16}$$

where β_l, β_m, and β_p are the resistance of particle-loaded media, clean media, and the particles deposited within the media; ϕ_m and ϕ_p are the solid volume fraction of the fibrous and particles deposited in the media, respectively.

6.3. Comparison with CFD Simulations

In this section, we compare the predictions of our semi-numerical model with the more accurate predictions of our macroscale CFD simulations (for more information about the accuracy of these CFD simulations see Fotovati *et al.*, 2011; Fotovati *et al.*, 2012; Saleh *et al.*, 2014a). Figures 6.5a and 6.5b show the pressure drop and collection efficiency of a 19-pleat circular filter with an SVF of 7.5%, a thickness of 0.7 mm, and a fiber diameter of 5 µm. The inlet and the outlet diameters are taken to be 85 and 34 mm, respectively, and the inlet volume flow rate is set equal to 0.185m^3/s. Figures 6.5a and 6.5b are obtained for particles with a diameter of 1 and 10 µm, with their corresponding trajectories in Figure 6.5c and 6.5d, respectively. The results shown in Figure 6.5 show that there exists good general agreement (less than 20%) between the predictions of our semi-numerical model and those of the CFD calculations (the mismatch is due to the simplistic nature of the cake growth models considered in our semi-numerical model).

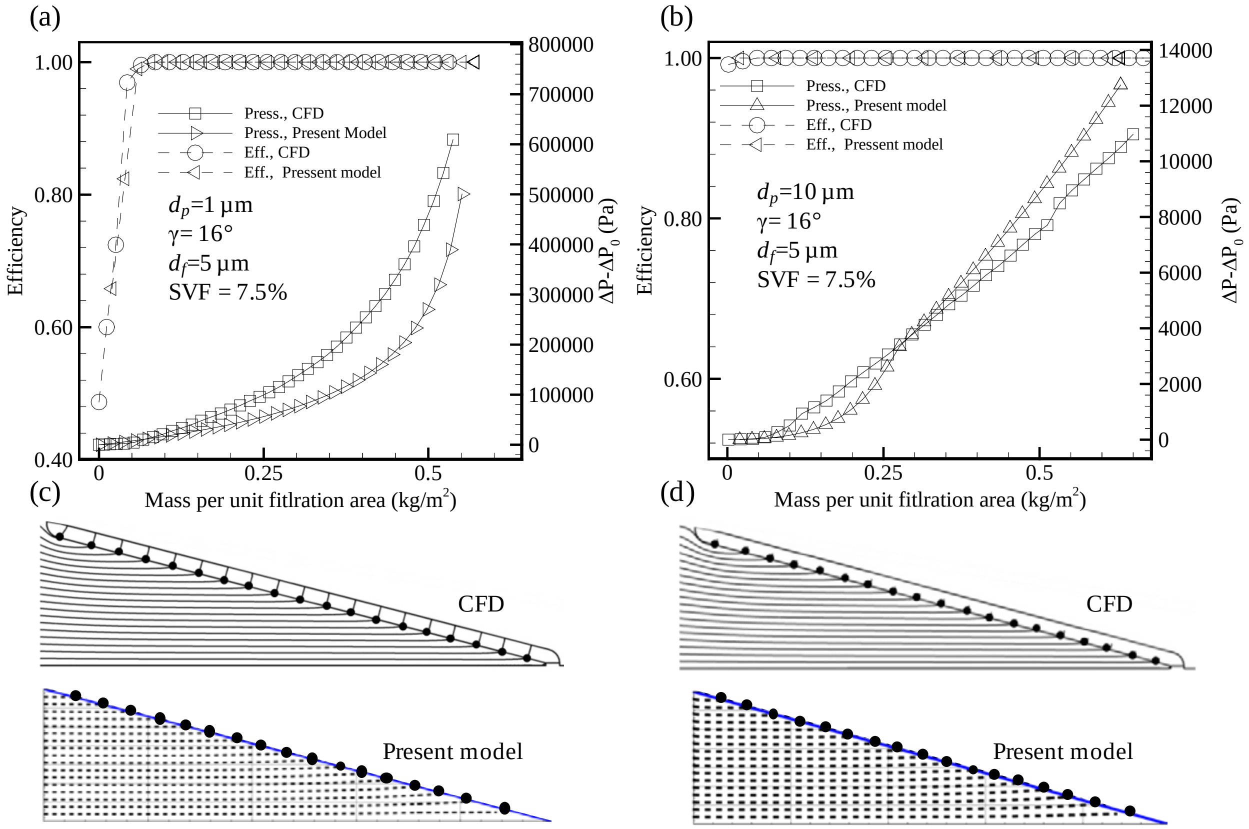

Figure 6.5: Comparison between pressure drop and collection efficiency predictions obtained from the present model and our CFD simulations for a circular pleated filter with 19 pleats loaded with dust particles at an air velocity of 0.5 m/s. The data shown in (a) and (b) are obtained for 1 µm and 10 µm particles, respectively. Particle trajectories from CFD simulations are compared with those of the current model in (c) and (d) for 1 µm and 10 µm particles, respectively.

6.4. Results and Discussion

In this section, we compare the performance of circular pleated filters to their flat counterparts. We arbitrarily chose a fibrous medium made of fibers with a diameter of 15 µm, an SVF of 10%, a thickness of 0.7 mm and a pleat length of 25.4 mm for the cases considered in this section. The flat pleated filters were constructed such that pleat geometries with 2 and 4 pleats per inch and half-pleat angles of 7.125° and 14.25° were obtained. The same pleat angles were also used for the circular filters (see Figure 6.6), but different inlet diameters were used to obtain different inlet-to-outlet diameter ratios.

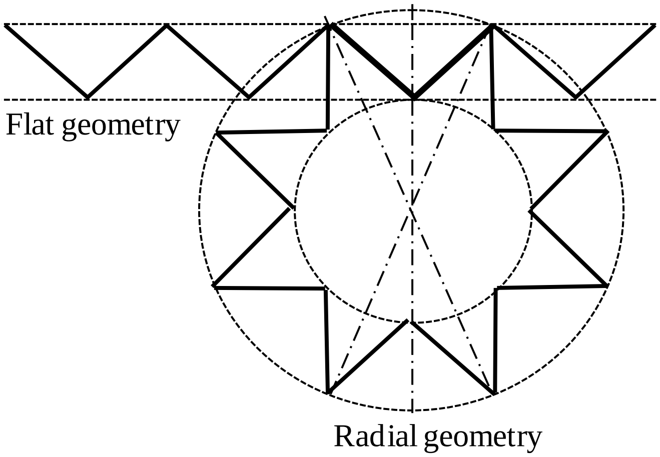

Figure 6.6: Illustration of a circular pleated filter and its flat counterpart.

Figures 6.7a–6.7d show a comparison between the performance of circular pleated filters and their flat counterparts having a half-pleat angle of $\gamma = 7.125^o$ when loaded with mono-dispersed particles of 1 and 10 µm diameters. These circular filters have 28 and 32 pleats, corresponding to inlet radii of 32.4 and 28.4 mm, when considering R_{io} ratios of 4.7 and 10.2, respectively. Figures6.7e–6.7h present similar a comparison but for circular filters having 16 and 14 pleats with corresponding inlet-to-outlet diameter ratios of 4.9 and 11.8 and inlet radii of 32.6 and 28.5 mm, respectively, leading to a half-pleat angle of $\gamma = 14.25^o$. Figures 6.7a, 6.7c, 6.7e, and 6.7g compare dust-cake profiles in circular pleated filters with those in their flat counterparts for particles of 1 or 10 µm diameters at different mass loadings. It is clearly shown in Figures 6.7b and 6.7d that circular pleated filters experience slightly less pressure drop increase due to mass loading when $R_{io} >> 1$. This is because increasing the inlet-to-outlet diameter ratio forces the particles to deposit deeper into the pleat channel, leaving a thin dust-cake near the pleat entrance where the flow can pass through with less resistance. For instance, the circular pleated filter with an inlet-to-outlet diameter ratio $R_{io} = 10$ exhibits 25% less pressure drop than its flat counterpart when loaded with particles of 1 µm at a mass loading of 0.15 kg/m^2 (or 8% at a mass loadings of

0.69 kg/m^2 with 10 µm particles). This effect becomes clearer when the pleat angle is increased. As shown in Figures 6.7f and 6.7h, when the pleat with angle is increased to 14.25°, for instance, the circular pleated filters with $R_{io} = 4.9$ and $R_{io} = 11.8$ show 36% and 62% less pressure drops than their flat counterpart loaded with particles of 1 µm diameter at a mass loading of 0.29 kg/m^2, respectively.

6.5. Conclusions

This chapter presents an easy-to-use approximate model to predict the filtration performance of circular pleated filters under dust loading conditions. Our model starts by considering a reasonable profile for the dust-cake inside a filter's pleat channels, and allows it to grow as the filter accumulates particles over time. Utilizing Darcy's law for pressure drop and Newton's 2nd law for particle trajectory calculation, our model provides quantitative information with regards to the instantaneous performance of a circular pleated filter in both the depth and surface filtration regimes. The predictive model developed in this work is approximate, but given the trade-off between accuracy and speed, the rate at which a large parameter study can be completed makes our model uniquely attractive for design and development of circular filters. One can start a design process with our present method to narrow down the design variables and then continue with a more comprehensive CFD model for finalization of the design.

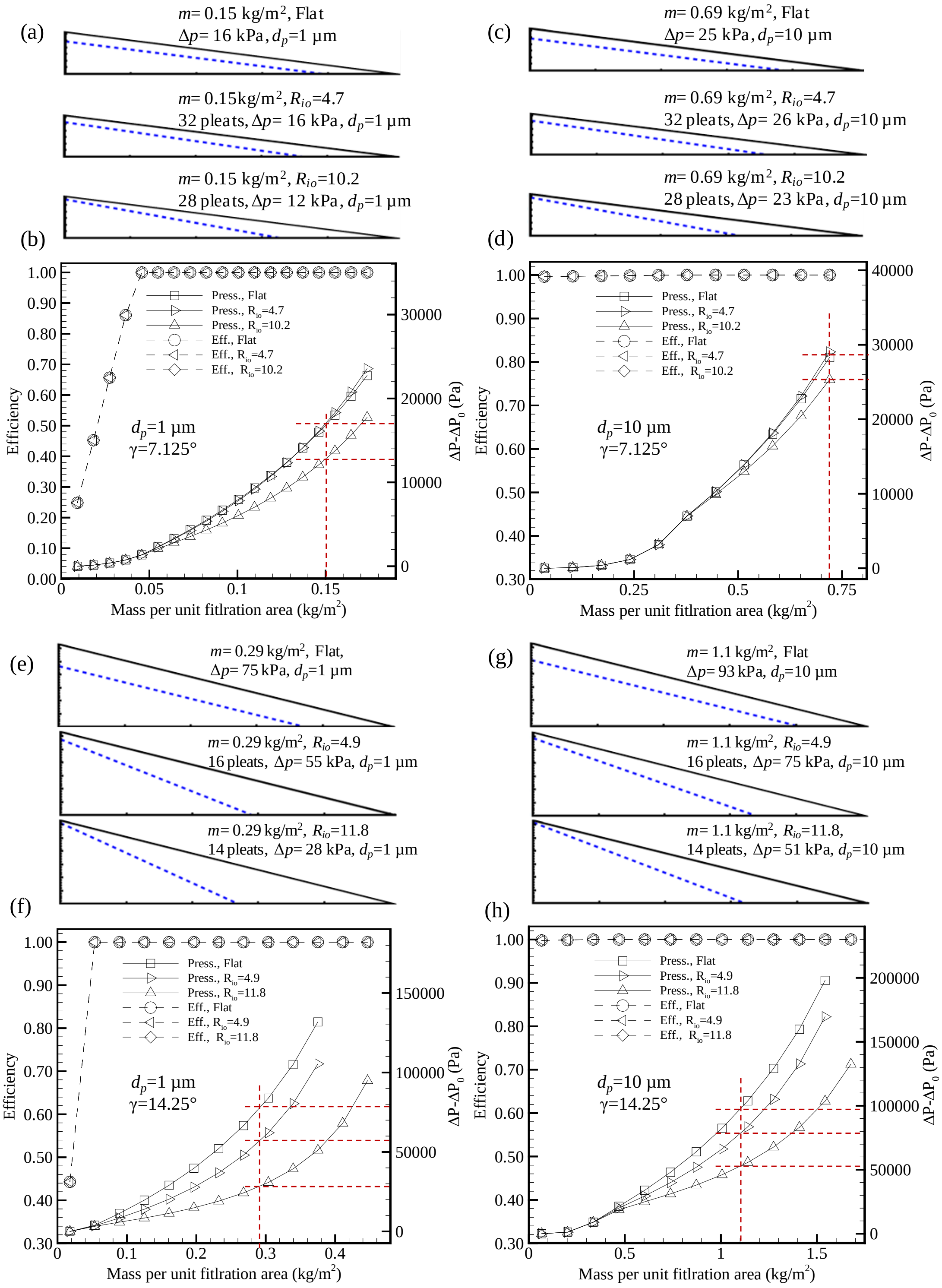

Figure 6.7: Dust-cake profile examples for circular and flat pleated filters of a fixed pleat half angle of $\gamma = 7.125^o$ at an inlet velocity of 1 m/s are shown with blue dashed lines in (a) particles with a diameter of 1 µm. The instantaneous collection efficiency and pressure drop for this filter-particle combination is given in (b) as a function of mass deposited per unit filtration area. The results in (c) and (d) correspond to the same calculations but for particles with a diameter of 10 µm. Likewise, the results in (e), (f), (g), and (h) are obtained for the same circular pleated filter but when the half angle in increased to $\gamma = 14.25^o$.

In this Chapter, in particular, performance of a circular pleated filter is compared to its flat counterpart. It was found that circular pleated filters with high inlet-to-outlet diameter ratios perform better than their flat counterparts. This is because when a filter's inlet-to-outlet diameter ratio is high, the particles tend to deposit deeper into the pleat channel leaving a thin, relatively more permeable, dust-cake near the pleat entrance. Our pressure drop and collection efficiency predictions are also compared with the results of our previously developed more sophisticated CFD simulation methods, and reasonable agreement has been observed.

Chapter 7

Predictive Correlations for Dust-Loaded Pleated Filters[9]

7.1. Introduction

In previous chapters we presented models to predict the performance of dust-loaded pleated filters. However, it is impossible for any numerical or experimental study to consider all the parameters affecting the filtration performance of a pleated filter. It is then very necessary for the industry to develop correlations that estimate the filtration efficiency of a pleated filter in service as a first step of product design and development.

In this chapter, we use analytical derivations as well as our previously developed models to develop correlations that predict the filtration performance of flat rectangular or triangular pleated filters in addition to cylindrical pleated filters made of triangular pleats. These correlations are very helpful in predicting an approximate value of the collection efficiency and pressure drop of a pleated filter during its service as a function of the amount of mass deposited in the filter. Using these correlations will be the first step of the pleat design process before conducting any expensive experimental or numerical experiments.

---

[9] Contents of this chapter is prepared to be submitted for journal publication

In the following subsection, we first present our correlation formulations for depth filtration in triangular pleated filters under dust-loading (Sec. 7.2). We then discuss the formulations describing the pressure drop in the surface filtration regime of flat and cylindrical pleated filters in Sec. 7.3 and Sec. 7.4, respectively. In Sec. 7.5 and Sec. 7.6, we discuss the depth and surface filtration correlations for rectangular filters. We compare the predicted performance of the presented correlations with CFD simulations and with the macroscale model predictions in Section 7.7, followed by our conclusions are given in Sec. 7.8.

7.2. Depth Filtration in Triangular Pleats

Assuming filter media to be the sole source of pressure drop in a pleated filter, the pressure drop of a clean filter can be obtained using Darcy's law:

$$\Delta p_0 = v_w \frac{\mu}{k_m} t_m = v_w \beta_0 \tag{7.1}$$

where Δp and v_w are the pressure drop and the filtration velocity across the fibrous media, respectively, k_m is the permeability of the media, t_m is the thickness of the fibrous media, β_0 is the resistance of the clean fibrous medium, and μ is the air viscosity. When particles deposit inside the media, they cause additional resistance to the flow which increases the pressure drop. The pressure drop of a loaded medium can be obtained as

$$\Delta p = v_w \beta_l \tag{7.2}$$

where β_l is the dust-loaded media resistance. Using the un-weighted resistivity method, the following expression can be used for the total dust-loaded resistance:

$$\beta_l = \beta_m + \beta_p = \frac{\mu t_m}{k_m(\phi_m)} + \frac{\mu t_m}{k_c(\phi_p)} \tag{7.3}$$

where ϕ_m and ϕ_p are the solid volume fraction of the clean fibrous medium and particles deposited in the medium, respectively. k_c is the permeability of the granular media due to particle deposition and can be obtained from:

$$k_c = \frac{d_p^2 c^c}{180}\frac{(1-\phi_p)^3}{\phi_p^2} \tag{7.4}$$

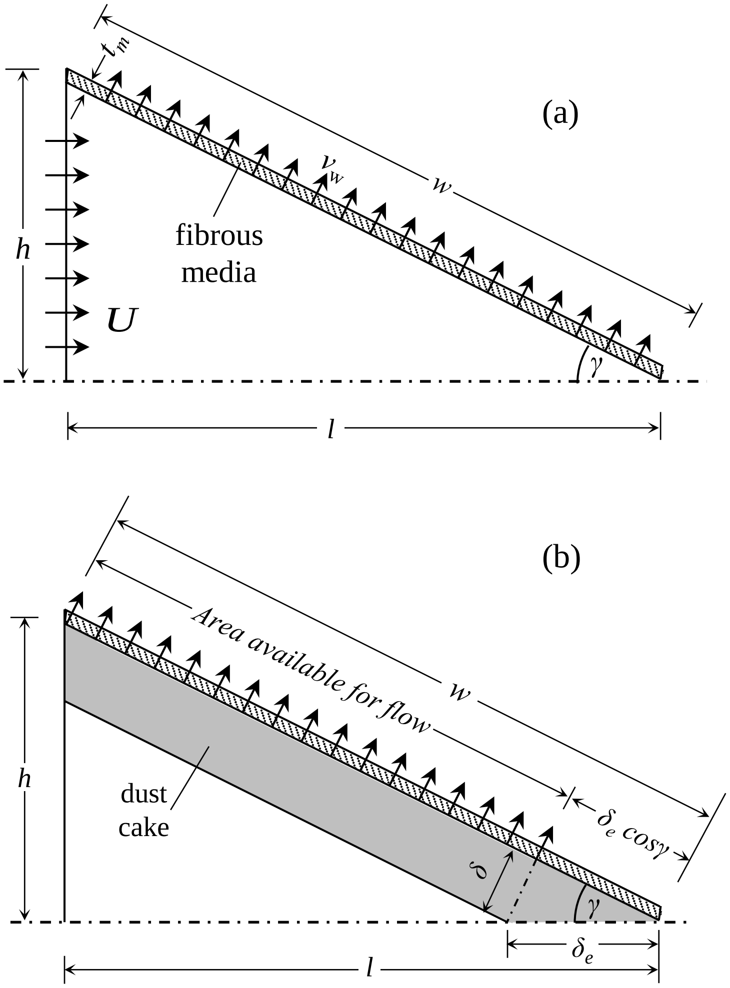

Fig. 7.1: Illustration of dust loaded triangular flat pleated filter with depth (a) and surface (b) deposition.

Rearranging Equation 7.2, the following expression for the pressure drop increase due to particle deposition can be obtained as

Using Equation 7.2, the following expression for the pressure drop increase due to particle deposition can be obtained

$$\Delta p_p = v_w \mu \frac{t_m}{k_c(\varphi_p)} \tag{7.5}$$

where Δp_p is the pressure drop increase due to deposition inside the fibrous media. In order to relate the filtration velocity across the fibrous media to the inlet velocity, we applied mass conservation on a control volume including the pleat channel as shown in Figure 7.1a. Therefore, we obtain

$$w v_w = hU \tag{7.6}$$

where w is the filtration area per unit pleat depth and h is the pleat height (see Figure 7.1a). The depth of the pleat is the direction normal to the paper. By definition, volume fraction of deposited particles φ_p can be written as

$$\varphi_p = \frac{n_p V_p}{V_m} \tag{7.7a}$$

in which n_p is the number of particles deposited inside the media, V_p is the volume of one particle, and V_m is the volume of the fibrous media, and $m_p = \rho_p n_p V_p$ is the total mass of the deposited particles. Therefore, Equation 7.7a can be written as:

$$\varphi_p = \frac{m_p}{\rho_p V_m} \tag{7.7b}$$

in which ρ_p is the density of the particle material. Equation 7.5 can therefore be written as:

$$\Delta p_p = \frac{Uh\mu}{w}\left(\frac{t_m}{k_c}\right) = \frac{Uh\mu t_m}{w}\frac{180}{d_p^2 c^c}\left(\frac{m_p}{\rho_p V_m}\right)^2\left(1-\frac{m_p}{\rho_p V_m}\right)^{-3} \tag{7.8}$$

The above equation gives the pressure drop increase in the depth filtration regime, and is valid as long as

$$0 \le m_p \le \rho_p V_m \left(\alpha_p - \varphi_m\right) \tag{7.9a}$$

$$0 \le \varphi_p \le \left(\alpha_p - \varphi_m\right) \tag{7.9b}$$

where φ_m is the SVF of the clean fibrous media. This means that the total volume of the particle granular structure should be less than the volume of the particle pack subtracted from it the volume occupied by the original fibers. Here, we use an empirical correlation for α_p reported by Kasper *et al.,* 2010:

$$\alpha_p = 0.64 - 0.64\exp(-0.29\frac{\rho_p}{\rho_w}d_p) \tag{7.10}$$

where ρ_w is the density of the water. Note that in the case of $\alpha_p \le \phi_m$, there is no depth filtration, as particles have no space to be deposited inside the filter medium besides the fibers and hence, particles will start depositing on the surface immediately.

For the collection efficiency prediction, we can use the well-known Single Fiber Efficiencies (SFEs) from literature to estimate the initial efficiency of the pleated filter. Here, we use the expression of (Stechkina *et al.*, 1982) for SFE due to Brownian diffusion,

$$E_D = 2.9Ku^{-1/3}\,\mathrm{Pe}^{-2/3} + 0.62\mathrm{Pe}^{-1} \tag{7.11}$$

where $Ku = -\frac{\ln \varphi_m}{2} - 0.75 + \varphi_m - 0.25\varphi_m^2$ is the Kuwabara factor, $\mathrm{Pe} = v_w d_f / D$ is the Peclet number $D = \sigma c^c T / (3\pi \mu d_P)$ is particle diffusivity, and $\sigma = 1.38 \times 10^{-23} (m^2 kg s^{-2} K^{-1})$ is the Boltzmann constant. The SFE due to interception is calculated using the expression proposed in (Lee and Liu, 1982):

$$E_R = 0.6 \frac{1-\varphi_m}{Ku} \frac{R^2}{(1+R)} \tag{7.12}$$

The SFE due to impaction is obtained using the equation of the study by Landahl and Hemann, 1949:

$$E_I = \frac{\mathrm{St}^3}{\mathrm{St}^3 + 0.77\mathrm{St}^2 + 0.22} \tag{7.13}$$

where $St = \frac{\rho_p d_P^2 c^c v_w}{18 \mu d_f}$ is Stokes number and calculated based on the filtration velocity inside the fibrous media (not the inlet velocity). The total collection efficiency of the clean pleated filter can then be obtained using the following equation (Brown, 1993),

$$E_0 = 1 - \exp\left(\frac{-4\varphi_m E_\Sigma t_m}{\pi d_f (1-\varphi_m)} \right) \tag{7.14}$$

where $E_\Sigma = 1 - (1-E_D)(1-E_R)(1-E_I)$ is the total SFE.

The above equations are developed for clean filters. Our object however is to model the collection efficiency of particle-loaded filters. We assumed that the deposition of particles inside a fibrous structure only affects its SVF. The loaded particles increase the SVF of the filter and hence its collection efficiency. For the sake of simplicity, we assume that the filtration efficiency of a fibrous structure increases linearly with the mass of the particles deposited within the structure. We assume collection efficiency of the filter reaches 100% when the SVF of the particles within the fibrous media reaches a maximum value φ_p^{max}. The instantaneous efficiency of the filter for SVFs smaller than the maximum allowable value is estimated via linear interpolation between the clean efficiency, at the SVF of the media (φ_m), and 100%, at the maximum SVF (φ_p^{max}). Therefore, the efficiency of a loaded filter holding mass m_p can be predicted as:

$$E_m = E_0 + (1 - E_0)\frac{m_p}{m_p^{max}} \tag{7.15}$$

where E_m is the efficiency of dust-loaded pleated filter and m_p^{max} is the maximum mass that can fill the fibrous media.

$$m_p^{max} = \varphi_p^{max} \rho_p V_m \tag{7.16}$$

$$\varphi_p^{max} = \alpha_p - \varphi_m \tag{7.17}$$

7.3. Triangular Flat Pleats with Surface Filtration

Applying Darcy’s Law to obtain the pressure drop due to surface dust deposition (Δp_s) in a pleated filter,

$$\Delta p_s = v_w \frac{\mu}{k_c}\delta = v_w \beta_c \tag{7.18}$$

where β_c is the resistance of the dust granular media to the air flow. The thickness of the cake δ can be expressed in terms of mass deposition,

$$m_p = \rho_p V_c \alpha_p = \rho_p A_f \delta \alpha_p \tag{7.19}$$

where V_c is the volume of the particle granular pack and A_f is the filtration surface area and is equal to the product of the length (w) and the depth (z) of the pleat wall.

Hence, pressure drop can be approximated in the following expressions:

$$\Delta p_s \approx v_w \frac{\mu}{k_c} \frac{m}{\rho_p \alpha_p A_f} \tag{7.20}$$

It can be seen from the above equation that the pressure drop is inversely proportional to the dust cake permeability k_c, the surface area available for filtration ($w - \delta_e \cos\gamma$), and the cake solid volume fraction α_p. It is also linearly proportional to the inlet velocity U as shown in Fig. 7.1b. Hence we have:

$$\Delta p_s \propto U, \frac{1}{k_c}, \frac{1}{\alpha_p}, \frac{1}{w - \delta_e \cos\gamma} \tag{7.21}$$

where δ_e is the dust cake thickness measured from the pleat end, and γ is the pleat half angle. Therefore we can obtain an expression for the pressure drop increase due to surface deposition as

$$\Delta p_s = \psi \frac{m}{A_f} U \frac{1}{\alpha_p k_c \left(w - \delta_e \cos\gamma \right)} \tag{7.22}$$

where ψ is a constant of proportionality.

The cake thickness at the end of the pleat can be related to the mass deposited as

$$\delta_e = \frac{w\left(1 - \sqrt{1 - \dfrac{2m}{w^2 \rho \alpha_p} \cot\gamma}\right)}{\cos\gamma} \tag{7.23}$$

Substituting in the pressure drop equation (Eq. 7.22) we can obtain

$$\Delta p_s = \psi \frac{m_p}{A_f}\frac{U}{\alpha_p k_c w}\left[1-\left(1-\left(1-2\frac{m}{w^2\rho_p\alpha_p}\cot\gamma\right)^{0.5}\right)\right]^{-1} \tag{7.24}$$

It is shown in the above equation that the pressure drop is not a linear function of mass per unit area. In order to linearize the relation we divided the increase in pressure drop by $\frac{U}{\alpha_p k_c w}\left\{1-\left(1-(1-2\frac{m_p}{w^2\rho_p\alpha_p}\cot\gamma)^{0.5}\right)\right\}^{-1}$. Hence, we obtain a linear function of the linearized pressure drop and the mass loaded per unit area m_p / A_f as can be seen in Figure 7.2. The case presented in this figure is for a 2 pleat per inch surface filter with a pleat height and width of 0.635 cm and a pleat angle of 45°. The dashed line shows an exact linear function, and the solid line shows the linearized pressured drop as a function of mass per unit area.

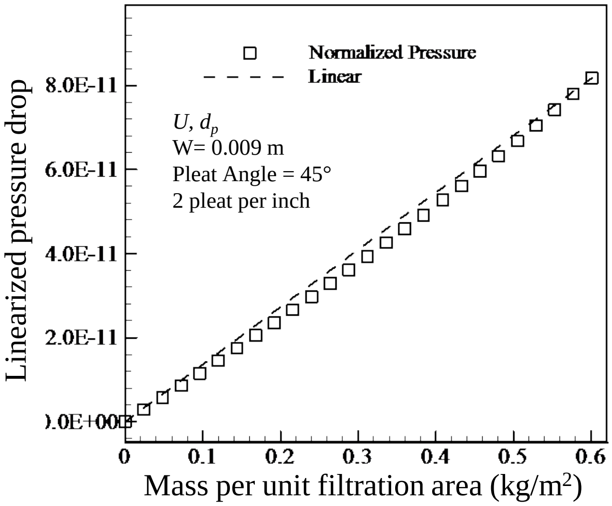

Fig. 7.2: Example of linearized pressure drop as a function of mass per unit area of a surface flat triangular pleated filter. This plot is applicable to any particle diameter and inlet velocity.

The constant of proportionality ψ was found to be only dependent on the pleat geometry. More specifically, it was not a function of the flow velocity or the particle diameter. Values of ψ is plotted in Fig. 7.3. These values were obtained by applying our 2-D semi-numerical model for different pleat lengths and heights in order to cover the most common dimensions of any pleated filter.

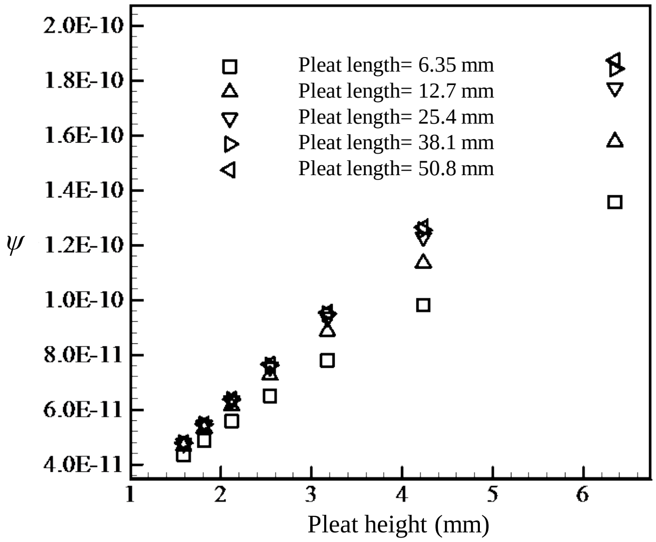

Fig. 7.3: The coefficient ψ for a flat triangular pleated filter as a function of pleat geometry.

The total pressure drop of a pleated filter at any mass loading can be obtained by adding the three components of the pressure drop (Δp_0, Δp_p, and Δp_s). An example of the regimes of filtration (depth and surface) is shown in Fig. 7.4.

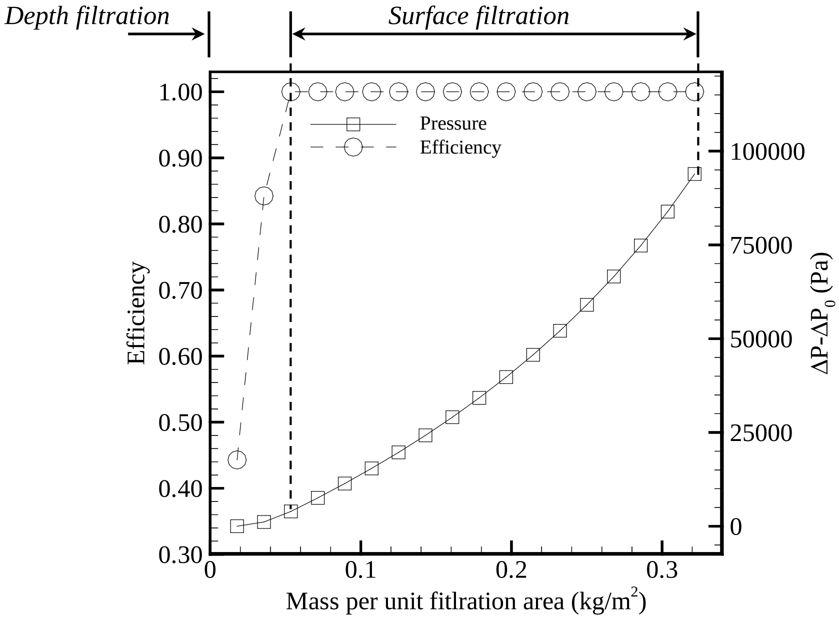

Fig. 7.4: Illustration of the dust loading deposition regimes, the transition from depth to surface filtration shown for dust loading performance of a triangular flat pleated filter.

7.4. Triangular Radial Pleats with Surface Filtration

A triangular filter can be in either a flat pleated arrangement or in a radial pleated arrangement (cartridge filters). To obtain the radial pleated filters correlation, we first conducted a series of parameter studies to report the ratio of dust cake thickness δ_i / δ_f as illustrated in Fig. 7.5. Note that the dust cake is assumed to be a linear profile in the case of radial pleats.

The fraction δ_i / δ_f was only a function of the inlet to outlet diameter ratio (R_{io}) as shown in Fig. 7.6. In this figure, we conducted a wide parameter study changing the number of pleats and consequently pleat angles, and fabric length. As shown in the figure, the fraction of cake thicknesses only depends on R_{io}.

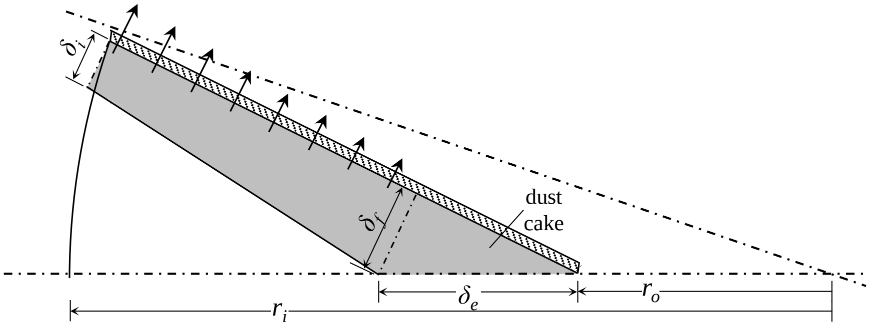

Fig. 7.5: Illustration of the dust-loaded radial pleated filter with linear cake profile.

We conducted a series of parameter studies to calculate the coefficient ψ in the case of non-uniform cake profiles with different pleat heights, widths and cake thickness ratios (f=δ_i / δ_f) as shown in Fig. 7.7a.

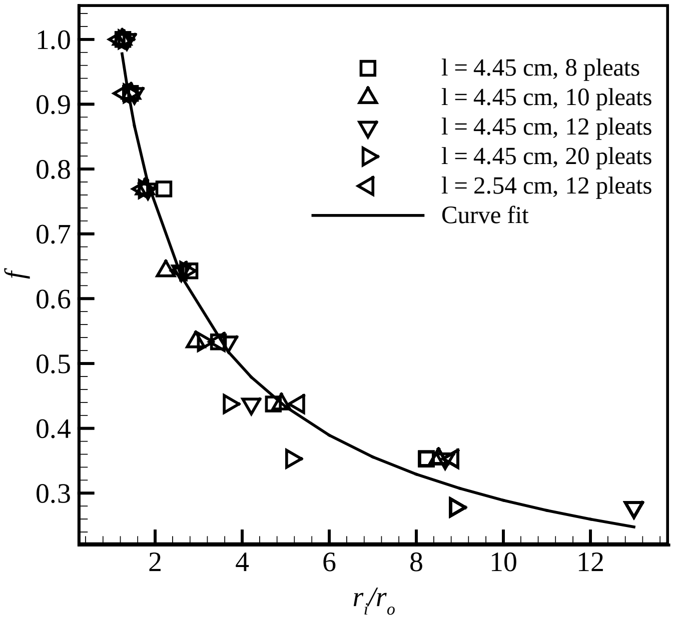

Fig. 7.6: initial to final thickness ratio δ_i / δ_f as a function of inlet-to-outlet diameter ratio R_{io}.

Figure 7.7b shows the normalized coefficient ψ with respect to its maximum corresponding value for each pleat geometry (in the case of uniform cake as in the corresponding flat pleat). Hence, we can relate the performance of a radial pleated filter to its flat counterpart as

$$\frac{\psi}{\psi_{flat}} = 0.9551 f^3 - 2.811 f^2 + 2.86 f \tag{7.25}$$

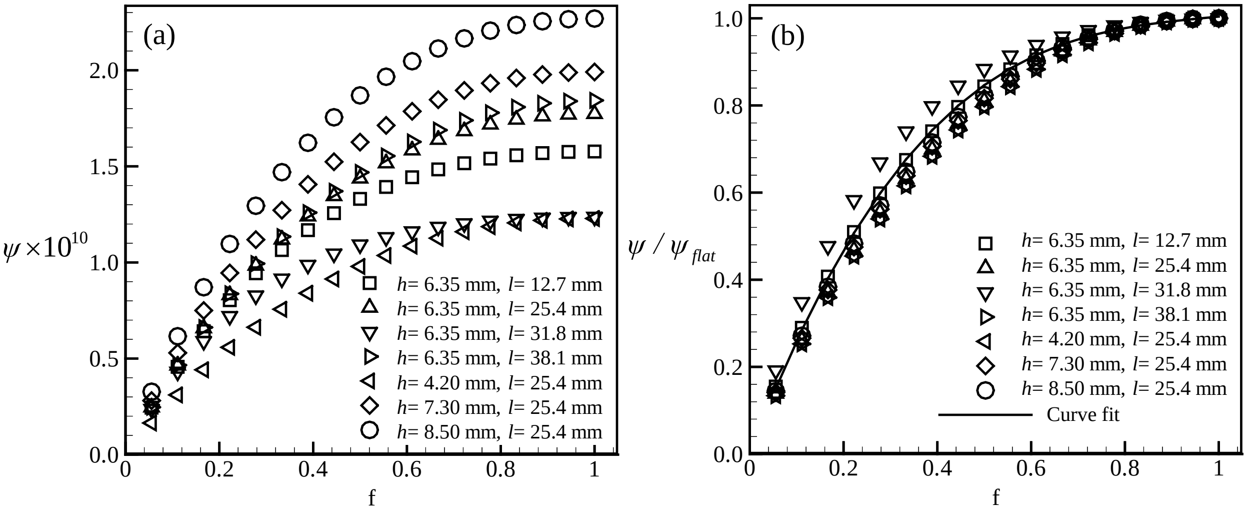

Fig. 7.7: the coefficient of proportionality ψ (a) and its normalized values (b) as a function of initial to final thickness ratio (f= δ_i / δ_f).

7.5. Depth Filtration in Rectangular Pleats

Similar to the discussion given in Section 2 for triangular pleats with depth deposition, the filtration performance of rectangular pleated filters during depth filtration is discussed here. The filtration velocity can be obtained as a function of the inlet velocity by applying mass conservation on the control volume which includes the pleat channel (see Fig. 7. 8a),

$$(2h + l) v_w = 2hU \tag{7.26}$$

where l is the pleat length. Using Darcy's law (Eqn. 7.5), we can obtain the expression for the pressure drop as a function of mass loaded inside the pleat fibrous media as

$$\Delta p_p = \frac{2Uh\mu}{2h+l}\left(\frac{t_m}{k_c}\right) = \frac{2Uh\mu}{2h+l}\frac{180}{d_p^2 c^c}\left(\frac{m_p}{\rho_p V_m}\right)^2\left(1-\frac{m_p}{\rho_p V_m}\right)^{-3} \tag{7.27}$$

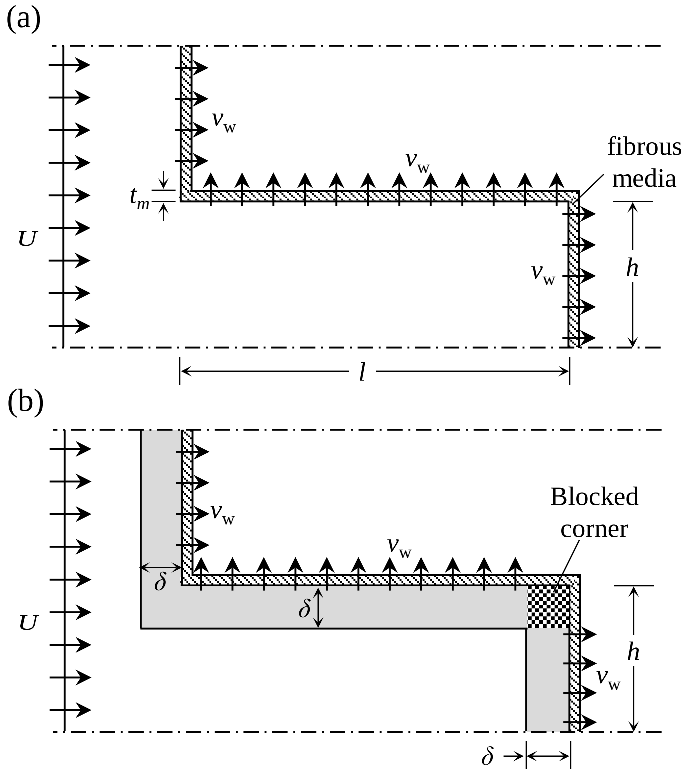

Fig. 7.8: Illustration of dust loaded triangular flat pleated filter with depth (a) and surface (b) deposition.

Regarding the collection efficiency prediction, the same expressions used in Equations 7.11-7.15 can be used here to predict the dust-loaded rectangular pleated filter efficiency. The only differences will be in calculating the filtration velocity v_w and volume of the fibrous media V_m.

7.6. Rectangular Pleats with Surface Filtration

Similar to the discussion presented in Section 3 regarding surface filtration of triangular flat pleated filters, the pressure drop due to surface dust deposition in a pleated filter is inversely proportional to the dust cake permeability, the surface area available for filtration ($l+2h-2\delta$), and the cake solidity α. It is also linearly proportional to the inlet velocity U as shown in Fig. 7.8b. Hence we have:

$$\Delta p_s \sim U, \frac{1}{k_c}, \frac{1}{\alpha_p}, \frac{1}{l+2h-2\delta} \tag{7.28}$$

where δ is the dust cake thickness (we assume uniform thickness layer along the pleat wall). Therefore we can obtain an expression for the pressure drop increase due to surface deposition as

$$\Delta p_s = \psi \frac{m_p}{A_f} U \frac{1}{\alpha_p k_c \left(l+2h-2\delta\right)} \tag{7.29}$$

where ψ is a constant of proportionality. The cake thickness along the pleat can be related to the mass deposited as

$$\delta = \frac{m_p}{A_f \rho_p \alpha_p} \tag{7.30}$$

where A_f here is equal to ($l+2h$). Substituting in the pressure drop equation we can obtain

$$\Delta p_s = \psi \frac{m_p}{A_f} \frac{U}{\alpha_p k_c} \left(l+2h - \frac{m_p}{\rho_p \alpha_p} \frac{2}{l+2h} \right)^{-1} \tag{7.31}$$

It is shown in the above equation that the pressure drop is not a linear function of mass per unit area. In order to linearize the relation we divided the increase in pressure drop by $\frac{U}{\alpha_p k_c} \left(l+2h - \frac{m_p}{\rho_p \alpha_p} \frac{2}{l+2h} \right)^{-1}$. Hence, we obtain a linear function of the linearized pressure drop and the mass loaded per unit area m_p / A_f as can be seen in Fig. 7. 9. The case presented in this figure is for a rectangular pleated surface filter with a pleat height and length of 0.725 and 2.54

cm. The dashed line shows an exact linear function and the solid line shows the linearized pressured drop as a function of mass per unit area.

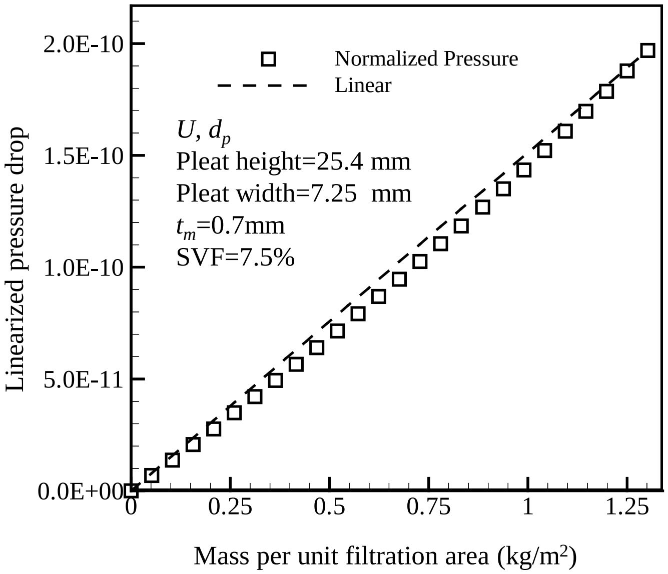

Fig. 7.9: Example of linearized pressure drop as a function of mass per unit area a surface flat rectangular pleated filter. This plot is applicable to any particle diameter and inlet velocity.

The constant of proportionality ψ was found to be only dependent on the pleat height and length. More specifically, it was not a function of the flow velocity or the particle diameter. Values of ψ are plotted in Fig. 7.10. Each point in this figure represents a complete simulation case using our 2-D semi-numerical model when loading each pleat geometry with the mass that fills its channel. We chose the most common pleat heights and lengths so that we can cover the performance of any rectangular pleated filter with any dimension.

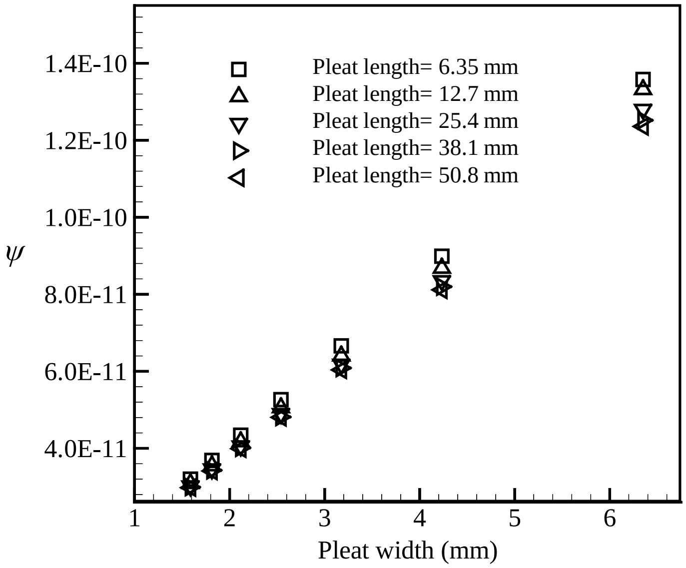

Fig.7.10: The coefficient ψ for a flat rectangular pleated filter as a function of pleat geometry.

7.7. Results and Discussion

In this section we compare our results with our previous macroscale model and with CFD simulations. We start with triangular flat filters in Section 7.1 and then rectangular filters in Section 7.2. In section 7.3 and 7.4, we compare the predictions of our correlations with the macroscale model, which was benchmarked and validated before, for flat triangular and rectangular pleats as well as cylindrical triangular dust-loaded pleats.

7.7.1. Comparison with CFD Simulation: Triangular Pleats

In this section, we considered a complicated filtration regime in which the particles can deposit both inside and outside the fibrous media in a pleated filter. We compare the results of our 2-D macroscale model and the 3-D CFD simulations with those of the present correlations as in Equation 7.7 and 7.13 (see Saleh *et al.*, SPT 2014 for more information about these models). The fibrous medium considered here has an SVF of 7.5% with a fiber diameter of 15 µm. The corresponding fibrous media has a through-plane permeability constant of k=1.6×10-10 m^2.

Figure 11a shows the pressure drop predictions between our present correlation predictions of the pressure drop and both our 3-D CFD and 2-D macroscale model. The triangular pleated filter considered here was challenged with mono-dispersed particles of 1 µm diameter. The dust cake profiles are shown for both the CFD and the macroscale model in Fig. 7.11b.

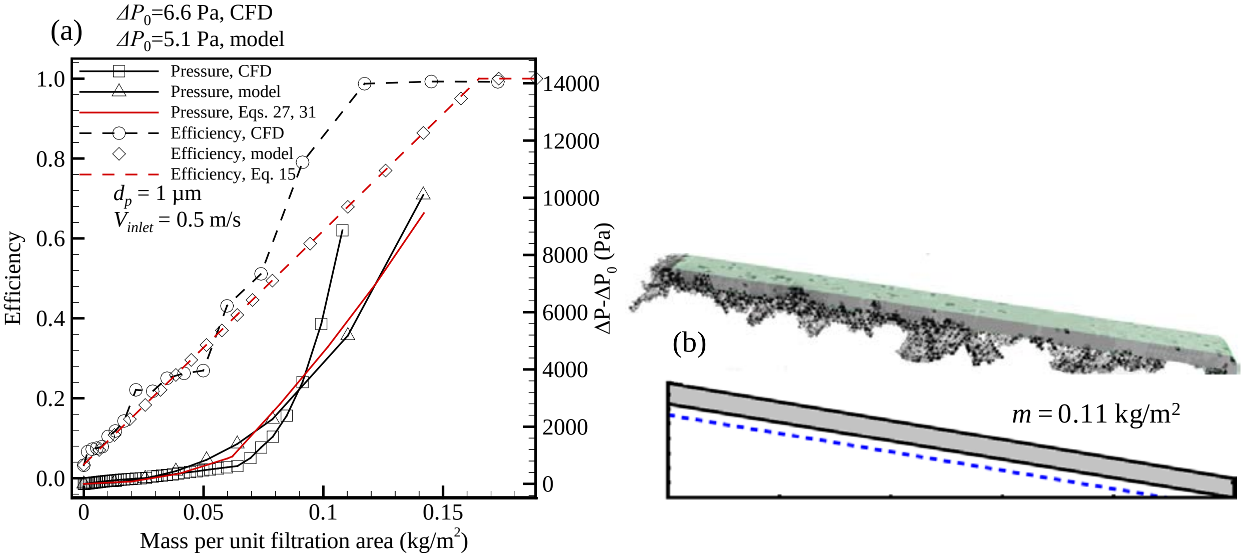

Fig.7.11: Comparison between pressure drop and collection efficiency predictions of the present correlations with both the macroscale model and our CFD calculations for a filter with 4 triangular pleats per inch in surface and depth filtration regimes (a). A particle diameter of 1 µm is considered at an air velocity of 0.5 m/s. Dust deposition patterns are compared in (b) at a mass loading of 0.11 kg/m^2.

7.7.2. Comparison with CFD Simulation: Rectangular Pleats

In this section we present the predictions of our present correlations with both the 2-D macroscale model and the 3-D CFD simulations for a rectangular filter with a pleat count of 4 per inch loaded with 1 µm particles at an inlet velocity of 0.1 m/s and with the same fibrous media characteristics mentioned in Section 7.1. Given the complexity of the problem, the general agreement shown in Fig. 7.12a is acceptable (see the complicated cake morphology and its semi-analytical model counterpart in Figs. 7.12b).

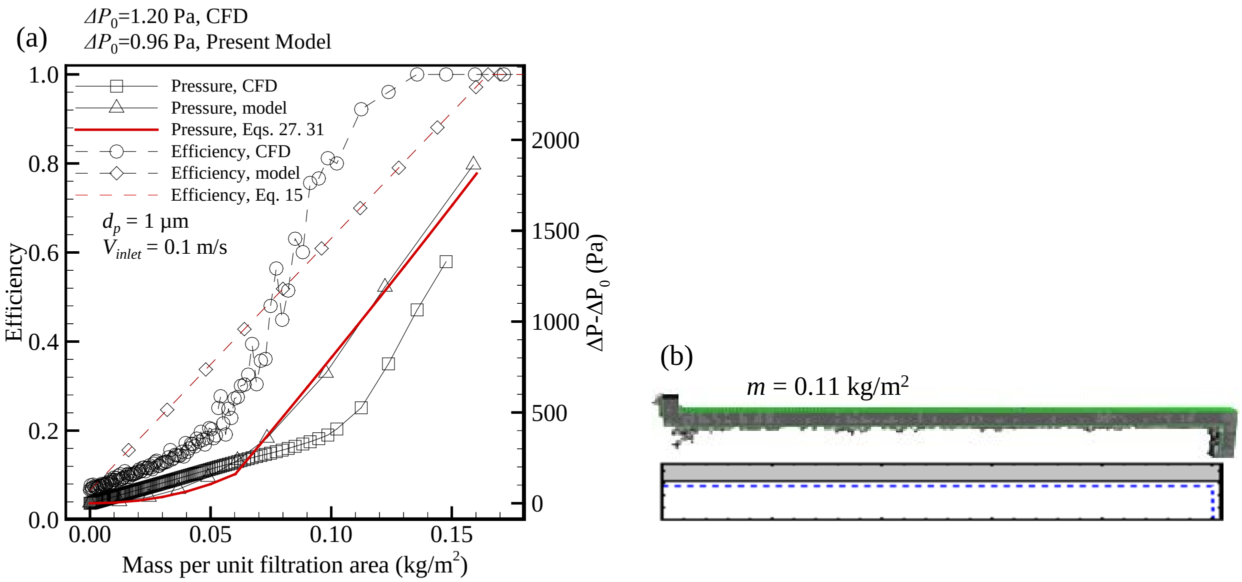

Fig.7.12: Comparison between pressure drop and collection efficiency predictions of the present correlations and both the macroscale model and our CFD calculations for a filter with 4 rectangular pleats per inch in surface and depth filtration regimes (a). A particle diameter of 1 µm is considered at an air velocity of 0.1 m/s [3]. Dust deposition patterns are compared in (b) at a mass loading of 0.11 kg/m^2.

7.7.3. Comparison with 2-D macroscale model: Flat Pleats

In this section, we present the predictions of our present correlations with the 2-D semi-numerical macroscale model for triangular and rectangular pleated filters of 2 and 4 pleat counts per inch loaded with 5 µm particles at an inlet velocity of 1 m/s. The fibrous media were composed of fibers of 15 µm diameter and an SVF of 7.5%. Figure 7.13a shows the pressure drop increase due to loading the triangular pleated filters with 5 µm particles as a function of mass loading per unit area. Whereas Figure 7.13b shows the pressured drop increase when loading the rectangular pleated filters with the same mono-dispersed particles. It can be clearly seen that the pressure drop predictions of the present correlations are in good agreement with those from the 2-D semi-numerical model.

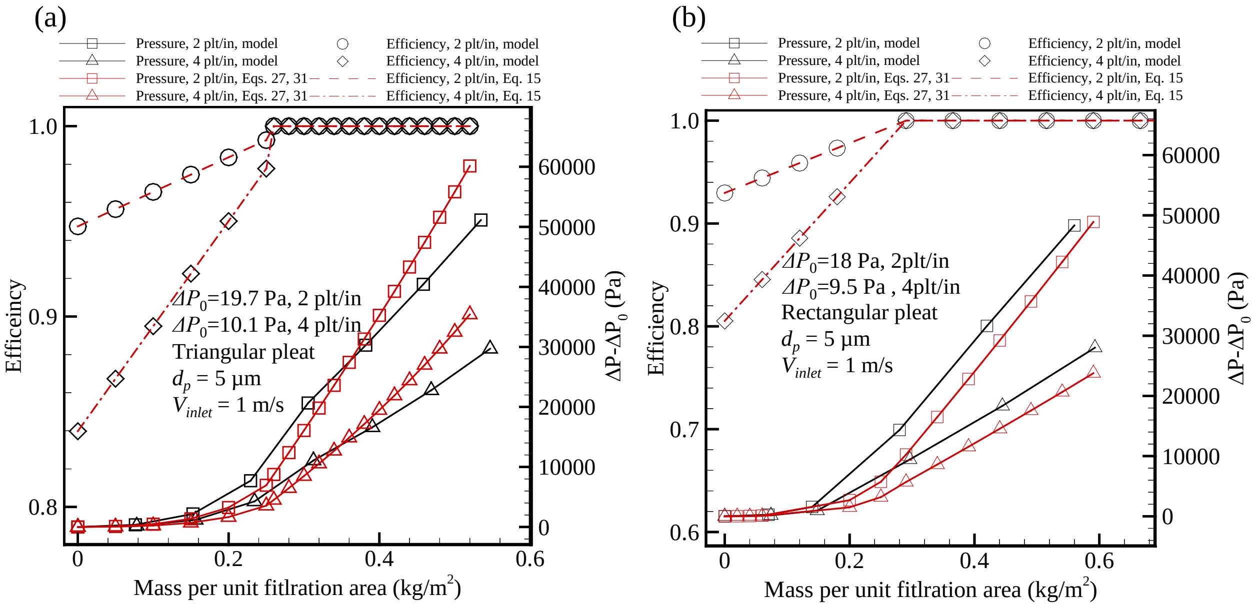

Fig. 7.13: Comparison between pressure drop and collection efficiency predictions of the present correlations and the 2-D semi-numerical macroscale model for a filter with 2 and 4 triangular (a) and rectangular (b) pleats per inch in surface and depth filtration regimes. Inlet air velocity and particle diameter are 1 m/s and 5 µm, respectively.

7.7.4. Comparison with 2-D macroscale model: Cylindrical Pleats

In this section we compare the predictions of our correlations in the case of cylindrical pleated filters with those obtained from our semi-numerical model (Chapter 6). The filters considered here have a half pleat angle of 14.25° and a pleat height and length of 6.4 and 25.4 mm, respectively. We considered two inlet diameters for the cylindrical pleated filters of 57.1 and 65.1 mm and challenged the two pleated filters with 1 and 10 µm particles. Figure 7.14a and 7.14b shows the pressure drop as a function of mass loading per unit area for both our present correlations and the macroscale model predictions when the filters are challenged with 1 and 10 µm particles, respectively. Both predictions seem to agree well with one another.

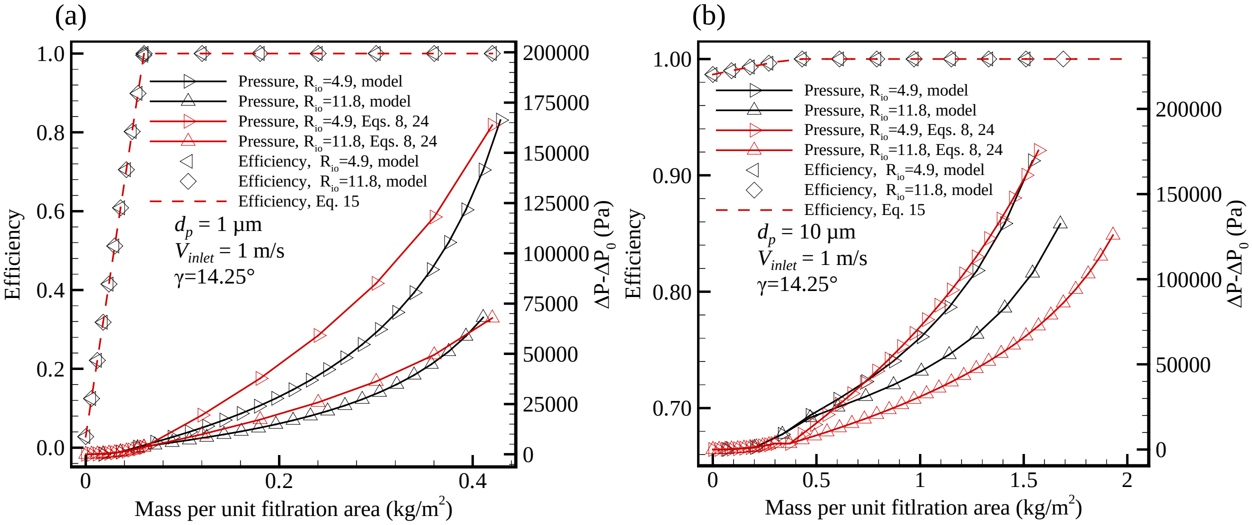

Fig. 7.14: Comparison between pressure drop and collection efficiency predictions of the present correlations and the 2-D semi-numerical macroscale model for a cylindrical filter with half pleat angle γ of 14.25° for different pleat inlet diameters of 57.07 and 65.1 mm when challenged with 1 and 10 µm particles in (a) and (b) respectively. Pleat height and length was 6.4 and 25.4 mm, respectively.

7.8. Chapter Conclusions

This chapter presents the correlations that describe the surface and depth filtration performance in flat and cylindrical triangular pleated filters in addition to flat rectangular pleated ones under dust-loading conditions. These correlations were developed based on simple analytical study in order to minimize the considered parameters that affect the filtration performance of a pleated filter. The predictions of the filtration performance (collection efficiency and pressure drop) of the correlations presented in this work were compared with our previous 2-D semi-numerical model predictions. In order to obtain the pressure drop of dust loaded pleated filters, series of simulations were conducted using our semi-numerical model that was published before for different pleat shapes and geometries. These correlations are believed to be very helpful in the design and development of pleated filters.

Chapter 9

Overall Conclusions

The main goal of this thesis is to advance the modeling of the filtration performance of fibrous filters under dust loading conditions in order to better design a filter. Achieving this goal helps develop correlations describing the filtration performance of a pleated filter from the first day of its service until it is regenerated or disposed using these modeling techniques.

In Chapter 2, we illustrated the microscale model which is used to simulate loading flat-sheet fibrous filters with particles. The air flow field through 3-D fibrous structures was obtained by solving Stokes' equations. Particles were tracked in a Lagrangian approach using ANSYS–Fluent code enhanced with user-defined functions in order to be able to model the instantaneous efficiency and pressure drop of a dust-loaded filter. We also implemented a 1-D macroscale model from the literature. The comparison between the models revealed thatA close comparison between the results of the 1-D macroscale and 3-D microscale simulations indicates that the former requires a series of ad-hoc or case-dependent correction factors before it can produce accurate predictions for the instantaneous pressure drop or collection efficiency of a fibrous filter under dust-loading. In contrast, the 3-D microscale simulation method proposed in this study is self-sufficient, as it is developed based on first principles, and can potentially replace the traditional design methods currently used in industry for product development.

In Chapter 3, we presented a CPU-affordable 3-D macroscale model to simulate the service life of pleated fibrous filters when challenged with mono- and poly-dispersed aerosols. The model enables one to predict the pressure drop and collection efficiency in both surface and depth filtration regimes. It is important to mention that this model is much faster than the microscale model which makes it feasible to conduct limited parameter studies to help product design. The model was compared with microscale model in the case of flat-sheet filter and good agreement between the results was evident.

In Chapter 4, we utilized both the above 3-D micro and macroscale models in order to investigate the performance of trilobal fibers when compared with their circular counterparts under dust loading. Correlations for both pressure drop and collection efficiency were presented for the fibers with different cross-sectional shape. Trilobal fibers are found to outperform their circular counterparts only when the particles are highly inertial, and only if the orientation of the trilobal cross-section with respect to the incoming flow is such that one of the grooves of the fiber faces the flow with a normal angle. In cases of low inertial particles, trilobal fibers were found to experience higher efficiency values with loading but at the expense of higher increase in pressure drop. The same performance prevails when the fibers have through-plane orientation. Therefore, trilobal fibers are not expected to have any advantage over circular ones given the lack of the available control on their orientation.

A fast easy-to-use 2-D semi-numerical model was presented in Chapter 5 and Chapter 6 for simulating the filtration performance of dust loaded flat and circular pleated filters, respectively. The model uses the knowledge of the CFD micro and macroscale models illustrated in Chapter 2 and 3 in order to obtain the velocity field inside the pleat channel. The dust-cake pattern is obtained by tracking the particle trajectories inside the pleat channel. The particles' equations of motion are solved with the analytical expression of the velocity fields—a set of second order ordinary differential equations. Instantaneous pressure drop and collection efficiency estimates for pleated filters in presence of dust-loading in both depth and surface filtration regimes were obtained by the approximate dust cake profiles, air flow mass conservation and Darcy's law. Good agreement was observed when the results of this model were compared with CFD models. It was found that filters with rectangular pleats can potentially provide better performance than their triangular counterparts under heavy loading, due to their larger surface area available for the filtration. From the comparison in Chapter 6 between flat and circular (cartridge) triangular pleated filters, circular pleated filters were found to outperform their flat counterparts, especially when they experience smaller inlet diameters (high inlet to outlet diameter ratios).

In Chapter 7, we presented the correlations that describe the performance of any pleated filter (rectangular, triangular flat and radial pleated filters). These correlations are very helpful for the industry to obtain good approximate predictions of the pressure drop of any pleated filter under dust loading conditions.

References

References

Bemer, D., Regnier, R., Morele, Y., Grippari, F., Appert-collin, J.C. and Thomas, D. (2013). "Study of clogging and cleaning cycles of a pleated cartridge filter used in a thermal spraying process to filter ultrafine particles." Powder Technology 234: 1-6.

Bergman, W., Taylof, R.D., Miller, H.H., Biermann, A.H., Hebard, H.D., Da Roza, R.A. and Lum, B.Y. (1978). Enhanced filtration program at LLNL. 15th DOE Nuclear Air Cleaning Conf., Boston.

Bourrous, S., Bouilloux, L., Ouf, F.X., Appert-Collin, J.C., Thomas, D., Tampère, L. and Morele, Y. (2014). "Measurement of the Nanoparticles Distribution in Flat and Pleated Filters During Clogging." Aerosol Science and Technology 48(4): 392-400.

Box, G.E.P. and Muller, M.E. (1958). "A NOTE ON THE GENERATION OF RANDOM NORMAL DEVIATES." Annals of Mathematical Statistics 29(2): 610-611.

Brown, R.C. (1993). Air Filtration. Pergamon Press Inc.

Carman, P.C. (1956). Flow of Gases through Porous Media. Butterworths, London.

Chen, D.-R., Pui, D.Y.H. and Liu, B.Y.H. (1995). "Optimization of Pleated Filter Designs Using a Finite-Element Numerical Model." Aerosol Science and Technology 23(4): 579-590.

Cheng, Y.-H. and Tsai, C.-J. (1998). "Factors Influencing Pressure Drop through a Dust Cake during Filtration." Aerosol Science and Technology 29(4): 315-328.

Cheung, C.S., Cao, Y.H. and Yan, Z.D. (2005). "Numerical Model for particle deposition and loading in electret filter with rectangular split-type fibers." Computational Mechanics 35(6): 449-458.

Clague, D.S. and Phillips, R.J. (1997). "A numerical calculation of the hydraulic permeability of three-dimensional disordered fibrous media." Physics of Fluids 9(6): 1562-1572.

Davies, C.N. (1973). Air Filtration. Academic Press, London.

Doganoglu, Y., Jog, V., Thambimuthu, K. V., Clift, R. (1978). Removal of fine particles from gases in fluidized beds. Trans. Inst. Chem. Eng., 56: 296.

Dullien, F.A.L. (1992). Porous media fluid transport and pore structure, 2nd Edition, Academic Press, Inc. San Diego, California, USA.

Dunnett, S.J. and Clement, C.F. (2009). "A numerical model of fibrous filters containing deposit." Engineering Analysis with Boundary Elements 33(5): 601-610.

Dunnett, S.J. and Clement, C.F. (2012). "Numerical investigation into the loading behaviour of filters operating in the diffusional and interception deposition regimes." Journal of Aerosol Science 53(0): 85-99.

Filippova, O. and Hänel, D. (1997). "Lattice-Boltzmann simulation of gas-particle flow in filters." Computers & Fluids 26(7): 697-712.

Fotovati, S., Hosseini, S.A., Vahedi Tafreshi, H. and Pourdeyhimi, B. (2011). "Modeling instantaneous pressure drop of pleated thin filter media during dust loading." Chemical Engineering Science 66(18): 4036-4046.

Fotovati, S., Tafreshi, H.V. and Pourdeyhimi, B. (2011). "Analytical expressions for predicting performance of aerosol filtration media made up of trilobal fibers." Journal of Hazardous Materials 186(2–3): 1503-1512.

Fotovati, S., Vahedi Tafreshi, H. and Pourdeyhimi, B. (2010). "Influence of fiber orientation distribution on performance of aerosol filtration media." Chemical Engineering Science 65(18): 5285-5293.

Geisler, M., Wachtel, J., Hemberger, F., Schultz, T., Vidi, S. and Ebert, H.P. (2008). "Trilobal polyimide fiber insulation for cryogenic applications." International Journal of Thermophysics 29(4): 1385-1394.

Gervais, P.C., Bardin-Monnier, N. and Thomas, D. (2012). "Permeability modeling of fibrous media with bimodal fiber size distribution." Chemical Engineering Science 73(0): 239-248.

Gervais, P.C., Poussier, S., Bardin-Monnier, N., Karcher, G. and Thomas, D. (2014). "Combination of Single-Photon Emission and X-Ray Computed Tomography to visualize aerosol deposition in pleated filter." Separation and Purification Technology 126(0): 52-61.

Gupta, A., Novick, V.J., Biswas, P. and Monson, P.R. (1993). "Effect of Humidity and Particle Hygroscopicity on the Mass Loading Capacity of High Efficiency Particulate Air (HEPA) Filters." Aerosol Science and Technology 19(1): 94-107.

Happel, J. (1959). "Viscous flow relative to arrays of cylinders." AIChE Journal 5(2): 174-177.

Hasolli, N., Park, Y.O. and Rhee, Y.W. (2013). "Filtration performance evaluation of depth filter media cartridges as function of layer structure and pleat count." Powder Technology 237: 24-31.

Hinds, W.C. (1982). Aerosol Technology, properties, behavior, and measurement of airborne particles. John Wiley & Sons, Inc. New York.

Hinds, W.C. and Kadrichu, N.P. (1997). "The effect of dust loading on penetration and resistance of glass fiber filters." Aerosol Science and Technology 27(2): 162-173.

Hinds, W.C. (1999). Aerosol Technology, properties, behavior, and measurement of airborne particles. John Wiley & Sons, Inc. New York.

Hosseini, S.A. and Tafreshi, H.V. (2010). "3-D simulation of particle filtration in electrospun nanofibrous filters." Powder Technology 201(2): 153-160.

Hosseini, S.A. and Tafreshi, H.V. (2010). "Modeling particle filtration in disordered 2-D domains: A comparison with cell models." Separation and Purification Technology 74(2): 160-169.

Hosseini, S.A. and Tafreshi, H.V. (2010). "Modeling permeability of 3-D nanofiber media in slip flow regime." Chemical Engineering Science 65(6): 2249-2254.

Hosseini, S.A. and Tafreshi, H.V. (2011). "On the importance of fibers' cross-sectional shape for air filters operating in the slip flow regime." Powder Technology 212(3): 425-431.

Hosseini, S.A. and Vahedi Tafreshi, H. (2012). "Modeling particle-loaded single fiber efficiency and fiber drag using ANSYS–Fluent CFD code." Computers & Fluids 66(0): 157-166.

Jaganathan, S., Vahedi Tafreshi, H. and Pourdeyhimi, B. (2008). "On the pressure drop prediction of filter media composed of fibers with bimodal diameter distributions." Powder Technology 181(1): 89-95.

Joubert, A., Laborde, J.C., Bouilloux, L., Calle-Chazelet, S. and Thomas, D. (2010). "Influence of Humidity on Clogging of Flat and Pleated HEPA Filters." Aerosol Science and Technology 44(12): 1065-1076.

Joubert, A., Laborde, J.C., Bouilloux, L., Chazelet, S., Thomas, D. (2011). "Modelling the pressure drop across HEPA filters during cake filtration in the presence of humidity." 66 (2) 616-623.

Jung, I., Kim, S.Y. and Oh, T.H. (2010). "Effects of Spinning Conditions on Shape Changes of Trilobal-shaped Fibers." Textile Research Journal 80(1): 12-18.

Kanaoka, C., Emi, H. and Myojo, T. (1980). "Simulation of the growing process of a particle dendrite and evaluation of a single fiber collection efficiency with dust load." Journal of Aerosol Science 11(4): 377-389.

Kanaoka, C., Hiragi, S. and Tanthapanichakoon, W. (2001). "Stochastic simulation of the agglomerative deposition process of aerosol particles on an electret fiber." Powder Technology 118(1–2): 97-106.

Karaca, E. and Ozcelik, F. (2007). "Influence of the cross-sectional shape on the structure and properties of polyester fibers." Journal of Applied Polymer Science 103(4): 2615-2621.

Kasper, G., Schollmeier, S. and Meyer, J. (2010). "Structure and density of deposits formed on filter fibers by inertial particle deposition and bounce." Journal of Aerosol Science 41(12): 1167-1182.

Kasper, G., Schollmeier, S., Meyer, J. and Hoferer, J. (2009). "The collection efficiency of a particle-loaded single filter fiber." Journal of Aerosol Science 40(12): 993-1009.

Kuwabara, S. (1959). "The forces experienced by randomly distributed parallel circular cylinders or spheres in a viscous flow at small Reynolds numbers." Journal of the Physical Society of Japan 14(4): 527-532.

Lamb, G.E.R., Costanza, P. and Miller, B. (1975). "Influences of Fiber Geometry on the Performance of Nonwoven Air Filters." Textile Research Journal 45(6): 452-463.

Lamb, G.E.R. and Costanza, P.A. (1980). "Influences of Fiber Geometry on the Performance of Nonwoven Air Filters: Part III : Cross-Sectional Shape." Textile Research Journal 50(6): 362-370.

Lamb, G.E.R., Costanza, P.A. and Turner, J.H. (1980). "Role of Filter Structure and Electrostatics in Dust-Cake Formation." Textile Research Journal 50(11): 661-667.

Landahl, H.D. and Herrmann, R.G. (1949). "Sampling of liquid aerosols by wires, cylinders, and slides, and the efficiency of impaction of the droplets." Journal of Colloid Science 4(2): 103-136.

Lantermann, U. and Hänel, D. (2007). "Particle Monte Carlo and lattice-Boltzmann methods for simulations of gas–particle flows." Computers & Fluids 36(2): 407-422.

Lee, K.W. and Liu, B.Y.H. (1982). "Theoretical Study of Aerosol Filtration by Fibrous Filters." Aerosol Science and Technology 1(2): 147-161.

Li, A. and Ahmadi, G. (1992). "Dispersion and Deposition of Spherical Particles from Point Sources in a Turbulent Channel Flow." Aerosol Science and Technology 16(4): 209-226.

Li, S.Q. and Marshall, J.S. (2007). "Discrete element simulation of micro-particle deposition on a cylindrical fiber in an array." Journal of Aerosol Science 38(10): 1031-1046.

Lo, L.-M., Hu, S.-C., Chen, D.-R. and Pui, D.Y.H. (2010). "Numerical study of pleated fabric cartridges during pulse-jet cleaning." Powder Technology 198(1): 75-81.

Longest, P.W. and Xi, J. (2007). "Effectiveness of Direct Lagrangian Tracking Models for Simulating Nanoparticle Deposition in the Upper Airways." Aerosol Science and Technology 41(4): 380-397.

Lücke, T. and Fissan, H. (1996). "The prediction of filtration performance of high efficiency gas filter elements." Chemical Engineering Science 51(8): 1199-1208.

Mattern, K.J. and Deen, W.M. (2008). ""Mixing Rules" for estimating the hydraulic permeability of fiber mixtures." Aiche Journal 54(1): 32-41.

Maze, B., Vahedi Tafreshi, H., Wang, Q. and Pourdeyhimi, B. (2007). "A simulation of unsteady-state filtration via nanofiber media at reduced operating pressures." Journal of Aerosol Science 38(5): 550-571.

Montgomery, J.F., Green, S.I., Rogak, S.N. (2015). "Impact of Relative Humidity on HVAC Filters Loaded with Hygroscopic and Non-Hygroscopic Particles." 49 (5) 322-331.

Omeroglu, S., Karaca, E. and Becerir, B. (2010). "Comparison of Bending, Drapability and Crease Recovery Behaviors of Woven Fabrics Produced from Polyester Fibers Having Different Cross-sectional Shapes." Textile Research Journal 80(12): 1180-1190.

Park, B.H., Lee, M.H., Jo, Y.M. and Kim, S.B. (2012). "Influence of pleat geometry on filter cleaning in PTFE/glass composite filter." Journal of the Air & Waste Management Association 62(11): 1257-1263.

Payatakes, A.C. and Gradon, L. (1980). "DENDRITIC DEPOSITION OF AEROSOLS BY CONVECTIVE BROWNIAN DIFFUSION FOR SMALL, INTERMEDIATE AND HIGH PARTICLE KNUDSEN NUMBERS." Aiche Journal 26(3): 443-454.

Payatakes, A.C. and Tien, C. (1976). "Particle deposition in fibrous media with dendrite-like pattern: A preliminary model." Journal of Aerosol Science 7(2): 85-100.

Przekop, R., Moskal, A. and Gradoń, L. (2003). "Lattice-Boltzmann approach for description of the structure of deposited particulate matter in fibrous filters." Journal of Aerosol Science 34(2): 133-147.

Raynor, P.C. (2008). "Single-Fiber Interception Efficiency for Elliptical Fibers." Aerosol Science and Technology 42(5): 357-368.

Rebai, M., Prat, M., Meireles, M., Schmitz, P. and Baclet, R. (2010). "Clogging modeling in pleated filters for gas filtration." Chemical Engineering Research and Design 88(4): 476-486.

Regan, B.D. and Raynor, P.C. (2009). "Single-Fiber Diffusion Efficiency for Elliptical Fibers." Aerosol Science and Technology 43(6): 533-543.

Rudnick, S. N., and First, M. W. (1978). Specific resistance (K2) of filter dust cakes: comparison of theory and experiments. Third Symposium on Fabric Filters for Particulate Collection, EPA-600/7-78-007, 251-288.

Saleh, A.M., Fotovati, S., Vahedi Tafreshi, H. and Pourdeyhimi, B. (2014). "Modeling service life of pleated filters exposed to poly-dispersed aerosols." Powder Technology 266(0): 79-89.

Saleh, A.M., Hosseini, S.A., Vahedi Tafreshi, H. and Pourdeyhimi, B. (2013). "3-D microscale simulation of dust-loading in thin flat-sheet filters: A comparison with 1-D macroscale simulations." Chemical Engineering Science 99(0): 284-291.

Saleh, A.M. and Vahedi Tafreshi, H. (2014). "A simple semi-numerical model for designing pleated air filters under dust loading." Separation and Purification Technology 137(0): 94-108.

Saleh, A.M. and Vahedi Tafreshi, H. (2015). "On the filtration performance of dust-loaded trilobal fibers." Separation and Purification Technology 149(0): 295-307.

Saleh, A.M., Tafreshi, H.V., Pourdehimi, B. (Submitted for publication)."Service Life of Circular Pleated Filters vs. their Flat Counterpart." Separation and Purification Technology

Sanchez, J.R., Rodriguez, J.M., Alvaro, A. and Estevez, A.M. (2010). "Deduction and Application of Filtration and Cleaning Indices for Aerosol Filtration Operations Using Nonwoven Fabrics as Filters." Environmental Progress & Sustainable Energy 29(1): 17-24.

Sánchez, J.R., Rodríguez, J.M., Alvaro, A. and Estévez, A.M. (2007). "The capture of fly ash particles using circular and noncircular cross-section fabric filters." Environmental Progress 26(1): 50-58.

Sirkar, K.K. (1975). "Transport in Packed Beds at Intermediate Reynolds Numbers." Industrial & Engineering Chemistry Fundamentals 14(1): 73-74.

Spielman, L. and Goren, S.L. (1968). "Model for predicting pressure drop and filtration efficiency in fibrous media." Environmental Science & Technology 2(4): 279-287.

Spurny, K.R. (1998). Advances in aerosol filtration, Lewis Publisher, CRC Press LLC: 471.

Stechkina, I.B. and Fuchs, N.A. (1966). "Studies on Fibrous Aerosol Filters—I. Calculation of Diffusional Deposition of Aerosols in Fibrous Filters." Annals of Occupational Hygiene 9(2): 59-64.

Stechkina, I. B. (1969). Diffusion precipitation of aerosols in fiber filters, Dokl. Acad. Nauk. SSSR: 167, 1327.

Subrenat, A., Bellettre, J. and Le Cloirec, P. (2003). "3-D numerical simulations of flows in a cylindrical pleated filter packed with activated carbon cloth." Chemical Engineering Science 58(22): 4965-4973.

Tafreshi, H.V., Rahman, M.S.A., Jaganathan, S., Wang, Q. and Pourdeyhimi, B. (2009). "Analytical expressions for predicting permeability of bimodal fibrous porous media." Chemical Engineering Science 64(6): 1154-1159.

Tascan, M. and Vaughn, E.A. (2008). "Effects of Total Surface Area and Fabric Density on the Acoustical Behavior of Needlepunched Nonwoven Fabrics." Textile Research Journal 78(4): 289-296.

Thomas, D., Contal, P., Renaudin, V., Penicot, P., Leclerc, D. and Vendel, J. (1999). "Modelling pressure drop in hepa filters during dynamic filtration." Journal of Aerosol Science 30(2): 235-246.

Thomas, D., Penicot, P., Contal, P., Leclerc, D. and Vendel, J. (2001). "Clogging of fibrous filters by solid aerosol particles Experimental and modelling study." Chemical Engineering Science 56(11): 3549-3561.

Tien, C. (1989). Granular filtration of aerosols and hydrosols, Butterworths, Boston.

Tien, C., 2012. Priciples of Filtration. Elsevier.

Waghode, A.N., Hanspal, N.S., Wakeman, R.J. and Nassehi, V. (2007). "Numerical Analysis of Medium Compression and Losses in Filtration area in Pleated Membrane Cartridge Filters." Chemical Engineering Communications 194(8): 1053-1064.

Wakeman, R.J., Hanspal, N.S., Waghode, A.N. and Nassehi, V. (2005). "Analysis of Pleat Crowding and Medium Compression in Pleated Cartridge Filters." Chemical Engineering Research and Design 83(10): 1246-1255.

Wang, H., Zhao, H., Guo, Z. and Zheng, C. (2012). "Numerical simulation of particle capture process of fibrous filters using Lattice Boltzmann two-phase flow model." Powder Technology 227(0): 111-122.

Wang, Q., Maze, B., Tafreshi, H.V. and Pourdeyhimi, B. (2006). "A case study of simulating submicron aerosol filtration via lightweight spun-bonded filter media." Chemical Engineering Science 61(15): 4871-4883.

Wang, Q., Maze, B., Tafreshi, H.V. and Pourdeyhimi, B. (2007). "Simulating through-plane permeability of fibrous materials with different fiber lengths." Modelling and Simulation in Materials Science and Engineering 15(8): 855-868.

Appendix A

Collection efficiency due to interception and inertial impaction are the dominant capture mechanism for the particles considered here. For the interception SFE, we used the expression proposed by Lee and Liu (1982),

$$\eta_{R0} = 0.6 \frac{1-\alpha}{Ku} \frac{R^2}{(1+R)} \tag{A1}$$

In this equation $Ku = -\frac{ln\,\alpha}{2} - 0.75 + \alpha - 0.25\alpha^2$ is the Kuwabara factor. The SFE due to impaction is obtained using the following expression given by Brown (1993) for moderate values of Stokes number,

$$\eta_{I0} = \frac{Stk^3}{Stk^3 + 0.77Stk^2 + 0.22} \tag{A2}$$

where $Stk = \frac{\rho_P\, d_P^2\, c^c\, V}{18\,\mu\, d_f}$ is the Stokes number.

Filter efficiency, *E*, can be obtained based on the total SFE, $\eta_{\Sigma 0}$, as follows using (Brown 1993),

$$\eta_{\Sigma 0} = 1-(1-\eta_{R0})(1-\eta_{I0}) \tag{A3}$$

$$E = 1 - exp\left(\frac{-4\,\alpha\,\eta_{\Sigma 0}\, Z}{\pi d_f\,(1-\alpha)}\right) \tag{A4}$$

The empirical pressure drop correlation of Davies (1973) for clean fibrous media ΔP_0 is given as,

$$\frac{\Delta p_0}{Z} = 64\mu V \frac{\alpha^{1.5}(1+65\alpha^3)}{d_f^2} \qquad \text{(A5)}$$

Appendix B

The three major mechanisms for particle capture are Brownian diffusion, direct interception, and inertial impaction. To predict the capture mechanisms due to diffusion in granular beds, we used the following expression for the single collector efficiency (Tien, 2012):

$$E_D = 4\,As^{1/3}Pe^{2/3} \tag{B1}$$

In the above equation, $Pe = V\,d_f\,/\,D$ is the Peclet number, $D = \sigma\,c^c\,T\,/\,(3\pi\,\mu\,d_P)$ is particle diffusivity, $\sigma = 1.38\times10^{-23}\,(m^2kg\,s^{-2}\,K^{-1})$ is the Boltzmann constant, and *As* is the correction factor. Note that $As = 2\left(1-q^5\right)/\left(2-3q+3q^5-2q^6\right)$, and $q = \mathrm{SVF}^{1/3}$. To obtain the capture efficiency due to interception with Reynolds number less than 1, the following equation was used:

$$E_R = 1.5\,g^3R^2 \tag{B2}$$

The correction factor g for the range of granular collectors (previously deposited particles) in this study is the following (Sirkar, 1975):

$$g = \left\{\left[2+1.5\left(1-\varepsilon\right)+1.5\left[8\left(1-\varepsilon\right)-3\left(1-\varepsilon\right)^2\right]^{0.5}\right]\Big/\varepsilon\left[2-3\left(1-\varepsilon\right)\right]\right\}^{1/3} \tag{B3}$$

Equation A3 is valid when the granular collector has $Re < 1$, with cell porosity ε of greater than 0.33 and Peclet number greater than 1000. Finally, for the single collector efficiency due to inertial impaction, the equation offered by Doganoglu (1978) was modified for the range of our collector and particles sizes:

$$E_I = 2.89\gamma Stk \qquad \text{(B4)}$$

where $Stk = \dfrac{\rho_P\, d_P^2\, c^c\, V}{18\,\mu\, d_c}$ is the Stokes number, and d_c is the collector diameter. Note that $\gamma = 0.00318\,Stk^{-1.248}$ is the correction factor. It has been added to the equation B4, to make it valid for the range of particles Stokes number ($Stk > 0.01$) in this study (Tien, 1989).

Particle penetration through a filter can be estimated based on the above single collector expressions:

$$P = exp\left(\frac{-4\,\alpha\, E_\Sigma\, thk_c}{\pi d_f\,(1-\alpha_c)}\right) \qquad \text{(B5)}$$

In this equation E_Σ is the total single collector efficiency, and is defined as $E_\Sigma = 1-(1-E_D)(1-E_R)(1-E_I)$. Particle penetration through each computational cell P is calculated using the above equation. The cell dimension here is used as the filter thickness.

Appendix C

For particle capture in fibrous media, the work of Stechkina (1969) was used to estimate the Single Fiber Efficiency (SFE) due to Brownian diffusion, as shown below.

$$E_D = 2.9Ku^{-1/3}\,Pe^{-2/3} + 0.62Pe^{-1} \qquad \text{(C1)}$$

In this equation $Ku = -\frac{ln\,\alpha}{2} - 0.75 + \alpha - 0.25\alpha^2$ is the Kuwabara factor, Pe is the Peclet number.

To predict SFE due to interception, the expression proposed by Lee and Liu (1982) was used:

$$E_R = 0.6\frac{1-\alpha}{Ku}\frac{R^2}{(1+R)} \qquad \text{(C2)}$$

The SFE due to impaction was predicted using the following expression (Pich, 1966):

$$E_I = \frac{Stk^3}{Stk^3 + 0.77Stk^2 + 0.22} \qquad \text{(C3)}$$

Note that fiber diameter d_f is constant, but the SVF of the cell (α) will be updated every time some mass is deposited in the cell.

Using the above equations, the value for total SFE (E_Σ) can be obtained and the total particle penetration through the filter can be calculated using equation (B5).

Vita

Ahmed Mohammed Saleh

2526 Waldo Ln., Richmond, VA 23228 ▪ Saleham@vcu.edu
Born in Jeddah, Saudi Arabia, May, 31st 1983, and an Egyptian Citizen

EDUCATION

Ph.D., Mechanical Engineering, (Expected August 2015**)**
Virginia Commonwealth University (VCU), Richmond, VA
Dissertation: Micro- and Macro-Scale Modeling of Filter Aging: Effects of Particle Poly-Dispersity and Fiber Cross-Sectional Shape
GPA 3.86

M.S., Mechanical Engineering , 2011
Mechanical Engineering Department, Faculty of Engineering, Alexandria University, Egypt
Dissertation: Optimization of Multiple Heaters in a vented enclosure
GPA 3.95

B.S., Mechanical Engineering, 2005
Mechanical Engineering Department, Faculty of Engineering, Alexandria University, Egypt
Grade: Distinction with Honors (1 of only 2 "Distinction" grade holders among 450 graduates)
Graduation Project: Design of Specific Features in a Liquefied Natural Gas (LNG) Plant, including supplementary designs
GPA 3.8

RESEARCH EXPERIENCE

Research Assistant, Mechanical and Nuclear Engineering Department, VCU, Richmond, 2011-Present

- Developed User-Defined Functions (UDF) using C programming language for ANSYS-Fluent to model the flow in dust loaded fibrous media:
  - Conducted particle tracking using the Discrete Phase Model (DPM) enhanced with particle size consideration and Brownian Diffusion motion for nanoparticles in addition to enabling particles deposition on the fibers or previously deposited particles
  - Modeled poly-disperse particle deposition in a novel macroscale model, solving analytical expressions for aerosol filtration, simulating pleated filters aging during depth and surface filtration
  - Considered the dust deposition by marking the cells containing deposits and adding sink terms to them when solving the momentum equations to accurately model their resistance to the flow

- Developed fast easy-to-use 2-D semi-analytical model to predict the filtration performance of pleated filters (radial/cylindrical and flat triangular and rectangular flat pleated filters). Solving the particles' equation of motion (a set of 2nd order ODEs) to obtain particle trajectories inside the pleat channel leads to an approximate dust deposition profile. The model was validated with experimental data from the literature and compared with the more sophisticated 3-D CFD macroscale model. Effects of pleat geometry and shape were investigated. The simple method gives good approximate prediction of the pleated filter performance in a matter of seconds instead of few days in the case of the 3-D macroscale model

- Studied the effect of fiber cross-sectional shape on the filtration performance under dust loading conditions. Using trilobal fibers as a filter medium was found not to have a great privilege on the filtration performance compared with circular fibers. Correlations for the performance of flat-sheet filters with circular and non-circular cross sections shapers were developed by applying the micro and macroscale CFD models

- Developed correlations for predicting the filtration performance of pleated filters during their life cycle

- Presented semi-annual reports and presentations to the Industrial Board Meetings at the Nonwovens Institute, NC State University for the last three years

AWARDS AND HONORS

- Ranked top 2nd student in the class of Mechanical Engineering department, Faculty of Engineering, Alexandria University (among 450 undergrads)
- Best graduation project in mechanical engineering, Faculty of Engineering, Alexandria University, Egypt
- Best mechanical engineering project (among all universities' graduation project in Egypt) in the Egyptian Engineering Day (EED) conference held in Cairo and sponsored by the Institute of Electrical and Electronics Engineers (IEEE)
- Elected to represent the Department of Mechanical Engineering in the Ideal Student Competition for two consecutive years during undergraduate studies, Alexandria University, Egypt
- Dean of Engineering Award for excellence in Engineering Education, Alexandria University, Egypt. Academic years 2000–01, 2002–03, 2003–04, and 2004–05.
- Ph.D. research funded by VCU and the Nonwovens Institute at NC State University

JOURNAL PUBLICATIONS

Saleh, A.M., Hosseini, S.A., Tafreshi, H.V., Pourdeyhimi, B., 2013. 3-D Microscale Simulation of Dust-Loading in Thin Flat-Sheet Filters: A Comparison with 1-D Macroscale Simulations. *Chemical Engineering Science,* 99, 284-291.

Saleh, A.M., Fotovati, S., Tafreshi, H.V., Pourdeyhimi, B., 2014. Modeling Depth and Surface Deposition of Poly-Dispersed Dust in Pleated Filters. *Powder Technology,* 266, 79-89.

Saleh, A.M., Tafreshi, H.V. Semi-Numerical Model for Predicting the Service Life of Pleated Filters, 2014. *Separation and Purification Technology,* 137, 94-108.

Saleh, A.M., Tafreshi, H.V. On The Filtration Performance of Dust-Loaded Trilobal Fibers, 2015. *Separation and Purification Technology,* 149, 295–307

Saleh, A.M., Tafreshi, H.V., Pourdeyhimi, B., Service Life of Circular Pleated Filters vs. their Flat Counterpart, (submitted for publication), *Separation and Purification Technology.*

Saleh, A.M., Tafreshi, H.V., Pourdeyhimi, B., Predictive Correlations for the Performance of Dust-Loaded Pleated Filters, (to be submitted).

OTHER RELEVANT EXPERIENCE

Mechanical Engineer Officer, First Lieutenant, Egyptian Naval Forces (2nd Brigade of Missile Crafts) 2007 – 2008

- Supervised overhauls of diesel engines, air compressors and pumps in the Brigade Workshop, spare parts management, and served as on-call second ship engineer

Second Ship Engineer, First Lieutenant, Egyptian Naval Forces 2006 – 2007

- On board a missile craft, supported operations, repairs and scheduled maintenance

Undergraduate Research Assistant, Freiberg University of Technology, Germany 2004

- Projects: Heat Transfer Simulation of welding preheating in train rails, and measuring emissivities of various metals using Infrared Imaging

TEACHING EXPERIENCE

Teaching Assistant 2011 – 2013
Mechanical and Nuclear Engineering Department, VCU, Richmond, VA

Demonstrator and Researcher 2008 – 2011
Faculty of Engineering, Mechanical Engineering Department, Alexandria University, Egypt

Instructor 2006 – 2011
Arabic Academy for Science and Technology in the Faculty of Maritime Transport, Egypt

Courses Taught:
Mathematics, Mechanics, Physics, Numerical Methods, Advanced Engineering Mathematics, Thermodynamics, Thermal Power Plants, HVAC and Heat Transfer

SKILLS

Professional Command of the following

- Computer Programming (C, FORTRAN, Mathematica, MATLAB, Visual Basic)
- FlexPDE
- ANSYS–FLUENT
- AutoCAD
- Geographical Information System **(**GIS)
- Windows and Linux operating systems
- Microsoft Office package

PROFESSIONAL ACTIVITY

Assisted in reviewing for the following journals

- Aerosol Science and Technology
- Chemical Engineering Research and Design
- Chemical Engineering and Technology

- Chemical Engineering Science
- Industrial and Engineering Chemistry Research
- International Journal of Heat and Mass Transfer
- Journal of Aerosol Science
- Journal of Nanoparticle Research
- Powder Technology
- Separation and Purification Technology
- Separation Science and Technology
- The Korean Journal of Chemical Engineering

RELEVANT GRADUATE COURSEWORK

- Advanced Engineering Mathematics
- Advanced Fluid Mechanics
- Applied Statistics for Engineers and Scientists
- Computational Fluid Dynamics
- Convective Heat Transfer
- Independent study of porous media
- Introduction to Aerosol Science and Technology
- Numerical solutions of Differential Equations